Copyright

By

Thomas Earl Dyson

2010

The Thesis committee for Thomas Earl Dyson Certifies that this is the

Approved version of the following thesis:

Effects of Hole Pitch Variation on Overall and Internal Effectiveness in the Leading Edge Region of a Simulated Turbine Blade with Heat Flux Measurements

APPROVED BY

SUPERVISING COMMITTEE:

Supervisor:

David G. Bogard

Robert Moser

Effects of Hole Pitch Variation on Overall and Internal Effectiveness in the Leading Edge Region of a Simulated Turbine Blade with Heat Flux Measurements

By

Thomas Earl Dyson, B.S.M.E.

Thesis

Presented to the Graduate School

of the University of Texas at Austin

in Partial Fulfillment

of the Requirements

for the Degree of

Master of Science in Engineering

The University of Texas at Austin

May 2010

Dedication

To my parents

Acknowledgments

Foremost, I would like to thank Dr. David Bogard for giving me the opportunity to work for him and take advantage of his vast experience. His guidance and advice was instrumental in the production of this work. Secondly, I would like to thank Pratt & Whitney and our contract supervisors, Atul Kohli and Justin Piggush for their part in this endeavor. Additionally, I'd like to thank Dr. Robert Moser for supplying useful input.

I would also like to thank Don Artieschoufsky, Curtis Johnson, Mike Slotboom, and the rest of the Mechanical Engineering shop team for their advice and support in producing the models used in this study. Without their input and dedicated effort this project would have been dead in the water. I would also like to thank Mark Phillips for helping me out with the heat flux gauges.

Last, but certainty not least, I would like to thank the other students in the TTCRL group, Jason Albert, Jason Dees, Todd Davidson, Emily Pfautsch, Laurene Dobrowolski and Aimie Faucett. At one point or another, all provided invaluable help and or data used in the completion of this project.

Effects of Hole Pitch Variation on Overall and Internal Effectiveness in the Leading Edge Region of a Simulated Turbine Blade with Heat Flux Measurements

By

Thomas Earl Dyson, M.S.E.

The University of Texas at Austin, 2010

SUPERVISOR: David Bogard

In this study, the cooling of a simulated blade under increasing pitch between holes was examined. The change in non-dimensional surface temperature, ϕ, was measured experimentally to quantify this performance loss. This critical quantification of the sensitivity of cooling to pitch between holes has not been studied previously. A range of blowing ratios and angles of attack were tested. Data are presented in terms of the laterally averaged ϕ, and in terms of the minimum ϕ, arguably more important from a design perspective. Increasing the pitch 13% produced no measureable change using either parameter. An increase of 26% in pitch produced only a 4% loss in lateral averages, while some hot points dropped by 10%. These small changes are due to compensating effects of increased internal and through-hole convective cooling. A limit to these

effects was shown when increasing pitch 53%. While performance loss in the average was still relatively small at 15%, the minimum ϕ decreased by 27%.

Heat flux gauges were used to gather data on the internal and external surface. The internal impingement used in this study represents a more accurate representation of internal cooling for an actual engine part than has been previously studied, providing a starting point for exploring the differences between engine configurations and those generally investigated in the literature. External heat flux measurements were used to measure the ratio of heat flux with and without film cooling. These results call into question the use of the net heat flux reduction parameter, which is commonly used to quantify overall film cooling performance.

Table of Contents

Acknowledgments v
Table of Contents viii
List of Figures x
List of Tables xiv
Nomenclature xv
1 Introduction 1
1.1 The Basics 2
1.2 Film Cooling 5
1.2.1 Film Cooling Parameters 6
1.2.2 Hot Spots and the Matched Biot Number Model 13
1.3 Objectives of Current Study 18
2 Experimental Facility and Procedure 20
2.1 Wind Tunnel Facility 20
2.2 Test Model Assembly and Instrumentation 23
2.2.1 Geometric Parameters 23
2.2.2 Polycast Leading Edge Model 25
2.2.3 Corian® Leading Edge Model 29
2.2.4 Adiabatic Leading Edge Model 30
2.2.5 Model Instrumentation 31
2.2.6 Coolant Supply Plenum and Impingement Plates 33
2.2.7 Infrared Cameras 36
2.3 Heat Flux Calibration Apparatus and Procedure 39
2.3.1 Constant Heat Flux Plate 40
2.3.2 Gauge Attachment Procedure 44
2.3.3 Model Installation Procedure 47
2.4 Test Procedure and Data Reduction 50
2.5 Uncertainty Analysis 57
3 Results and Discussion 70
3.1 Adiabatic Effectiveness Results 72
3.1.1 Effects of Blowing Ratio Variation 72
3.1.2 Effects of Angle of Attack Variation 79
3.2 Effects of Pitch Variation 84
3.2.1 Effects of M Variation 86
3.2.2 Effects of α Variation on ϕ with Varying Pitch 95
3.2.3 Simplified Analysis 104

3.3 Effects of Pitch Variation Using $\boldsymbol{\phi min}$ Analysis 109
3.3.1 Effects of α Variation under Varying Pitch Using ϕmin Analysis 112
3.4 Effects of Pitch Variation Using Constant Mass Flow Analysis 116
3.5 Internal Cooling 119
3.5.1 Internal Temperature Profiles 120
3.5.2 Internal Heat Flux 126
3.6 External Heat Flux Data 131
4 Conclusions 141
4.1 Adiabatic Effectiveness for *p/d* = 7.6 142
4.2 Effects of Pitch Variation on Film Cooling Performance 143
4.3 Internal and External Heat Flux Measurements 146
4.4 Recommendations for Future Work 148
A. Appendix 150
A.1 Explanation for Constant Internal and External Heat Transfer Coefficients 150
A.2 Verification that the Aluminum Impingement Plate was Not Adversely Affecting Effectiveness Measurements 151
References 154
Vita 157

List of Figures

Figure 1.1.1: Ideal Brayton cycle as applied to a gas turbine engine [2] 2
Figure 1.2.1: Basic diagram of how film cooling works [6] 5
Figure 1.2.2: Visual explanation of the principle behind the use of T_{aw} in film cooling 8
Figure 1.2.3: Comparison of contours of η and ϕ for a leading edge model with p/d = 7.6, M = 1.0, α = 0° and DR = 1.5 15
Figure 1.2.4: Simplified representation of the flow of energy around a cooling hole [6] 16
Figure 2.1.1: Abstract diagram of TTCRL's small wind tunnel facility 21
Figure 2.2.1: Diagram of some dimensions and coordinates used to define a leading edge model 24
Figure 2.2.2: Diagram of the leading edge model 25
Figure 2.2.3: Diagram of the new aluminum mold without the internal radius piece 27
Figure 2.2.4: The end stage of withdrawing the inner radius insert from a new part 28
Figure 2.2.5: Comparison of two model materials at p/d = 8.6, M = 2 and DR = 1.5 30
Figure 2.2.6: Internal thermocouple positions on a flattened representation of the inner surface of the leading edge model 32
Figure 2.2.7: Coolant supply plenum. All dimensions are in millimeters. 33
Figure 2.2.8: A schematic of the p/d = 7.6 impingement plate geometry used for this study. Dimensions are in inches. 34
Figure 2.2.9: The plastic impingement plate offers at least one clear advantage 36
Figure 2.2.10: Representation of the IR camera setup used to observe the leading edge model 37
Figure 2.2.11: Database of points used to generate the new standard calibration curve for the P25 camera 38
Figure 2.3.1: Circuit diagram of the constant heat flux apparatus 41
Figure 2.3.2: Constant heat flux plate 42
Figure 2.3.3: Constant heat flux plate with some instrumentation installed 42
Figure 2.3.4: Raw IR image of the plate after 45 minutes at approximately 1300 W/m^2 44
Figure 2.3.5: Raw IR image of the installed gauges with their wires taped down 46
Figure 2.4.1: In-test repeatability for test ID 090406; p/d = 7.6, M = 2 and DR = 1.5 52
Figure 2.4.2: Test-to-test repeatability and the average value for p/d = 7.6, M = 2 and DR = 1.5. 52

Figure 2.4.3: IR calibrations used for the experiments done for this study 54
Figure 2.5.1: Comparison of two contour plots of η for M = 0.48 and DR within 0.01. In the first case (a) there is a small amount of coolant flowing from the leading edge holes, in the second (b) no coolant is visible. 61
Figure 2.5.2: Comparison of ϕi measurements taken after reinstalling thermocouples in the same location 63
Figure 2.5.3: Heat flux calculated using the manufacturer's specification compared to a known heat flux using the thermal grease method and another method 66
Figure 3.1.1: Comparison of η under changing M for p/d = 7.6 and α = 0° 73
Figure 3.1.2: Contours of η for p/d = 7.6, and (a) M = 0.5, (b) 1.0 and (c) 1.5 76
Figure 3.1.3: Contours of η for p/d = 7.6 and (a) M = 2.0, (b) 2.5 and (c) 2.9 76
Figure 3.1.4: Comparison to the Tu = 0.5% data of Johnston (DR = 1.8) and Yuki (DR = 1.1) at M = 1 78
Figure 3.1.5: Comparison to the Tu = 0.5% data of Johnston (DR = 1.8) and Yuki (DR = 1.1) at M = 2 78
Figure 3.1.6: Comparison of η under changing α for p/d = 7.6 and M = 2.0 81
Figure 3.1.7: Contours of η for α = 0° for p/d = 7.6 and M = 2 82
Figure 3.1.8: Contours of η for α = ±0.6° (a) and ±1.5° (b) for p/d = 7.6 and M = 2 82
Figure 3.1.9: Contours of η for α = (a) 4.6° and (b) 7.7° for p/d = 7.6 and M = 2 84
Figure 3.2.1: ϕ comparison for various blowing ratios with p/d = 7.6 86
Figure 3.2.2: ϕ comparison between the data taken for the current study and that of Maikell *et al.* using p/d = 7.6 88
Figure 3.2.3: ϕ vs. x/d for M = 1.5 89
Figure 3.2.4: Average ϕ values from multiple data points for M = 2.0 90
Figure 3.2.5: Contours of ϕ for M = 2 and p/d = (a) 7.6, (b) 8.6, (c) 9.6 and (d) 11.6 92
Figure 3.2.6: Comparison of ϕ and η for p/d = 7.6 and $\phi 0$ 93
Figure 3.2.7: ϕ vs. x/d for M = 3.0 94
Figure 3.2.8: ϕ vs. x/d for M = 0.5 95
Figure 3.2.9: ϕ comparison at all tested α values for p/d = 7.6 with M = 2 [22] .. 97
Figure 3.2.10: ϕ comparison at all tested α values for p/d = 9.6 with M = 2 97
Figure 3.2.11: ϕ comparison at all tested α values for p/d = 11.6 with M = 2 98
Figure 3.2.12: Lateral comparison of ϕ for p/d = 11.6, M = 2 at x/d = 0 99
Figure 3.2.13: Pitch variation at M = 2.0 and α = ±4.6° 100
Figure 3.2.14: Contours of ϕ for p/d = 7.6 at α = 4.6° and M = 2 [22] 101
Figure 3.2.15: Contours of ϕ for p/d = 8.6 at α = ±4.6° and M = 2 102
Figure 3.2.16: Contours of ϕ for p/d = 9.6 at α = ±4.6° and M = 2 102
Figure 3.2.17: Contours of ϕ for p/d = 11.6 at α = ±4.6° and M = 2 103
Figure 3.2.18: Lateral ϕ at x/d = 2 for M = 2 and α = 0° 108

Figure 3.2.19: Lateral ϕ at *x/d* = 6 for *M* = 2 and α = 0° 109
Figure 3.3.1: ϕmin plot for *M* = 2 and α = 0° with all four values of *p/d* 111
Figure 3.3.2: Comparison of ϕ and ϕmin for *p/d* = 7.6, 9.6 and 11.6 at *M* = 2. Note the enlarged scale. 111
Figure 3.3.3: Comparison of ϕ and ϕmin for all pitches with *M* = 2 and α = 0° at *x/d* = 2 112
Figure 3.3.4: ϕmin plot for *M* = 2.0 and α = ±0.6° 113
Figure 3.3.5: ϕmin plot for *M* = 2.0 and α = ±4.6° 114
Figure 3.3.6: Comparison between ϕmin and ϕ for some α values at *p/d* = 7.6 and *M* = 2. Note the expanded scale. 115
Figure 3.4.1: ϕ comparison plot for all values of *p/d* using constant overall mass flow 117
Figure 3.4.2: ϕ comparison plot for all values of *p/d* using constant mass per hole 117
Figure 3.4.3: Comparison of ϕ vs. *p/d* for all tested blowing ratios 119
Figure 3.5.1: Comparison of ϕi for *M* = 2 and *p/d* = 7.6, 8.6, and 9.6 with no impingement 121
Figure 3.5.2: Temperature uniformity at the 0° position 121
Figure 3.5.3: Comparison with the computational predictions of Ravelli *et al*. for *p/d* = 7.6 using impingement cooling with a metal plate 124
Figure 3.5.4: Comparison with the computational predictions of Ravelli *et al*. for *p/d* = 7.6 with no internal impingement 124
Figure 3.5.5: Comparison between measured values of ϕi and the computational predictions of Ravelli *et al*. with impingement and without for *M* = 2 126
Figure 3.5.6: Nu_j vs. Re_j comparison for internal impingement with data from the literature and Ravelli *et al*.'s computational predictions for x/d_j = 0 130
Figure 3.5.7: Nu_j vs. Re_j comparison for internal impingement with data from the literature and Ravelli *et al*.'s computational predictions for x/d_j = 2 131
Figure 3.6.1: h/h_0 for all available positions on the external surface with *p/d* = 7.6 132
Figure 3.6.2: Contours of η for *M* = (a) 0.5, (b) 1.0 and (c) 1.5 with scale heat flux gauges shown 133
Figure 3.6.3: Contours of η for *M* = (a) 2.0, (b) 2.5 and (c) 2.9 with scale heat flux gauges shown 134
Figure 3.6.4: Overall and adiabatic NHFR for *x/d* = 4.9 and *z/d* = 8.7 with variation in *M* from 0.5 to 2.0 and approximate uncertainty bands 136
Figure 3.6.5: Comparison of $\phi 0$ from Dobrowolski and ϕ for *M* = 1 and 2 137
Figure 3.6.6: Overall and adiabatic NHFR for *x/d* = 4.9 and *z/d* = 10 with variation in *M* from 0.5 to 2.0 138
Figure 3.6.7: Overall and adiabatic NHFR for *x/d* = 1.8 and *z/d* = 6.2 with variation in *M* from 0.5 to 2.0 138

Figure 3.6.8: The ratio of non-dimensional surface temperature with and without film cooling for the positions of the three heat flux gauges 140
Figure A.2.1: Comparison different impingement conditions using ϕ for M = 2 and p/d = 7.6 152
Figure A.2.2: Comparison of ϕi for M = 2 and p/d = 7.6 for aluminum and acrylic impingement plates..... 153

List of Tables

Table 2.2.1: Geometric definition of some parameters for the leading edge model 24
Table 2.3.1: Measured calibration factors for all gauges 47
Table 2.5.1: Uncertainty values for external heat flux measurements in absolute terms and as a percentage of the measurement for the given condition . 68
Table 3.1.1: M^* for the stagnation and off-stagnation rows of holes for a given M 74
Table 3.1.2: Position of the stagnation point under changing angle of attack 80
Table 3.1.3: Estimated M^* for each α with an overall $M = 2$ 80

Nomenclature

Symbols

Bi – Biot number
d – diameter
D – leading edge diameter
DR – density ratio
h – heat transfer coefficient
I – current
k – thermal conductivity
L – length of cooling hole through the surface
M – overall blowing ratio, also known as mass flux ratio
*M** – local blowing ratio
Nu – Nusselt number
p – pitch
P – pressure
Pr – Prandtl number
q'' – heat flux per unit area
r – leading edge radius
Re – Reynolds number
t – impingement plate thickness
T – temperature
Tu – mainstream turbulence level
U – stream-wise velocity
V – Volts
x – stream-wise dimensional coordinate along the surface
z – cross-stream dimensional coordinate

Greek

γ – specific heat ratio
ζ – impingement jet outlet-to-target spacing
η – predominantly represents adiabatic film cooling effectiveness, but may also represent efficiency
ρ – density
ϕ – overall effectiveness

Subscripts

0 – without film cooling
aw – adiabatic wall
c – coolant when applied to temperature, combined internal when applied to *h*
f – film cooling
h – hole
i – internal
j – impingement jet
o – outer
w – wall
∞ – mainstream

1 Introduction

The basic principle of gas turbine operation – expanding a heated fluid to perform work – has been known since antiquity, but it was not until the late 18th century that a mechanism that might be recognized as a modern gas turbine was built. John Barber's device had a compressor, combustion, and a turbine, but it did not produce useful work. It took until the early portion of the 20th century for technology to advance to the point where a gas turbine engine could compete with other engines for power generation and propulsion. Since the 1940s, gas turbine engines have been an increasingly important source of power for a variety of vehicles, from airplanes and helicopters to large naval vessels. And while steam turbines have been used for power generation for decades longer, gas turbines have become an integral part of our power grid, providing power to countless homes. A gas turbine's ability to produce large amounts of power – in the form of thrust for jets, or shaft work for helicopters – in a relatively small, light package make them highly desirable for use in aviation. For power generation, the gas turbine's advantages include the ability to startup quickly and, when used in a combined cycle, a high thermodynamic efficiency unmatched by other forms of power generation.

1.1 The Basics

Whether producing electrical energy through driving a motor or thrust to propel an aircraft, all forms of gas turbine engines have a few common features. They all operate on the Brayton cycle, a thermodynamic cycle first described by George Brayton in 1872 [1]. An ideal Brayton cycle consists of four stages, isentropic compression, isobaric heat addition, isentropic expansion, and isobaric heat rejection. All gas turbines have common components to operate on this cycle: compressor, combustor, and turbine. Power generation plants expand the working fluid as much as possible and exhaust the result to atmosphere. In jet aircraft applications, much of the energy remains in the fluid after expansion and is converted to thrust via a nozzle.

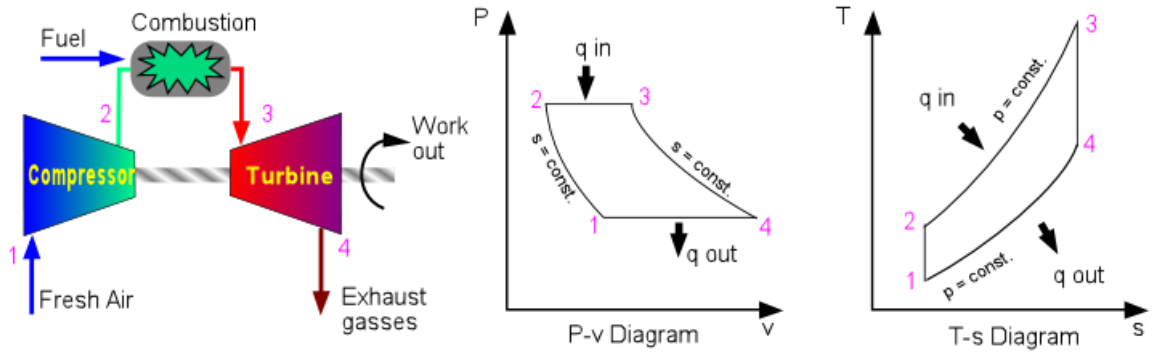

Figure 1.1.1: Ideal Brayton cycle as applied to a gas turbine engine [2]

As with any endeavor to produce work, there is a strong desire to do so efficiently. Gas turbines consume large amounts of fuel, and every erg of work

that can be extracted increases the value of the engine. The cycle efficiency of a gas turbine is described by either of the following equations:

$$\eta = 1 - \frac{T_4 - T_1}{T_3 - T_2} \qquad (1.1.1)^{[3]}$$

$$\eta = 1 - \frac{1}{\left(P_2/P_1\right)^{(\gamma-1)/\gamma}} \qquad (1.1.2)^{[3]}$$

The second equation is easily derived from the first using the properties of the Brayton cycle as described above, and a known specific heat ratio, γ, 1.4 for air. In an ideal system there are only a few ways to increase the efficiency:

- Increase the pressure ratio of the engine
- Reduce exhaust temperature
- Reduce compressor exit temperature
- Increase combustor exit temperature

The increase in combustion temperature is often a very desirable solution, though it poses many challenges. The gas exiting the combustor in modern engines already possesses a temperature in excess of the melting point of most materials. Special alloys and metallurgical techniques have been developed to raise the maximum allowable temperature, but even the most advanced materials are subject to melting and oxidation.

There are three primary methods used to keep the surface temperatures of turbine components down. The first method is to coat the vane or blade in an insulating material – a thermal barrier coating, or TBC – that can better withstand direct exposure to hot mainstream gasses. There are several failure mechanisms that TBC faces, namely: oxidation, fatigue, and erosion. Oxygen is able to penetrate the TBC material and oxidize the coating that bonds the TBC to the metal. Fatigue due to the mismatch in thermal expansion of TBC and the airfoil material also results in a breakdown in the interface [4]. The eventual result is that the TBC material spalls off, exposing the metal. For this reason, TBC is used primarily to extend the service life of an engine [5]. TBC is only useful with some method of heat extraction.

Cooling comes from relatively cold compressor stage air that is bled off and run through cooling channels inside the airfoil. The design of internal passages can incorporate many technologies to improve heat transfer, including internal jet impingement and ribs in the coolant passages to increase values of h_i.

The coolant can be returned through the base, or, as is usually the case, it can be exhausted through small holes in the surface. These holes are the third form of cooling available to reduce the metal temperature, and are known as film cooling holes.

1.2 Film Cooling

Film cooling is the process where cooling gas exits through small holes in the hot part. The resulting jets of coolant produce a protective layer on the surface of the airfoil that insulates the metal from the hot mainstream, as illustrated below. Additionally, the gas provides a great deal of direct cooling as it passes through the metal of the part.

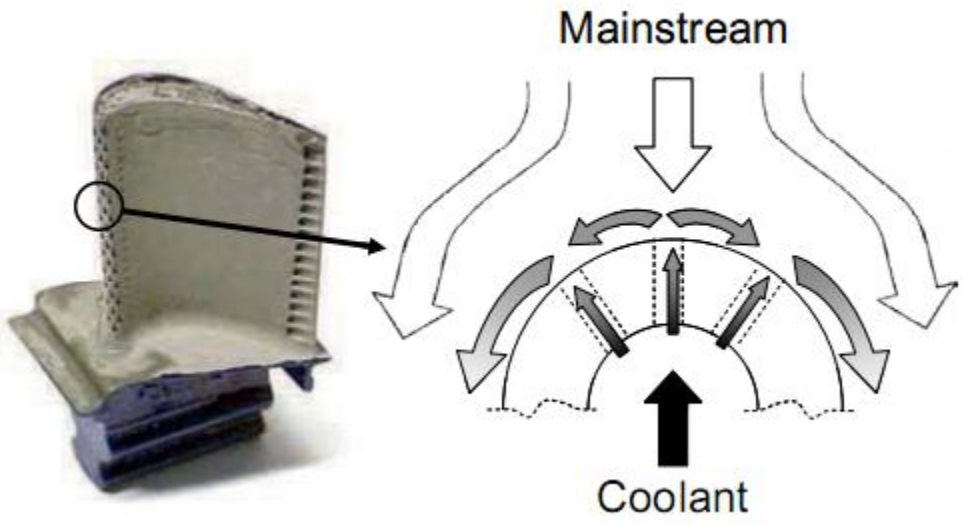

Figure 1.2.1: Basic diagram of how film cooling works [6]

The combined effect of through-hole convective cooling, surface cooling, and insulation from the mainstream is, in general, quite substantial. The result is that the engine's operating temperature can be safely raised without causing a reduction in part life or thermal failure.

However, the cost of this cooling is the previously mentioned air extracted from the compressor. Work is done to compress the coolant but no work is subsequently recovered. If coolant is improperly distributed the net result could be an engine with a lower efficiency. Therefore, a film cooling design should be selected that maximizes the potential performance of a given flow rate of coolant.

Of particular interest is the region on the leading edge of the airfoil. This region is subjected to the highest heat loads, and is heavily cooled using many film cooling holes, known as the showerhead. A large fraction of coolant is exhausted in this region.

1.2.1 Film Cooling Parameters

There are many important parameters that are used to define and understand performance of different film cooling designs. First, there are two commonly used parameters for describing how much coolant is being used. The first is mass flux ratio, or blowing ratio, *M.* It is defined as a ratio of coolant velocity and density to mainstream velocity and density as follows:

$$M = \frac{\rho_c U_c}{\rho_\infty U_\infty} \tag{1.2.1}$$

The coolant velocity and density are evaluated at the exit of the cooling hole. In most studies, the velocity to use for the mainstream is obviously the velocity outside the boundary layer. However, in the case of the leading edge this

velocity can be considered zero along the stagnation line. In this case, the approach velocity is used instead. Another parameter that is sometimes used to characterize coolant use is the momentum flux ratio, defined:

$$I = \frac{\rho_c U_c^2}{\rho_\infty U_\infty^2} \tag{1.2.2}$$

Momentum flux ratio can be used to compare results at dissimilar density ratios. Since this study was performed at a constant density ratio, momentum and mass flux are both valid, and blowing ratio was chosen in order to better compare to existing data. Density ratio is another important parameter for defining the coolant:

$$DR = \frac{\rho_c}{\rho_\infty} \tag{1.2.3}$$

Ethridge *et al.* [7] showed that the effect of density ratio on adiabatic film effectiveness is small above *DR* = 1.1 on the suction side of the airfoil. Ekkad *et al.* [8] used a cylindrical model to examine density ratio effects closer to the leading edge. Their findings showed that changes in *DR* more strongly affected heat transfer coefficient than coolant coverage, and these effects were reduced at higher mainstream turbulence levels. While engine conditions are sometimes as high as *DR* = 2.0, these findings allow the lower *DR* used in this study, 1.5, to be compared with confidence.

The behavior of the coolant along the surface can be observed by using the adiabatic wall temperature, T_{aw}, to track where coolant is distributed. Wherever coolant is present it provides protection from the mainstream by insulating the surface from direct interaction with hot gasses. In theory, this temperature can also be considered the temperature driving the heat flux along the wall, as visualized in Figure 1.2.2. Note that the coolant jet is not at a uniform temperature as might be implied by this figure. Instead, theory states that at some point within the coolant jet the temperature profile will match up with that seen using a purely adiabatic wall.

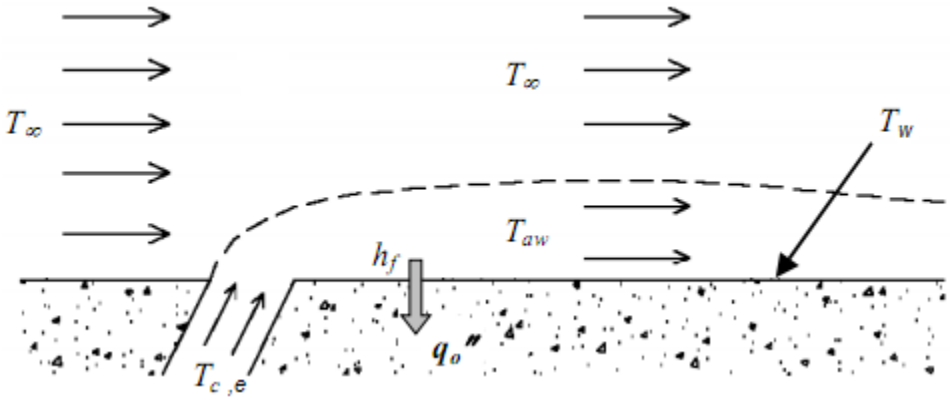

Figure 1.2.2: Visual explanation of the principle behind the use of T_{aw} in film cooling

If a constant heat flux is imposed on an adiabatic surface by say, a thin metal foil, and the surface is cooled by "coolant" which is the same temperature ratio as the mainstream air, then,

$$q'' = h(T_\infty - T_w) = h_f(T_{aw} - T_w) \tag{1.2.4}$$

which initially shows two fundamentally different heat transfer coefficients, becomes the same equation, since $T_{aw} = T_\infty$. The assumption that h_f can be used in this way forms the basis of using constant heat flux on an adiabatic surface to measure heat transfer coefficient changes with film cooling.

A good way to normalize the adiabatic wall temperature is the adiabatic film cooling effectiveness, η. This measure is a non-dimensional temperature that is defined as a ratio between the difference between the mainstream temperature and T_{aw}, and the difference between T_∞ and the coolant temperature, T_c:

$$\eta = \frac{T_\infty - T_{aw}}{T_\infty - T_c} \tag{1.2.5}$$

The adiabatic effectiveness is often presented as a lateral average, $\bar{\eta}$, but it is also important to look at contours of η in order to best understand the coolant distribution. The most directly relevant η data to this study was that of Johnston *et al*. [9]. They used nominally the same geometry as this experiment, but with different mainstream turbulence. Their *Tu* was alternately ~0.5% and 17%, while this experiment had a *Tu* value of 5% [10]. A new adiabatic test was undertaken for this study, in order to compare to Johnston *et al*.

One issue with adiabatic effectiveness results is the fact that introducing coolant jets to the mainstream tends to “blow away” the boundary layer along the surface, increasing the heat transfer coefficient. This is especially important near

the leading edge, where the boundary layer is often laminar. For this reason, the ratio of heat transfer coefficient with film cooling, h_f, and without, h_0, is another useful parameter for evaluating film cooling. The former has already been defined using Equation 1.2.4, and h_0 is defined by:

$$h_0 = q_0''/(T_w - T_\infty) \tag{1.2.6}$$

Where q'' is defined as positive out of the surface. Yuki and Bogard [11] showed that in the leading edge region, heat transfer augmentation could be as high as 60% in some locations near the jet exit; even further downstream values were in the 20% range. It is clear then that the effects of heat transfer augmentation are quite significant, and they must be taken into account when comparing film cooling designs.

It is necessary then to combine the effects of heat transfer augmentation and adiabatic effectiveness. A convenient method for combining these parameters was proposed by Mick and Mayle [12]. They combined Equations 1.2.4 and 1.2.6, and arrived at:

$$\frac{q_f''}{q_0''} = \left(\frac{h_f}{h_0}\right)\left(1 - \frac{\eta}{\phi}\right) \tag{1.2.7}$$

This equation allows predictions to be made about the surface heat flux. A slightly different formulation was proposed by Sen *et al*. [13], resulting in the net heat flux reduction (NHFR) parameter, as follows:

$$NHFR = 1 - \left(\frac{h_f}{h_0}\right)\left(1 - \frac{\eta}{\phi}\right) \tag{1.2.8}$$

Like the heat flux ratio, this equation is useful in examining the impact of coolant jets on the surface heat flux. However, several important assumptions were made in the formulation of these parameters. First, the parameter ϕ in these equations represents a non-dimensional metal temperature defined by:

$$\phi = \frac{T_\infty - T_w}{T_\infty - T_c} \tag{1.2.9}$$

In order to arrive at Equations 1.2.7 and 1.2.8 both T_c and T_w must be assumed to be the same with film cooling and without. For T_c this is a moderate assumption; while there is some heating of the coolant on the way through the model, it is still closer to the original coolant temperature than to that of the mainstream. However, the assumption that T_w is the same in both cases is quite substantial. It implies that film cooling produces no change in the metal temperature, which is the primary design goal of film cooling designs. Further, this temperature must also be assumed since it is generally unknown. It has historically been assumed to be 0.6, which is often quoted as “typical” for engine

designs. Lastly, even if in theory NHFR correctly combines heat transfer augmentation and film cooling effects, it does not give a surface temperature distribution. To obtain this, a FEM must be run using NHFR and internal cooling as boundary conditions to predict a metal temperature.

Given the nature of the assumptions that have gone into the prediction of a surface temperature using adiabatic models, it is advantageous to provide a means of directly predicting the temperature distribution on a simulated engine part. This is possible by using ϕ instead as a non-dimensional surface temperature described as “overall effectiveness”, which can take into account all aspects of cooling design. Obtaining a realistic value of this parameter is non-trivial (which is why adiabatic models have been and still are very popular) and the process required is described in the next section.

Assuming that conditions have been met to obtain overall effectiveness, there are many geometric parameters that define the shape of a given model which must be matched to engine dimensions. These are generally non-dimensionalized using the coolant hole diameter. Of particular importance to this study is the hole pitch, reported using *p/d*. The pitch is the distance between two coolant hole centerlines on the surface of the blade in the cross-stream direction. This parameter is important because it strongly impacts coolant distribution on the surface.

1.2.2 Hot Spots and the Matched Biot Number Model

The measure of actual surface temperature distribution can be accomplished using a model with a matched Biot number, *Bi*. The Biot number represents the ratio of convective heat transfer to conductive heat transfer at the wall. For a cylindrical surface *Bi* is defined:

$$Bi = \frac{h_f (r_o - r_i) \ln\left({r_o}/{r_i}\right)}{k_{solid}} \tag{1.2.10}$$

Adiabatic effectiveness tests require matching *Re* and *Pr* for engine conditions in order to be applicable. A conductive model needs to also match *Bi*, since the conductivity of the material should be appropriately scaled. Albert [14] showed that, with an assumption of one-dimensional heat transfer through the airfoil material, and using the definition of *Bi*, the surface temperature can be expressed as:

$$\frac{T_{aw} - T_w}{T_{aw} - T_c} = \frac{1}{1 + Bi + {h_f}/{h_c}} \tag{1.2.11}$$

Albert used the parameter h_c to represent a combined heat transfer coefficient from through-hole convective cooling, h_h, and cooling on the interior surface, h_i. His analysis showed that matching Biot number would produce an appropriate comparison to actual engine part surface temperatures by using ϕ.

Various estimates place the Biot number for engine conditions in the 0.1 to 0.4 range [14], [6]. Johnson [15] further reduced Equation 1.2.11 to express ϕ in terms of other non-dimensional parameters,

$$\phi = \frac{1-\eta}{1+Bi+{h_f}/{h_c}} + \eta \qquad (1.2.12)$$

As long as all these parameters are matched to engine conditions, the measured value of ϕ will be representative. Since Albert's work, Mouzon *et al.* [16], Terrel *et al.* [17] and Maikell *et al.* [18] have all successfully employed the matched *Bi* process on a leading edge to obtain useful ϕ results. Data were presented as both lateral averages, $\bar{\phi}$, and as contour plots. Their results have shown that conduction effects drastically smear out temperature gradients on the surface, as demonstrated by Figure 1.2.3. The points between the cooling holes are still much warmer than other areas, but the magnitude of the difference is much reduced. This figure shows the true "hot spots" between cooling holes. This temperature could be considered the limiting temperature in a blade design. A general rule of thumb in turbine design is that a change in surface temperature of 70° F might halve part life. This equates to a change in ϕ of approximately 0.05. Even one contour level in Figure 1.2.3 might represent this level of difference, so an examination of the minimum overall effectiveness, ϕ_{min}, is critical. Adiabatic effectiveness only provides an estimate of the location of these points, but overall

effectiveness measurements can determine the actual location and relative surface temperature.

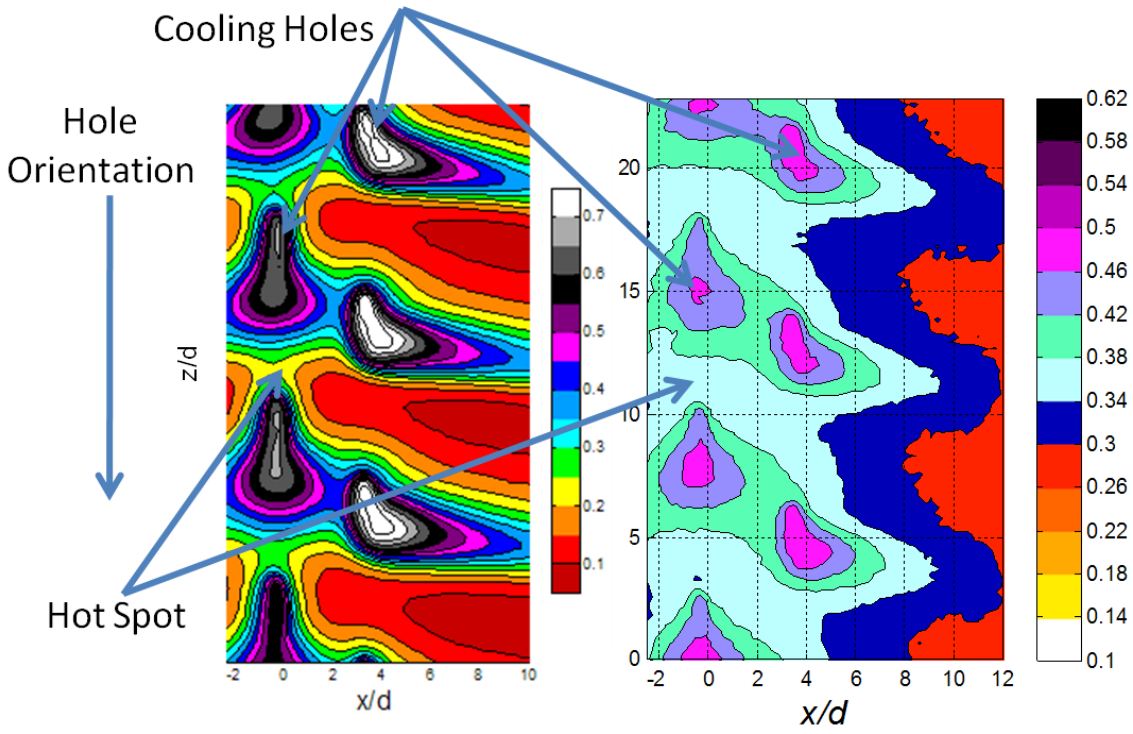

Figure 1.2.3: Comparison of contours of η and ϕ for a leading edge model with *p/d* = 7.6, *M* = 1.0, α = 0° and *DR* = 1.5

The surface temperature can be viewed as being affected by three heat flux values: flux into the surface, q_f'', flux through the cooling hole walls q_h'' and flux through the internal wall q_i''. These fluxes are shown in Figure 1.2.4. This approximation treats any flux from the wall into the coolant on the external surface as a reduction in overall q_f''. The energy balance along the surface is then expressed by:

$$Q_f = Q_h + Q_i \tag{1.2.13}$$

The contribution of q_h'' to cooling in the showerhead was explored by Terrel *et al*. [17], who found that between 30 and 80% (depending on *M* and internal cooling arrangements) of the total cooling was achieved by convection within the holes. The dominance of through-hole convection suggests that conduction through the solid from the hole walls is the largest factor in determination of surface temperature.

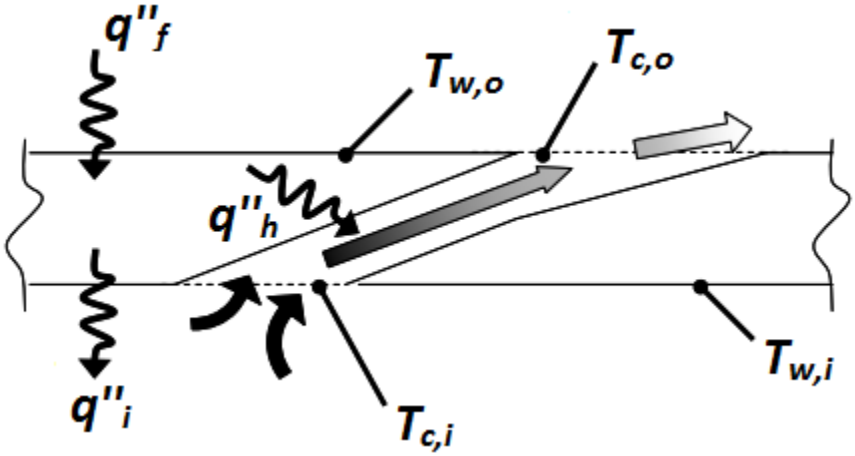

Figure 1.2.4: Simplified representation of the flow of energy around a cooling hole [6]

Because the location of holes in the showerhead region is so important, and large amounts of coolant are expended there, optimizing the showerhead design could lead to substantial coolant savings. There are many parameters that can be changed to alter the showerhead's cooling performance. One

parameter of particular interest is the hole pitch. In general, a very close pitch is used in order to provide the best coverage.

Schmidt *et al*. [19] tested η on two pitches, *p/d* = 3 and *p/d* = 6. They used a flat plate with compound angle holes (not at the 90° usually seen in the showerhead, but angled at 60°) and saw significant regions of low effectiveness between the holes at the larger pitch. Additionally, they showed that, at a variety of blowing ratios, the values of $\bar{\eta}$ and $\bar{\bar{\eta}}$ dropped by approximately 50% when the pitch was doubled. Local values of η dropped much more as coolant failed to completely cover the model. This serves to give an idea of the level of impact pitch variation might have, but no data concerning the leading edge region could be located.

This sort of reduction in η, directly proportional to the increase in pitch, is not surprising. The corresponding increase in q_f'' is expected to increase the surface temperature, but no study using a conducting model has explored the variation in pitch.

Mouzon *et al.* [16] varied internal impingement cooling through the use of different jet Reynolds numbers, Re_j. Jambunathan *et al*. [20] showed that there is very strong support for a power relation between Re_j and heat transfer coefficient. Mouzon *et al*. should have dramatically changed q_i'', but found little effect on ϕ. Their study is, however, the only one that could be found making use of a conducting model in measuring impingement on the leading edge.

A very recent computational study looked at this study's baseline geometry. In their paper, Ravelli *et al*. [21] explored the relationship between the three heat flux values, q_f'' ,q_h'' and q_i'', as defined in Figure 1.2.4. They showed that increasing h_i through impingement cooling increased q_i'' by a factor of three. However, the increased coolant-hole inlet temperature caused q_h'' to decrease. The implication is that it is possible that the balance between the change in internal cooling and cooling from through-hole convection acts to prevent changes in q_i'' from greatly affecting surface temperature.

1.3 Objectives of Current Study

It has been established that while previous studies have investigated ϕ distributions, they did not focus on the high temperature regions between the holes. One of the main goals of this study was to examine this area using the minimum overall effectiveness, ϕ_{min}. This analysis will highlight any localized hot spots, which are very important in thermally limited turbine parts. It was hoped that new insights could be obtained through examination of this parameter.

In order to further examine the heat flow through the leading edge, a major goal was to measure the heat flux on the interior and exterior of the model directly. The result would be a more detailed understanding of q_f'' and q_i'', and, through them, q_h''. The impingement condition was changed from a baseline case to a case with no internal impingement, just as Mouzon *et al*. [16] did in their study. Measurement of the heat fluxes would also allow h_0, h and h_i to be

determined without resorting to the constant heat flux wall condition assumption generally relied upon when finding these values on an adiabatic surface. Small heat flux gauges were purchased for installation, and part of the objective of this study was to determine how to use these new instruments, and measure heat flux at various locations on the internal and external surface.

However, the primary objective of this study was the evaluation of the affect of pitch variation on a matched *Bi* model. It is desirable to spread out cooling holes as much as possible without compromising cooling in order to reduce coolant use and manufacturing cost for an engine part. To this end, the pitch of the holes would be varied while holding all other factors constant. Using matched *Bi* models and the new ϕ_{min} parameter would allow the pitch to be optimized. The comparison of ϕ_{min} was particularly important, because it was predicted that pitch variation would more strongly affect this parameter.

2 Experimental Facility and Procedure

This section provides a detailed description of all facilities, experimental apparatuses, and models used in the course of generating the data presented in this thesis. The procedures for performing experiments and reducing the raw data are also examined. Lastly, an analysis of the uncertainty in measured quantities is presented.

2.1 Wind Tunnel Facility

The TTCRL facility used for this study was an Engineering Design Laboratory, Inc. closed-loop wind tunnel. This tunnel had been modified and built upon extensively over the years to arrive at the configuration shown in Figure 2.1.1.

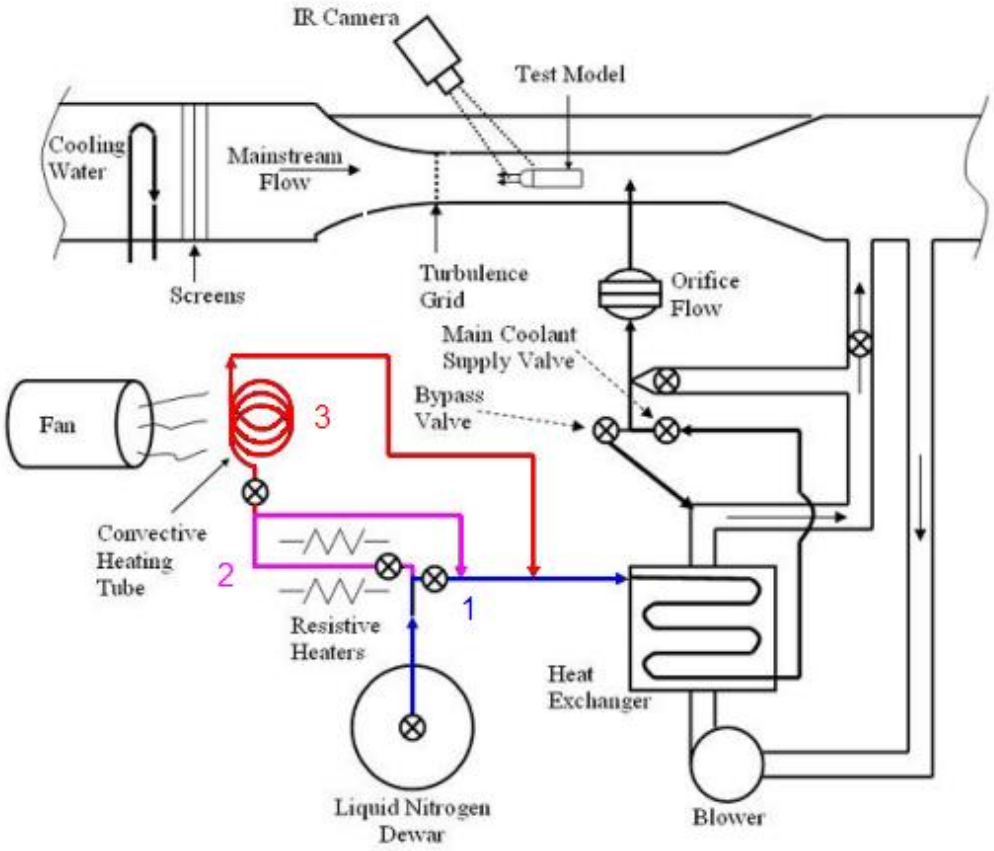

Figure 2.1.1: Abstract diagram of TTCRL's small wind tunnel facility

The flow was driven by a 5hp axial fan (not pictured). A water-to-air heat exchanger helped to maintain a steady mainstream temperature. Downstream of this exchanger was a series of honeycomb screens and a 9:1 area contraction which acted to reduce *Tu* to about 0.5%. The flow then entered the test section, which was a rectangular passage measuring 6" by 24" (15 x 61 cm) in which the model was centered. In order to better approximate engine conditions, a turbulence generating grid was used to produce an increased value of *Tu*. This level was measured as 5% slightly upstream of the model's location, with an

integral length scale of 2.3 cm [10]. This was within bounds for operating conditions in an actual gas turbine engine for a first stage blade. Mainstream velocity was uniform within 5% of nominal, resulting in a corresponding change in *Re* across the span of the model. U_∞ was maintained at a constant 15 ±0.3 m/s, or *Re* = 50000.

Nitrogen gas boiled from a liquid state was supplied as coolant. The temperature of the coolant was controlled through increasing the path length, depicted as 1, 2, and 3 in Figure 2.1.1. The coolant also traveled through an air-to-air heat exchanger driven by a 7.5hp constant speed centrifugal blower. This blower could be turned on and off as desired to generate additional warming. The amount of air driven through the heat exchanger was governed by a bypass valve. For small adjustments, a low power box fan was also used to force air over some of the piping. Lastly, a bypass valve in the coolant line allowed the mass-flow through the majority of the system to remain constant while the mass to the model was reduced. This prevented the temperature from increasing excessively at low values of *M*. Both *DR* and *M* could be varied as desired. All experiments were run under a constant *DR* of 1.5 ±0.05, while *M* was varied. *DR* was maintained within ±0.01 during data collection to aide in achieving steady state.

Before passing through the model, the coolant traveled through an orifice flow meter. This sensor allowed the measurement of the coolant flow rate from which *M* was calculated.

2.2 Test Model Assembly and Instrumentation

The actual test pieces used in this study were made from two different conducting materials and low conductivity foam using two different processes. Both are described here, in addition to the instrumentation procedure and a description of the complete test assembly, and the model geometry.

2.2.1 Geometric Parameters

External parameters defining the model for this study including: pitch, relative curvature, and hole length are non-dimensionalized using the coolant hole diameter, d. Internal parameters, jet-to-target spacing, impingement plate thickness, internal Nusselt and Reynolds numbers, are defined using the impingement cooling jet diameter, d_j. It should be noted that t and ζ are not typically used for plate thickness and jet-to-target spacing in the impingement literature. These symbols have been chosen to prevent confusion with symbols used in definition of external parameters that are not generally considered when investigating impingement cooling. Figure 2.2.1 illustrates every parameter except for the angle of attack, α. The definition of the coordinate system used for comparison of results is also shown. Lateral averages presented are values averaged in the z direction.

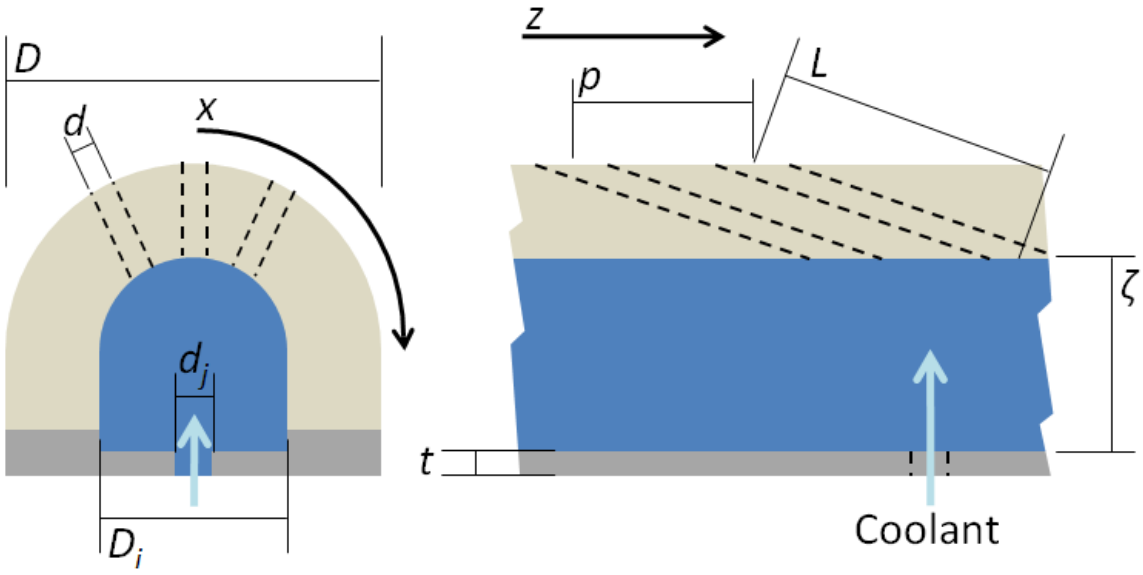

Figure 2.2.1: Diagram of some dimensions and coordinates used to define a leading edge model

Each parameter used to produce the models is described in Table 2.2.1. The models consisted of three rows of cooling holes positioned as shown in Figure 2.2.2. The cooling holes were positioned on the surface such that the off-stagnation hole centerline was exactly one half pitch from the stagnation row hole centerline.

Table 2.2.1: Geometric definition of some parameters for the leading edge model

Geometric Parameter	Value(s)
p/d	7.6, 8.6, 9.6, 11.6
D/d	16
L/d	11.7
D_i/d_j	5
t/d_j	0.625
ζ/d_j	5.2

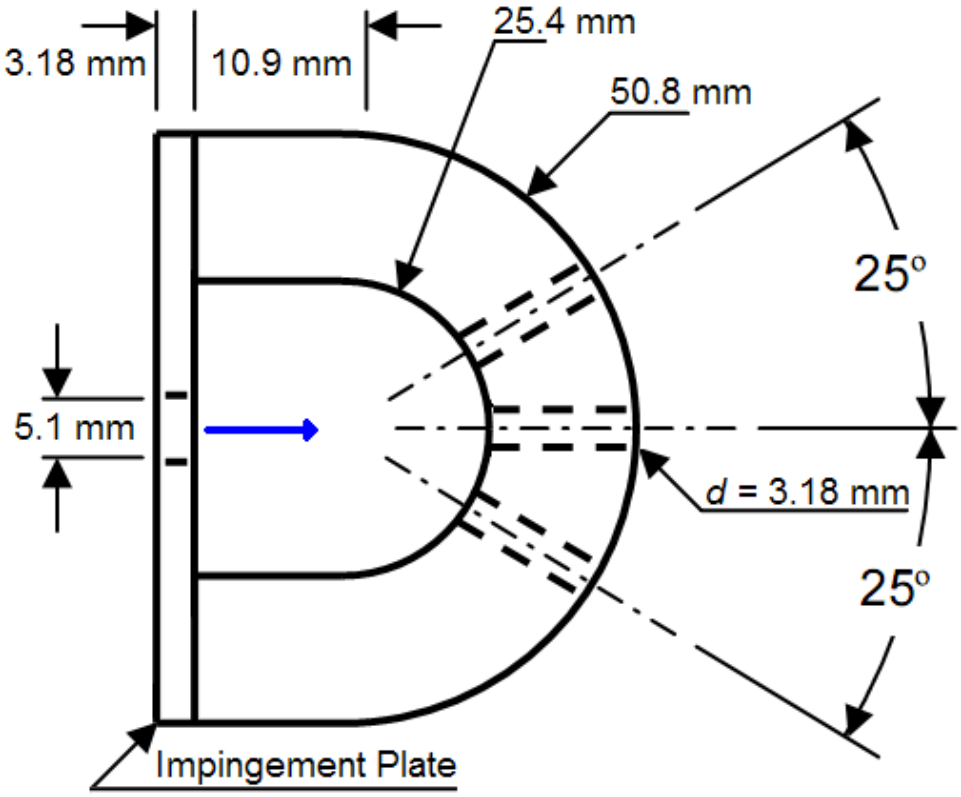

Figure 2.2.2: Diagram of the leading edge model

As depicted above, the half cylinder portion ends in a flat region. This flattened region continued downstream in the coolant supply, which formed a bluff body.

2.2.2 Polycast Leading Edge Model

The majority of the models used were cast from Polycast PC 287, a commercial epoxy selected for its thermal properties, and because it could be cast and machined in-house. Maikell [22] reported that the conductivity of the material was 4.3 W/mK, but this was based on the manufacturer's spec sheet.

During the course of Dobrowolski's study [23], it was discovered that this specification was likely based on a theoretical model and not on experimental testing. She experimentally determined that the actual conductivity of the material was 1.04 W/mK ±6%.

Maikell [22] previously cast the material in a mold first used by Albert [14] to produce adiabatic models. Maikell designed an aluminum insert and back plate that allowed the shape to be cast. However, the mold was cracked and no longer maintained dimensional tolerances. Additionally, the possibility of mold blowout due to inadequate sealing between the SLA front piece and the aluminum backing plate prompted a complete redesign of the mold.

A new mold was designed from all aluminum pieces that could be fitted together and held in place with bolts, as pictured in Figure 2.2.3. The new mold not only allowed better tolerances, it reduced the time required to produce a new leading edge model in several ways. First, the mold could be assembled and filled on the same day since it closed tightly, requiring no additional sealant. Second, because the internal surface of the mold was much smoother, sanding was no longer required to eliminate surface roughness before use.

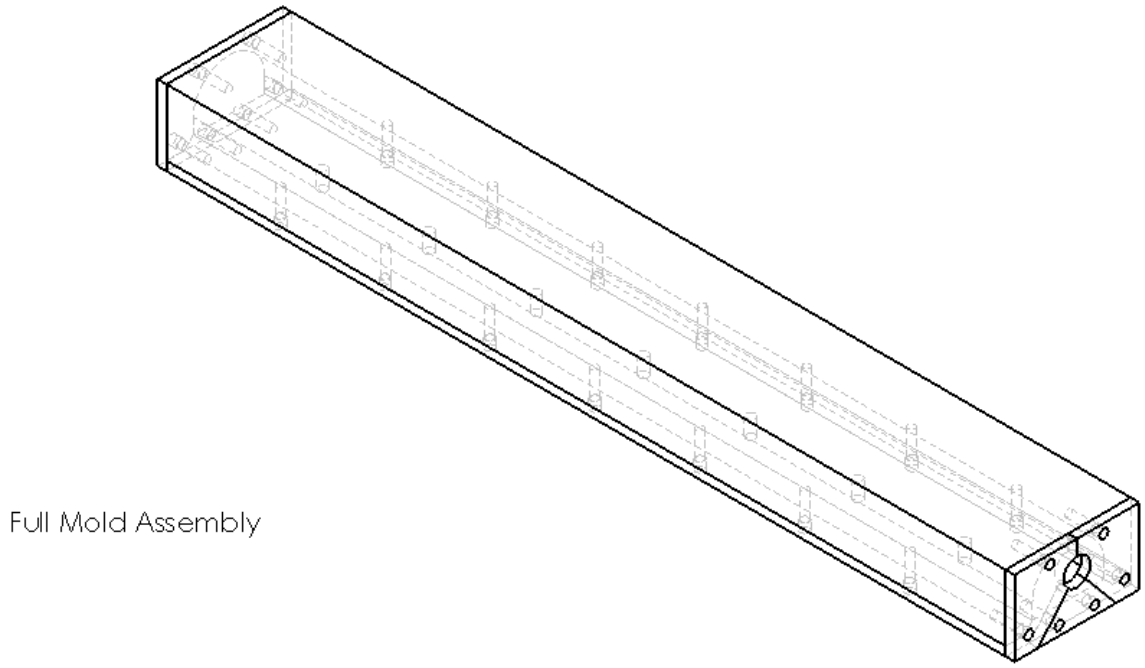

Figure 2.2.3: Diagram of the new aluminum mold without the internal radius piece

The inner radius insert was first attached to the backing plate and then tape was applied to prevent the liquid epoxy from seeping between the parts. Though this was determined to be unnecessary with the new mold, the surface produced by the tape was much smoother and facilitated the demolding process. Liberal application of Mann Ease Release 200 mold release remained part of the assembly procedure. Although it was now possible to pour the whole mold at once, it was determined that multiple small pours were still required in order to prevent air inclusions.

The new mold required only slight modification to the original demolding procedure. First, the end caps are unscrewed and knocked off. This sometimes required some light hammering on the sprue-hole end due to excess material

binding the cap to the rest of the mold. Afterward the backing plate was unscrewed from the mold and aluminum insert. Small spacer blocks were placed between the plate and the model to allow force to be applied. Successively more inserts were used as the screws were slowly tightened and the model was withdrawn. Once the model was level with the top of the mold, the inserts were moved to block the motion of the model and allowed the aluminum insert to be removed. The result is illustrated in Figure 2.2.4.

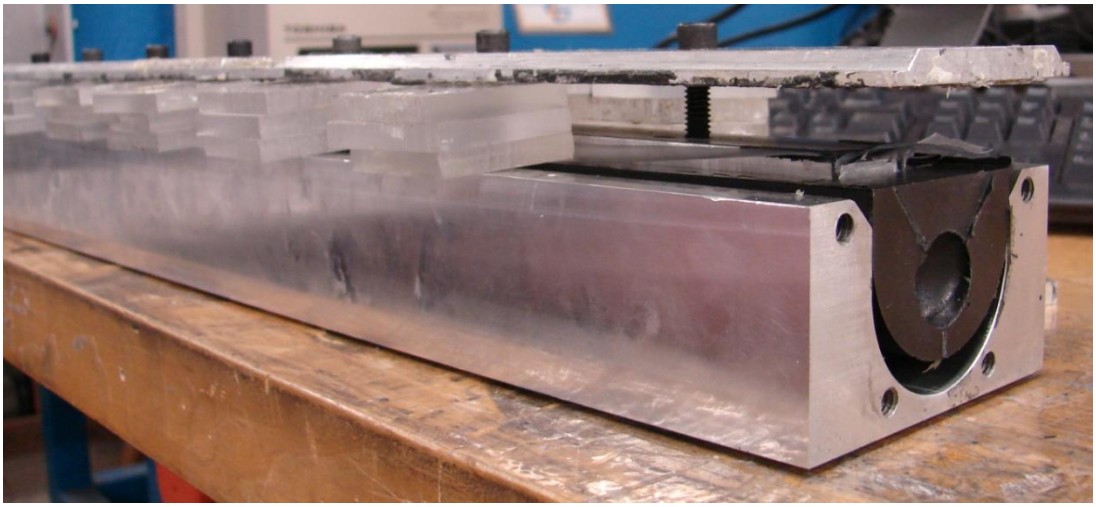

Figure 2.2.4: The end stage of withdrawing the inner radius insert from a new part

Sometimes the model would remain stuck in the mold at this point. It was found that some light hammering with a rubber mallet could move the model enough in the mold that it could be pried out without using a lever that could scrape the inside of the mold. To prevent damage to the new back plate, the old back plate was used during the removal process.

Once extracted, the model was machined as desired. The epoxy material is quite difficult to work with, being extremely hard, brittle, and abrasive. Typically a drill bit could not be used for more than a few holes before the tip was completely worn away. However, diligent effort on the part of the machinist obtained good results.

2.2.3 Corian® Leading Edge Model

Corian is a material most often used in producing countertops. It happens to have a thermal conductivity measured by Emily Pfautsch at 0.97 ±0.1 W/mK, making it suitable for use in matched *Bi* experiments, and comparable to the Polycast material.

Corian could only be obtained in ¾" sheets. In order to produce a leading edge model with the correct dimensions, two sheets were bonded together using a special adhesive designed for use on Corian. This special glue produced very strong bonds with a very thin interface, so any defect in conductivity was not noticeable. Once a piece was prepared it was machined using a CNC mill. The holes were then drilled by hand on a separate milling machine. Experiments performed by Jason Albert with p/d = 8.6 confirmed that there was no measurable difference in ϕ between models made from the two materials. An example comparison of the materials is presented in Figure 2.2.5. The p/d = 11.6 data presented in this report made use of this material.

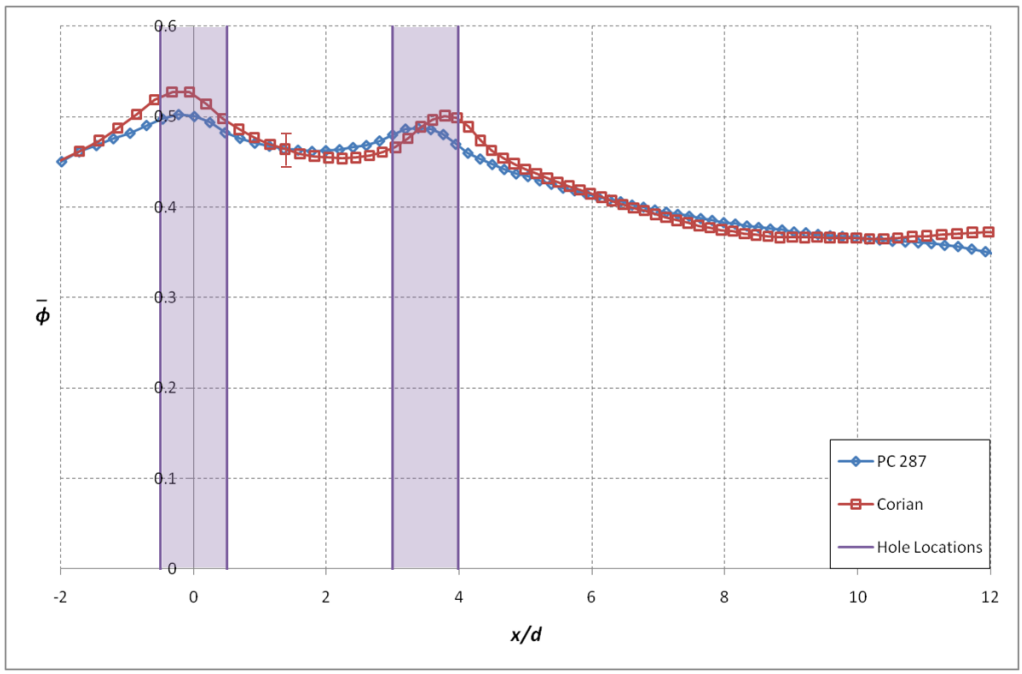

Figure 2.2.5: Comparison of two model materials at *p/d* = 8.6, *M* = 2 and *DR* = 1.5

2.2.4 Adiabatic Leading Edge Model

Although Johnston *et al*. [9] studied nominally the same geometry as used in this study (*p/d*, hole angle, and *D/d* were all the same), important differences exist in how the data were acquired. Johnston *et al*.'s model used a ¼ cylinder attached to the bottom of the wind tunnel; making use of bypass suction to make sure the streamlines along the "stagnation" row of holes were parallel to the wall. There was some question as to whether or not this produced a truly representative velocity field, which was why part of the goal of the current study was to measure these data using a full cylinder placed in the center of the test section. Additionally, the mainstream turbulence levels of Johnston *et al*. were very different than those used during measurement of ϕ (they were typically

much higher). For these reasons, a new model having the same dimensions as the conducting models was machined out of a low conductivity foam (k ~ 0.048 W/mK). The foam was machined from a block using a CNC milling machine. Afterward, the holes were added by hand on a different machine.

Testing procedure, instrumentation and data processing were all the same for the adiabatic model. It should be noted that there was some small amount of conduction taking place through the foam. However, the nature of the leading edge model made it very difficult to measure this conduction error. Estimates from Dobrowolski's [23] computational study predicted that the conduction error was approximately 0.05 between the rows of cooling holes, and dropped off rapidly to very small values downstream of the off-stagnation row.

2.2.5 Model Instrumentation

As one goal of this study has to do with internal flow and internal surface measurements not normally visible, a large number of instruments needed to be attached to the internal surface before assembly of the test model could be completed.

A "grid" of E-type thermocouples constructed from flat ribbon material was installed on the inner surface of the model, as shown below. Results obtained from these sensors were used as a boundary condition in Dobrowolski's [23] computational study.

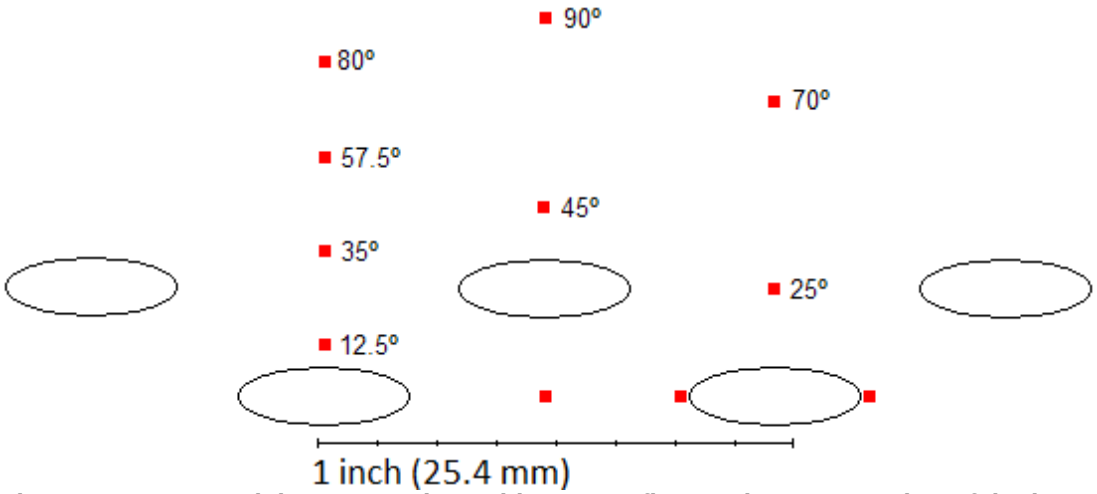

Figure 2.2.6: Internal thermocouple positions on a flattened representation of the inner surface of the leading edge model

Additionally, several RdF micro-foil heat flux gauges were installed on the interior. These sensors were capable of measuring heat flux directly, and had a small form factor. Each gauge was approximately 1.5x3 mm and 0.20 mm thick. These were the smallest gauges of their type available at the time. They proved to be somewhat unreliable (as described in section 2.3) so three pairs of gauges were installed. One pair was located on the stagnation point under the impinging jet, similar to where the 0º temperature sensor was positioned. Another pair was positioned at 45º where a corresponding temperature sensor was located on another pitch. The last pair was installed at the 70º position. Locating the gauges at similar positions to the interior thermocouples served two purposes: the surface temperature must be known to calculate h_i from q_i'', and the flux reported by the gauge was sensitive to the temperature of the gauge.

On the exterior surface there were two thermocouples placed so that they would be visible by the IR camera during the experiment. This was important for calibration of the camera, as described in section 2.2.7. Other thermocouples were positioned on the exterior surface to match the position of heat flux gauges placed on the exterior.

2.2.6 Coolant Supply Plenum and Impingement Plates

Once instrumented, the model was attached to the coolant supply plenum, which was designed and built by Albert [14], and is depicted in Figure 2.2.7.

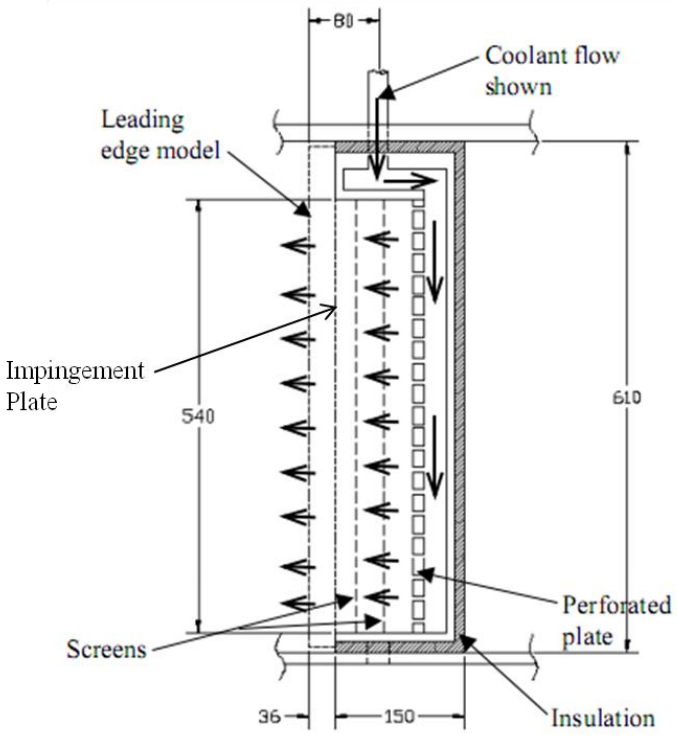

Figure 2.2.7: Coolant supply plenum. All dimensions are in millimeters.

The plenum was designed to evenly distribute the flow so there would be little span-wise variation within the model. This supply was somewhat modified by Mouzon [24]. An aluminum backing plate was installed that allows the use of various impingement plates.

For this study, an impingement plate made from aluminum was chosen. The plate had holes spaced with the same pitch as the model, but offset ½ pitch so that the impinging jet impacted directly between the film-cooling holes at the stagnation line. The diameter of the holes was 0.2" (5.08 mm), so the plate's p/d_j was 4.75. This plate was chosen because a large number of previous experiments in this lab have used it to simulate internal cooling.

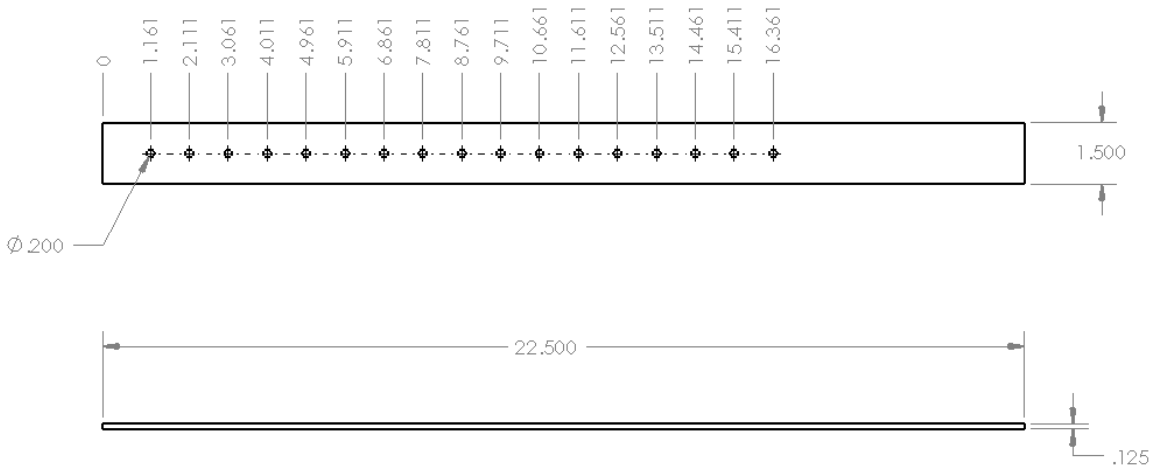

Figure 2.2.8: A schematic of the *p/d* = 7.6 impingement plate geometry used for this study. Dimensions are in inches.

A second plate having the same dimensions was manufactured from acrylic (k = ~0.2 W/mK). The purpose of this plate was to assess the possible

bias from coolant warming due to interaction with the impingement plate. The impingement plate was attached directly to the aluminum backing plate, which was in turn exposed to the mainstream flow.

Another issue faced during measurement of the adiabatic effectiveness was the use of the correct coolant temperature. Initially the same sensor used to measure T_c for the conducting models was used for the adiabatic model as well. However, it was discovered that there was a significant temperature rise downstream of the impingement cooling plate. This temperature increase was a function of blowing ratio, leading to the assumption that the impingement cooling plate might be affecting surface temperature by "pre-warming" the coolant in the conducting model as well. The plastic impingement plate was designed to assess whether or not this was indeed a significant contributor to overall effectiveness. This plate is shown as installed in Figure 2.2.9. A final case used no impingement plate as a "low h_i" case.

Figure 2.2.9: The plastic impingement plate offers at least one clear advantage

2.2.7 Infrared Cameras

Two FLIR Systems cameras, models P20 and P25, were used for collecting external surface temperature. The operation and calibration of this camera was covered extensively by Maikell [22], and no changes were made to his procedure, though extensive effort was undertaken to verify that the best calibration was used when comparing the data.

Because the test section was composed of paneling that is opaque to infrared frequencies, there were two windows, depicted in Figure 2.2.10, built into test the section composed of materials translucent to IR radiation. The interior window was composed of salt crystal. Because salt crystal loses its transmissive quality through absorption of humidity, the external window was composed of

Zinc Selenide. The calibration of the camera compensated for the transmissivity being less than one.

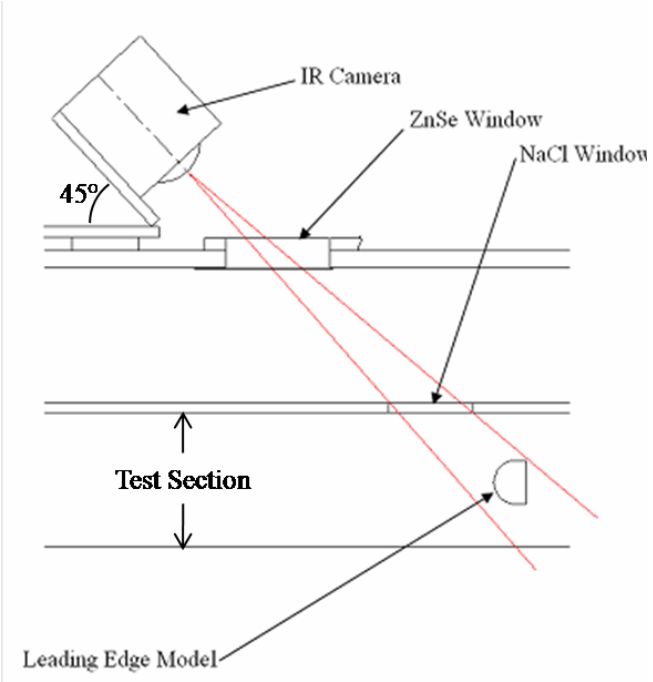

Figure 2.2.10: Representation of the IR camera setup used to observe the leading edge model

During the course of this study, it was found that the calibration of the camera had changed subtly from Maikell's [18] "standard" calibration. The probable reason for the change is that a new salt crystal window was installed. Over the course of many tests, a new database of calibration data, some of which is shown in Figure 2.2.11, were obtained and used to create a new standard calibration that was applied to all the data gathered for this study. The scatter in the data is not indicative of the uncertainty in the surface temperature;

rather, it represents uncertainty from the calibration procedure. The temperature of a given point in the IR field was very stable, but significant uncertainty from locating the calibration thermocouples in the field of view leads to scatter in the data. Combination of many tests worth of data was necessary in order to reduce this source of error. Waye[25] and others have shown that using a standard calibration produces substantial improvement in comparability between experiments. Calibration was thought to still be a significant contribution to the total uncertainty, and efforts to improve this procedure are ongoing.

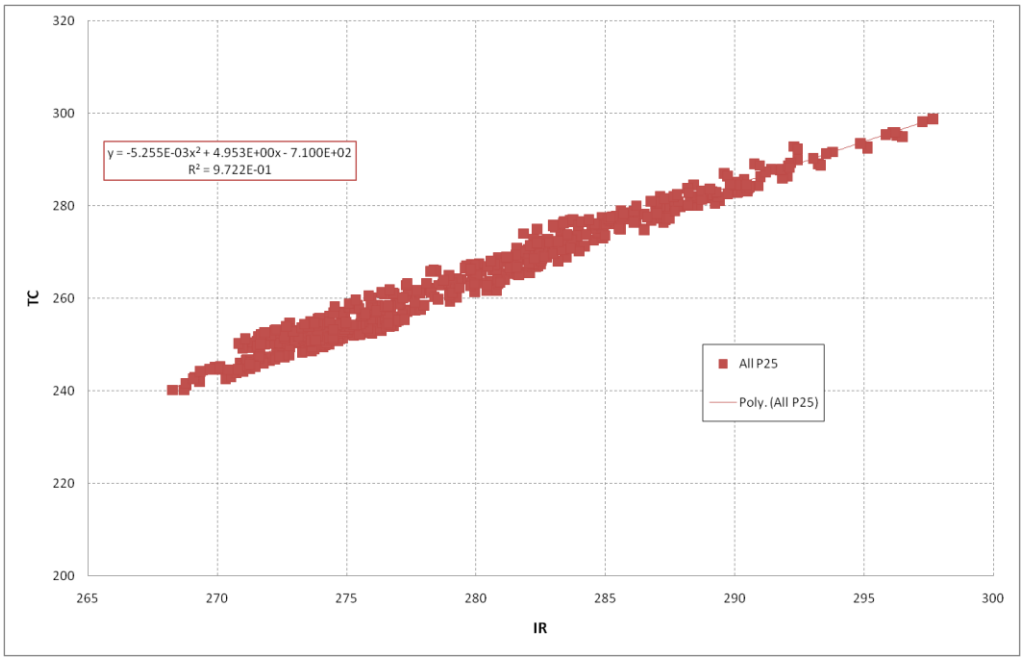

Figure 2.2.11: Database of points used to generate the new standard calibration curve for the P25 camera

Another camera was positioned on the side of the test section in order to observe the full length of the model. This vantage point was important for verifying that the model was at an angle of attack of 0º. The method used was to line up the side-view camera on the model and observe how the coolant streaks were distributed over the surface. The model was considered to be at 0º when the coolant distribution from the row of holes positioned on the stagnation line was visually symmetrical. No temperature data were used from this camera, so there was no need to calibrate it.

2.3 Heat Flux Calibration Apparatus and Procedure

Though the RdF heat flux gauges came with a calibration from the manufacturer, this calibration was not traceable to any sort of standard and came with no uncertainty values. Additionally, a method to attach the gauges to the surface in a manner that was repeatable and did not damage the gauges through repeated use was needed. In order to assess the uncertainty in the calibration and any affect on the calibration from the attachment procedure, an independent calibration was performed.

The results verified that the manufacturer's calibrations were valid within at least 10%. However, during the course of testing it became apparent that the gauges' were being degraded, as increasingly they produced bad data or failed completely. The attachment process was identified as the most likely culprit. Because the gauges that still produced a usable signal had unknown

calibrations, the only way to extract useful data was to take the ratio of heat fluxes at two different conditions. The results could be converted to a ratio of heat transfer coefficients. The most useful ratio that could be measured was h/h_0. Unlike h_f/h_0, this parameter would be expected to decrease using film cooling.

2.3.1 Constant Heat Flux Plate

In order to calibrate the gauges and test out various attachment procedures, an apparatus was developed to produce a known heat flux. An easy and well proven method of generating a known constant heat flux is the use of a thin metal foil as a resistance heater. A voltage supply and a resistor of known resistance were attached to the plate as shown in Figure 2.3.1. The voltage supply was a Trilectron DC supply capable of producing large amperages. Initially, the resistance to measure current was 0.0033 Ω. However, the resistor was only rated for fewer than 15 A. It was determined that repeatedly exposing this resistor to up to 100 A had permanently altered the resistance. A new resistor capable of maintaining resistance within 0.25% at up to 100 A was ordered. The Crompton Instruments FN 928 used to replace the old resistor had a resistance of 3.33×10^{-4} Ω.

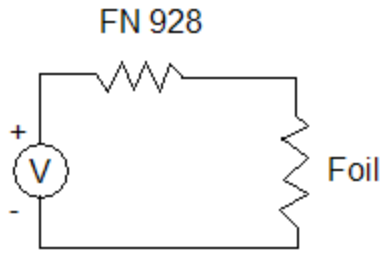

Figure 2.3.1: Circuit diagram of the constant heat flux apparatus

With voltage measured across both the known resistance and the thin metal foil, the power dissipated by the foil was easily calculated by the familiar equation, $P = IV$.

Flux was then calculated by dividing by the area of the plate (0.0338 m^2). This simple calculation only works if the plate can be assumed to have a perfectly adiabatic surface on one side. Another possible construction has the thin foil suspended vertically and a symmetric dissipation of q''. This setup was rejected because it made attaching the heat flux gauges in a repeatable manner exceptionally difficult. Therefore, an insulating backing was constructed to prevent as much loss through the back side of the foil as possible. The foam used for this purpose can be seen in pictures of the calibration apparatus presented in Figures 2.3.2 and 2.3.3. During calibration a measurement of the backside temperature allowed a correction to be applied to the flux value.

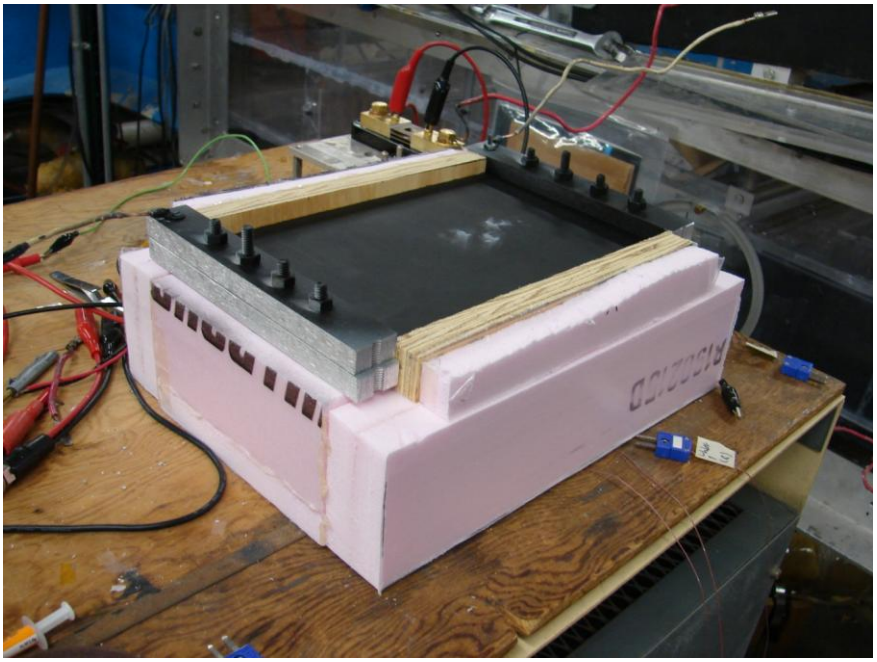

Figure 2.3.2: Constant heat flux plate

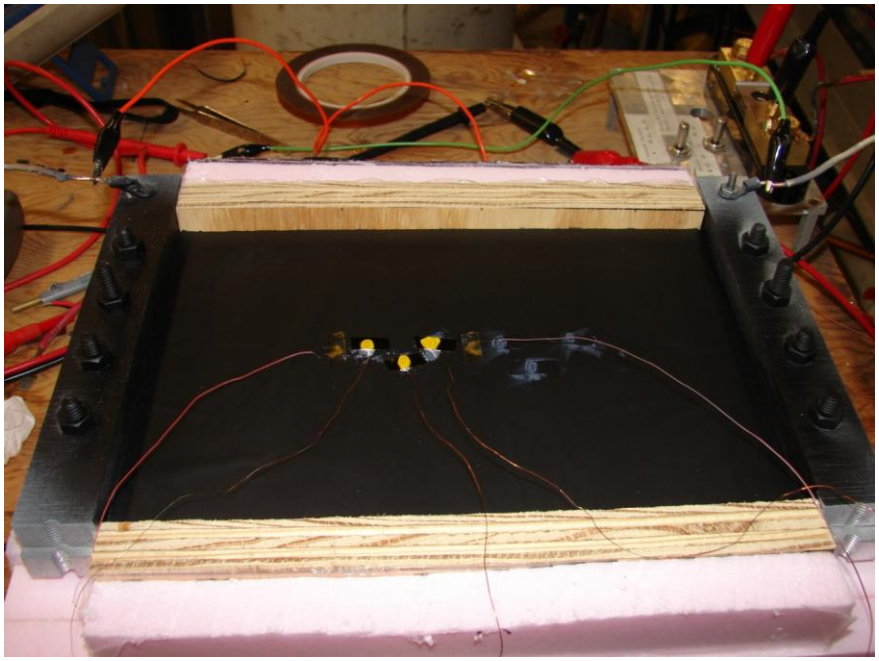

Figure 2.3.3: Constant heat flux plate with some instrumentation installed

The insulating material used was Owens Corning FOAMULAR®, a commercial grade housing insulation. This material degrades in performance and rigidity at temperatures in excess of about 90° C, requiring 1.5” (3.7 cm) of plywood in direct contact with the heat flux plate so that higher flux levels could be achieved. The foam has a thermal conductivity of approximately 0.028 ±0.002 W/mK (from the manufacturer specified R value). The conductivity of plywood is less certain, with most sources stating that it should be about k = 0.12. However, the bulk of the insulation (more than 85%) was provided by the foam, so the calculation of backside losses was insensitive to the conductivity of the wood. Foam thickness of 2.25” (5.7 cm) produced backside losses calculated to be less than 3% of the total power input. Even if the wood were a perfect conductor this percentage would be the same.

A thermocouple attached to the surface provided the temperature of the plate. It was assumed that this temperature would also represent the gauge temperature for the purpose of correcting the measured flux for changes in gauge sensitivity due to the change in material properties at different temperatures.

In addition to the wood backing, the plate also featured large bus bars that uniformly connect the heating foil with the current source. These large bars are solid aluminum pieces 0.25” thick with holes drilled every 1.2”. The bolts running through the bars were tightened such that the foil could not be shifted by hand. The resulting temperature distribution was uniform, varying by less than one

degree inside the area where the gauges were installed (shown in Figure 2.3.4) at a temperature difference with the air of about 70 K. The foil used was 0.002" stainless steel shim stock from TBI, who claim thickness uniformity of better than 5%.

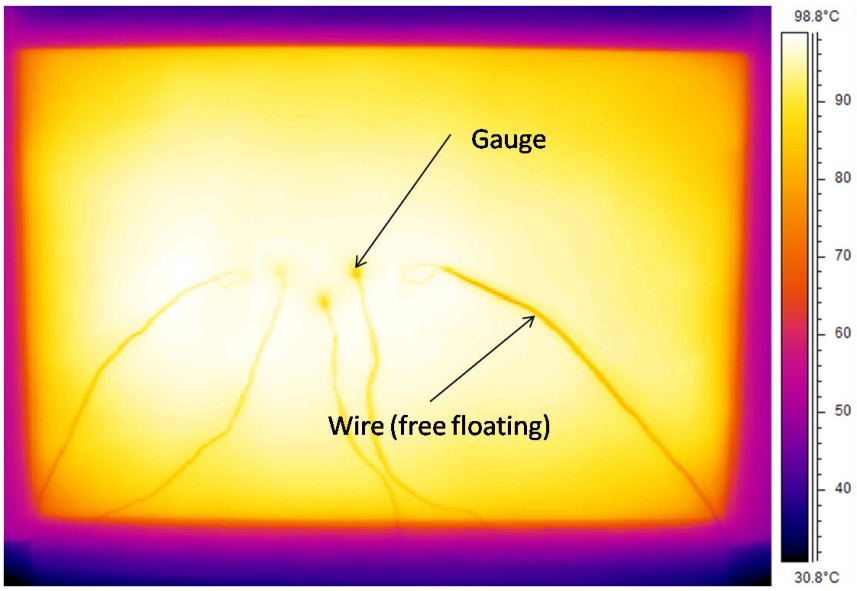

Figure 2.3.4: Raw IR image of the plate after 45 minutes at approximately 1300 W/m^2

2.3.2 Gauge Attachment Procedure

Initially the attachment method was to simply stick the gauges to the surface using a thin double sided tape that was estimated to provide very low thermal resistance. However, experimental results were not repeatable using this method, with test-to-test variations in the calibration constant for a single gauge sometimes as high as 60%. It was still evident that, whatever the calibration, it was always very linear with heat flux.

An improved method made use of thermal grease normally used in CPU heat sinks to fill in any gaps between the gauge and the surface. This grease was purposely designed to provide very low thermal resistance and improve contact between two surfaces. A small piece of tape was affixed over the gauge and stuck to the surface around it, using careful placement to avoid trapping any air. Additionally, the lead wires from the gauges were taped to the surface to prevent them from acting as fins. The fin effect is visible in Figure 2.3.4, where the gauges are clearly visible as cold spots on the surface. In comparison, Figure 2.3.5 shows an IR image from a calibration run with the wires taped to the surface. At the highest heat flux levels gauge surface temperatures were within one degree of the surrounding surface. The thermocouple visible in the image appears as a cold spot because it was unpainted. The temperature from the thermocouple was assumed to be the same as the gauge temperatures, and was used to calculate the adjustment to the gauges' signal due to temperature sensitivity, C_T. This factor was provided as a function of gauge temperature in °F:

$$1.06 - T_g 9.534093 \times 10^{-4} + T_g^2 1.164424 \times 10^{-6} + T_g^3 2.421347 \times 10^{-9} + T_g^4 1.138301 \times 10^{-11} - T_g^5 4.212063 \times 10^{-14} = C_T \quad (2.3.1)$$

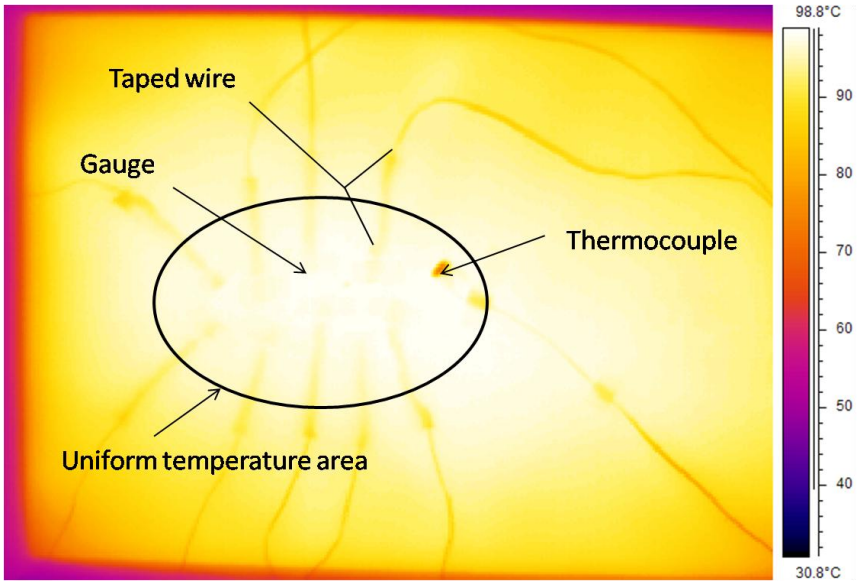

Figure 2.3.5: Raw IR image of the installed gauges with their wires taped down

Using this method the calibration was obtained by the relation,

$$C_g q'' = C_T(V - V_0) \tag{2.3.2}$$

where V_0 is the voltage measured at zero heat flux and C_g is the desired calibration constant, or gauge sensitivity.

Table 2.3.1 shows the sensitivities that were obtained using the methods described so far in this section compared to those provided by the manufacturer as a ratio. Ultimately, the gauges that produced the best results were those that had calibration ratio near to unity, indicating that the manufacturer's specification was generally correct.

Table 2.3.1: Measured calibration factors for all gauges

ID	Specified C_g (μV·ft^2·hr/BTU)	(C_g Measured)/(C_g Specified)
1	0.126	1.13
2	0.107	1.31
3	0.142	1.01
4	0.107	1.01
5	0.120	1.13
6	0.083	1.57
7	0.081	1.17
8	0.105	0.99
9	0.097	1.25

2.3.3 Model Installation Procedure

The preceding procedure worked well for calibrating the gauges, producing sensitivities that were very repeatable. However, the thermal grease did not stand up to cryogenic temperatures. The grease froze and dried into a fine powder. Presumably this powder did not have the same properties as the unfrozen grease, as initial results from the gauges installed in this manner were not realistic or repeatable.

A thermally (and electrically) conductive silver paint, most often used in electron microscopy, proved to provide sufficient bonding force to adhere the gauges to the surface. However, calibrating the gauges using the silver paint proved impossible with the existing calibration apparatus. An attempt was made, but the calibration constants were very different from those previously measured. Viewing the plate with the IR camera revealed that temperature wherever the silver paint was contacting the surface was significantly cooler than the

remainder of the plate. The calibrations that were obtained were consistent with the heat flux being less than usual, but because the conductive paint was changing the current density in an unpredictable way, actual flux was unknown. The assumption had to be made that the paint was not significantly altering the gauge sensitivity. However, to check the possibility that the paint was creating differing calibration constants, multiple gauges were placed in each position.

Repeated attachment and detachment of the gauges with the silver paint likely slowly degraded the gauge material. The thinning agent in the paint contains some solvents (acetone, benzene) that were never confirmed to be safe for use with the gauge material. Additionally, the paint thinner used to remove the gauges for repositioning was absorbed by the gauges, leaving them soft and more susceptible to damage. Absorption of the mineral spirits and dissolution of gauge material permanently changed the properties of the gauges, altering the calibration. Later examination of gauges that were never used with the paint confirmed that the gauge had been physically altered at some point during testing, making calibration changes during testing certain. Data taken early in testing (internal heat flux data) was still good, as that was the first exposure to the paint for the majority of gauges. However, during later tests more gauges failed, progressively reducing the number that could be relied upon.

At this point it was clear that heat flux on the external surface could not be measured directly, because the calibration was completely unknown, and was

likely changing between attachments. However, as previously mentioned, the ratio h/h_0 could still be measured.

In order to assure that the calibration constant did not change, it was required to leave the gauges in place to obtain h_0. Since the model that the gauges were attached to contained film cooling holes, the method for measuring h_0 was to very carefully fill the holes with clay (creating as smooth a surface as possible). With the holes blocked, the heat transfer coefficient could be obtained by cooling the model and measuring the flux again.

It would have been more desirable to measure the ratio q_f''/q_0'', but because of the method for blocking the holes, the internal cooling was compromised, so heat flux values would not be comparable. However, Dobrowolski [23] measured overall effectiveness on a conducting model cooled only by internal impingement (ϕ_0). When combined with the heat transfer coefficient ratio, this data allowed the heat flux ratio to be calculated by:

$$\frac{q_f''}{q_0''} = \left(\frac{h}{h_0}\right)\left(\frac{\phi}{\phi_0}\right) \tag{2.3.3}$$

This equation provided the opportunity to use this data to measure the real ratio of heat flux for film cooling to that without. This allowed the predictions provided by NHFR (Equation 1.2.8) to be evaluated.

2.4 Test Procedure and Data Reduction

A brief summary of the testing procedure for each geometry was as follows:

1. The tunnel was purged of excess humidity.
2. Desiccant packs were added to further reduce humidity to test levels (RH ≤ 5% was typical).
3. The camera was verified to be level relative to the model.
4. The model was verified to be at α = 0°.
5. The model was cooled to operating condition of *DR* = 1.5. During this period, data points were collected for calibration purposes.
6. Each blowing ratio was attained, usually starting with *M* = 2. Steady state was achieved by holding the model at constant flow rate for at least 5 minutes. Blowing ratio was considered constant if it varied no more than ±0.05 during a one minute interval, and was typically less than this. Density ratio was considered constant if it was within ±0.05 of nominal 1.5 and changed less than ±0.03 during the entire data collection period. For lower blowing ratios, as much as 10 minutes was required to obtain steady state. Afterward, examination of the data would confirm that steady state had been achieved.

7. The blowing ratio was returned to M = 2 and the angle of attack was varied. Steady state was found under angle changes in far less time, typically less than two minutes.
8. The model was returned to α = 0° in between positive and negative angles and at the end of the test.

Because each model was started at M = 2 and returned there several times throughout the test, this condition served as an in-test repeatability point. An example of in-test repeatability is shown in Figure 2.4.1. Because M = 2 was always repeated multiple times, it was also compared between tests to show test-to-test repeatability. The test-to-test points for p/d = 7.6 are shown in Figure 2.4.2.

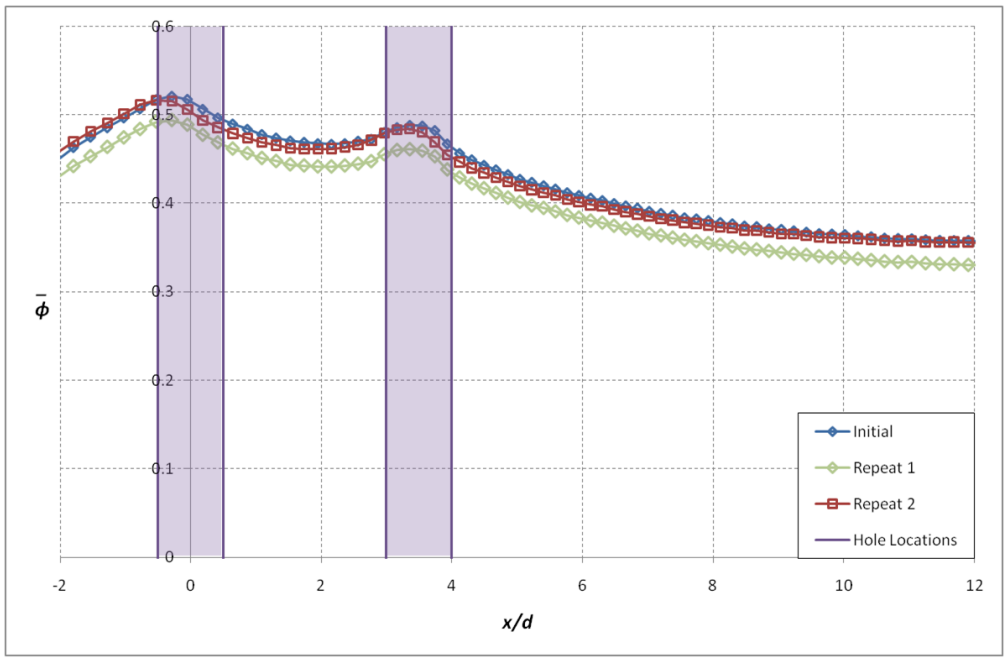

Figure 2.4.1: In-test repeatability for test ID 090406; *p/d* = 7.6, *M* = 2 and *DR* = 1.5

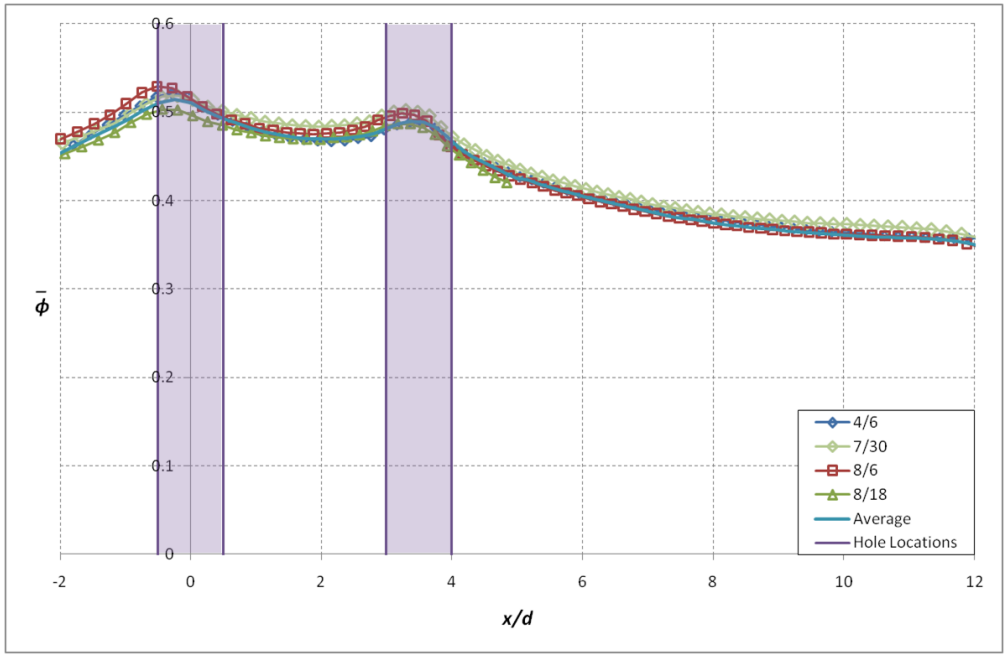

Figure 2.4.2: Test-to-test repeatability and the average value for *p/d* = 7.6, *M* = 2 and *DR* = 1.5.

The data reduction procedure used for this study was an evolution of the procedure described by Maikell [22]. The camera images are entered into ThermaCam Research Pro for preprocessing, locating TCs and defining the region for further processing by MATLAB.

The MATLAB program "blockscan," developed by TTCRL, was modified to find the hottest point in any given *x/d* line. However, there was some concern that pitch-to-pitch variation, while usually small, would produce unrealistic hot spot reports. Another TTCRL developed MATLAB program, "temp2phi," was modified to produce an average pitch. Using parameters entered into one of the input files, this program was able to determine the area of a single pitch and average all three available pitches into one. In turn, this was used to locate the "average hottest" spot along each *x/d* line. These points are presented as ϕ_{min}. The "temp2phi" program was also modified to allow for pitches other than *p/d* = 7.6.

Results from these two programs were input into an Excel spreadsheet. A template was developed to greatly speed the initial processing of the data. As previously mentioned, a new calibration was developed for the tests used in this study. This was accomplished using the thermocouple data gathered during the tests compared against the temperature readings from the IR camera extracted from the images. All the calibration data for the tests used in this study were combined and used to create a set of "standard" calibrations that could be applied to all the tests. The calibration curves used are presented in Figure 2.4.3, along with an example of some calibration data. As part of an effort to improve

camera calibration and reduce uncertainty, the author's colleagues performed many experiments resulting in another standard calibration. This calibration was applied to the *p/d* = 11.6 data, which was gathered later. Note that the minimum temperature used in the calibration was several degrees warmer than the minimum temperature recorded on the camera. However, given the near linearity of the camera response, any error due to extrapolation should be small. Also, the regions colder than the minimum calibration temperature are small and within the cooling holes, where laterally averaged data are not usually compared.

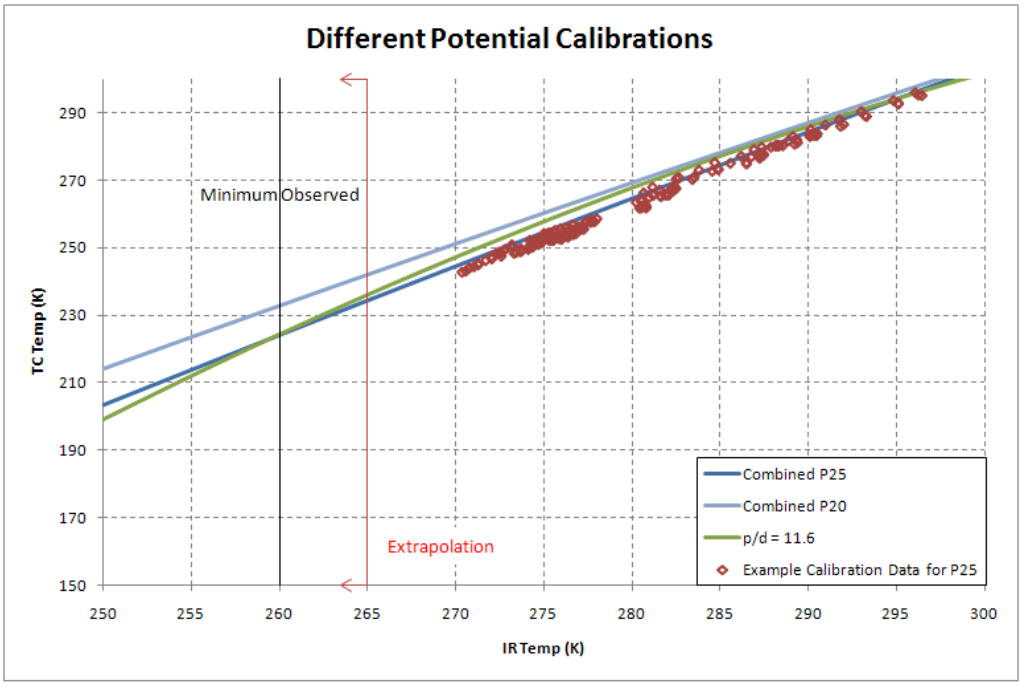

Figure 2.4.3: IR calibrations used for the experiments done for this study

Once satisfied with the calibration, the *x/d* correlation function was created. The *x/d* correlation function used a 3rd order curve fit. A higher order curve fit was not found to give any additional accuracy.

Pasting the results of “blockscan” and “temp2phi” into the template was the next step. The data points still had to be entered so that the conditions of each data point were known, but the creation of plots verifying steady state was automatic.

Reduction of heat flux data were more complicated. The signal from the heat flux gauges contained large fluctuations, from both the heat flux and noise introduced by the environment and signal acquisition. An average of 1000 data points over one second still retained significant low frequency noise. To further reduce the uncertainty in the mean to even lower levels, ~30 separate measurements of the flux were taken. The averaging time for LabView data points could not be increased without making the wind tunnel much more difficult to control. The resulting average voltage signal had an uncertainty in the mean typically less than 1%. Next, the gauge temperature was used to create an adjustment to the voltage. As previously mentioned, the gauge sensitivity was dependant on temperature due to changing properties at different temperatures. Typical values of C_{Tg} encountered during the course of testing were near 1.06, and small changes in temperature did not produce large changes in the adjustment factor. Armed with this adjusted voltage, the calibration constant

could be applied and a heat flux calculated. As previously mentioned, the manufacturer's calibration was found to offer consistent results for most gauges.

Incident radiation also affected the heat flux measurement. In order to get the true q_f'' the radiation component needed to be accounted for. For internal heat flux measurements, it was difficult to determine the actual radiation. An approximation was made by taking the temperature difference to be that of a point on the surface and that of the impingement plate, which was assumed to be very near the temperature of the coolant. Additionally, the paint used to secure the gauges has a low emissivity, estimated to be in the 0.5 range. Even at the largest temperature differences observed, the estimated flux was less than 4% of the measured flux. For the majority of conditions, it was nearer to 0.5%. Since the real radiation adjustment will be less than this worst-case estimate, no radiation correction for internal flux measurements was necessary.

On the exterior, estimation of the radiation contribution was more straightforward. For the h_0 case, the model was very close to a cylinder in cross-flow. Taking h_0 from correlations, an estimate of the heat flux was produced based on the measured temperature differences. Given that the surface was painted with black paint with an emissivity near 0.96, the radiation contribution was also estimated assuming that each point was exposed to an environment the same temperature as the mainstream air. The surface temperature difference was varied from ΔT = 14 to 26 K. Over this range, radiation contributed a nearly constant 6% to the total heat flux. The surface of a film cooled model provides a

higher temperature difference and a different ratio of heat transfer due to convection and radiation. Had the heat flux measurements been more reliable, the radiation flux could have been corrected for, but only a ratio of two fluxes (which include radiation) could be measured. Therefore, the radiation component to the heat transfer coefficient ratio was assumed to be nearly the same percentage as that without film cooling, which would cause the radiation contribution to cancel out. This is a significant assumption, but the difference due to the radiation was certainly less than the already high uncertainty in these measurements due to other factors.

2.5 Uncertainty Analysis

Proper understanding of the level of uncertainty in measurements is crucial before assigning any sort of value to experimental results. The measurement of pressure, temperature, and position combine in different ways to produce uncertainty in each result. Whenever possible, statistical means were used. For all other results, Moffat's [26] method of sequential perturbation was used.

Pichon [10] calibrated each pressure transducer to ±1.875 Pa and ±0.5625 Pa for the coolant and mainstream respectively, resulting in an uncertainty in the mainstream velocity of ±0.03 m/s; much less than the change in velocity across the span of the tunnel. Sequential perturbation showed that δM = ±0.020 for a nominal value of M = 0.5 (4%) and ±0.008 (less than 1%) or better

for all other values of *M*. The analysis included the temperature measurements used to calculate *DR*, which had a resulting uncertainty of δDR = ±0.004. Uncertainty in α was considered to be ±0.4° due to difficulty in positioning the model at α = 0°.

Many factors added to the uncertainty of ϕ. The definition (Eq. 1.2.9) is just four temperature measurements. However, many more factors are known to affect the surface temperature distribution. It is difficult to formulate an equation taking into account all the known quantities that affect ϕ. Additionally, there could be test parameters affecting the overall effectiveness that are unknown. So, even though T_∞ and T_c were measured accurately using thermocouples, and T_w's measurement uncertainty could have been estimated using the IR camera calibration, a statistical analysis was performed on the variation of ϕ from multiple measurements and from multiple experiments to determine the actual uncertainty.

Bias uncertainty was also a concern, and more difficult to eliminate. One potential source of bias was the uncertainty for the conductivity of the model, which could affect comparisons between Corian and Polycast models. Dobrowolski's [23] computational analysis found that increasing the conductivity from 1.04 to 4.3 W/mK increased the overall effectiveness about 25%. If this response can be assumed to be nearly linear, the 6% uncertainty in *k* for the solid would cause much less than 1% change in overall effectiveness. Measurement bias due to entering the wrong number of holes into LabView for

calculating *M* was possible. While considered unlikely, this sort of error was hard to account for since the constants were not saved. Radiation bias could also affect the surface temperature. In an engine, the first stage blade's surrounding environment is not the same temperature as the mainstream flow, as that would imply that the upstream vanes were uncooled. The contribution to heat flux from radiation would then be less than the ~6% that was present for these tests, but the actual amount would be difficult to assess. Lastly, the previously mentioned potential bias due to convection with the metallic impingement plate was assessed as negligible. Details of this determination are present in Section A.2.

A body of data containing many experiments performed by the author and his colleagues was analyzed to find valid comparisons for a statistical analysis for prediction of random error in ϕ. In all, 11 different geometries with one or more test-to-test repetitions were used as the basis for the statistical analysis. The data were corrected for *x/d* bias using the known location of surface features and compared at two positions, *x/d* = 0 and *x/d* = 8.

For each geometry group, the mean and variance were calculated. Then, using the average of all variance values, a true standard deviation for all tests was calculated. Applying Student's *t* distribution with a confidence level of 95% finally produced an uncertainty of $\delta\bar{\phi}$ = ±0.019 for *x/d* = 0 and $\delta\bar{\phi}$ = ±0.014 for *x/d* = 8 under conditions of *M* = 2.0 and *DR* = 1.5. A similar analysis could have been done for other values of *M*, but many fewer comparison points were available, forcing the uncertainty to be much higher. However, there was no reason to

believe that the uncertainty in $\bar{\phi}$ was actually greater. An important assumption is that this uncertainty was also representative of the "local" values represented by ϕ_{min}.

The exception was for *M* = 0.5. As is clear from the adiabatic contour plots shown in Figure 2.5.1, even two points at nominally the same value of *M* show an extreme difference in flow on the stagnation line. This sensitivity to blowing ratio was due to the coolant feed pressure being close to the stagnation pressure, which is discussed in more detail in Section 3.1.1. The sensitivity was seen in adiabatic and overall effectiveness. With no coolant emerging from the stagnation line, there would also be no through-hole cooling. For this blowing ratio, the uncertainty could be as high as $\delta\bar{\phi}$ = 0.04 around the stagnation row, but only a very limited number of points were available for comparison. Downstream of the off-stagnation row the impact should be reduced, but uncertainty should still be considered higher than $\delta\bar{\phi}$ = 0.019.

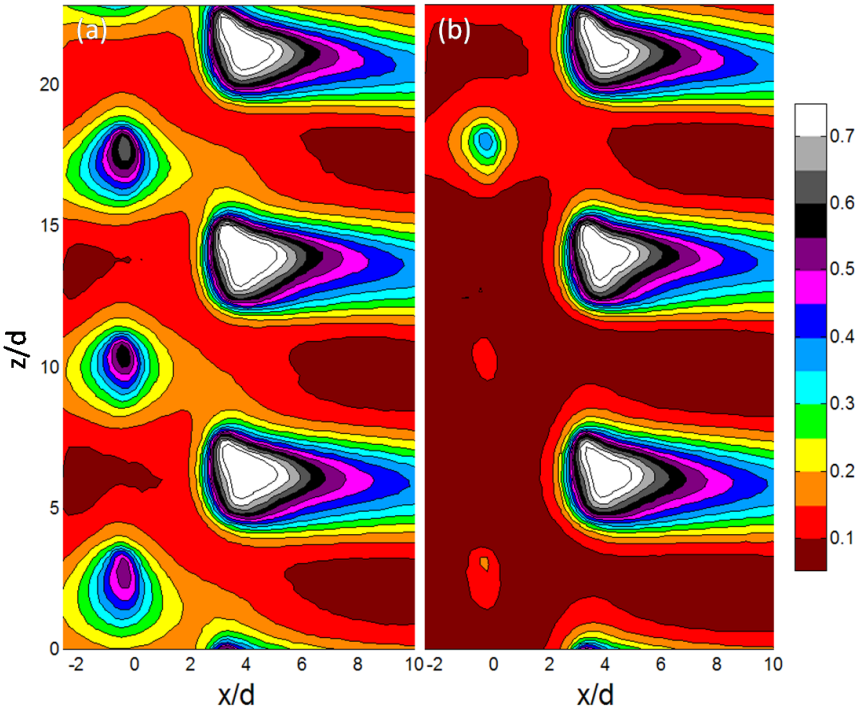

Figure 2.5.1: Comparison of two contour plots of η for *M* = 0.48 and *DR* within 0.01. In the first case (a) there is a small amount of coolant flowing from the leading edge holes, in the second (b) no coolant is visible.

Another important result of this analysis was the comparison of test-to-test and in-test repeatability. Previously it had been assumed that test-to-test variation was greater than in-test variation. However, statistical analysis of both sets of data revealed that in-test and test-to-test repetition of the same data point produced nearly identical uncertainty ($\delta\bar{\phi}$ = 0.019 at *x/d* = 0).

This allowed points from disparate tests to be combined into one analysis through simply averaging all available points. For *M* = 2.0, often used as a baseline and an in-test repeatability point, this made many more points available for computing an average, greatly reducing uncertainty calculated in this manner.

The remaining conditions still had too few points to make this a meaningful comparison, but for all pitches there was enough data to perform this more conventional analysis under this specific blowing ratio. When corrected for *x/d* shifting, the uncertainty for this condition was reduced to $\delta\bar{\phi}$ = ±0.01 for all pitches. This analysis also found that the uncertainty in *x/d* averaged ±0.1 within the range -2 ≤ *x/d* ≤ 12. Since *x/d* is not dependant on flow conditions, this uncertainty in *x/d* applies to all the data, not just *M* = 2.

Unfortunately, there was insufficient data to perform a similar statistical analysis on the adiabatic effectiveness data. Comparison of the maximum separation between the two available tests at *x/d* = 0 showed a difference in η of ~0.02. Comparison of in-test points showed less separation (less than 0.01), which gives some indication that the uncertainty in $\bar{\eta}$ may be less. Albert [14] was able to use a much larger dataset to obtain an uncertainty from a similar test procedure of $\delta\bar{\eta}$ = ±0.03. Given that he also found that uncertainty in adiabatic effectiveness and overall effectiveness were equivalent, it is likely then that the uncertainty for these measurements behaved the same. For this reason, the assumption has been made that $\delta\bar{\eta}$ = ±0.02 (except for *M* = 0.5). There is also the additional bias in the results introduced by conduction error. Using Dobrowolski's [23] computational results, this bias was estimated to be as high as 0.05 very near the holes (within ~ 0.5*d*), but rapidly reduced to 0.01 or less. For *x/d* > 2 it had virtually disappeared. Since the estimated conduction bias was so small and localized it was assumed that the contributions to $\bar{\eta}$ were negligible.

The uncertainty of internal effectiveness, taken purely with thermocouples, was found to be a nearly constant $\delta\phi_i$ = ±0.007 for all conditions using a perturbation analysis and the manufacturer specified uncertainty of thermocouple measurements of ±0.5 °C. Given the high levels of internal effectiveness measured, this represents a negligible value. However, there existed the possibility of additional uncertainty due to the attachment procedure. In order to check that this was not a significant factor, a comparison was made between different attachments at the same nominal position, which is shown in Figure 2.5.2

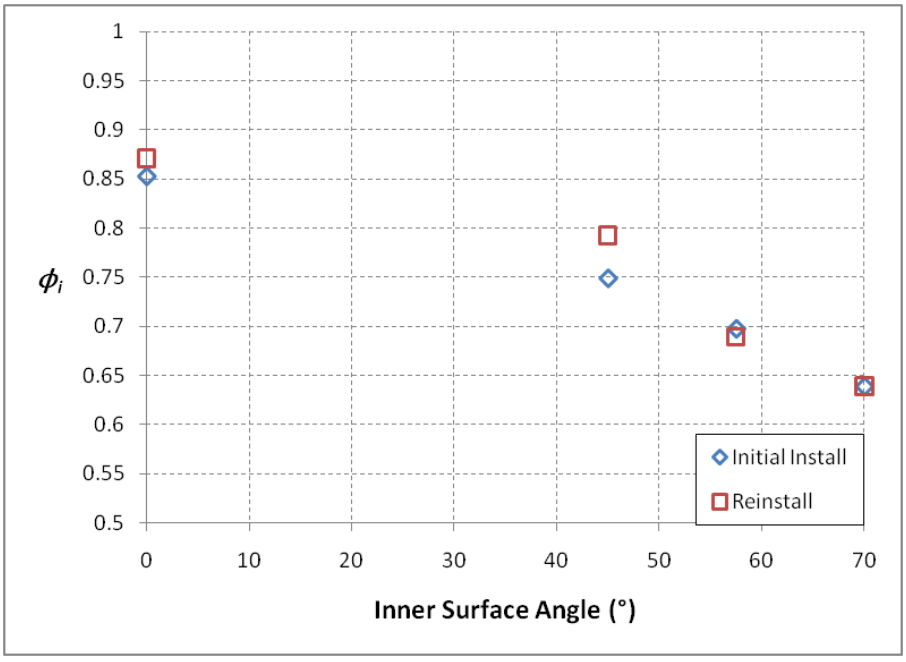

Figure 2.5.2: Comparison of ϕ_i measurements taken after reinstalling thermocouples in the same location

Initially, the fact that there was any separation between the measured points might seem to indicate that the gauges were being affected by attachment uncertainty. However, to truly compare these points some measure of the positional uncertainty in the gauge placement must be made. Measurements made of desired position versus actual position on many gauges determined that placement uncertainty was approximately ±1 mm, which is equivalent to ±0.3 *z/d* or ±4.5° of arc on the inner surface. Strong gradients in surface temperature could cause large differences between measurements, so temperature profiles predicted by Ravelli *et al.* [21] were consulted. They suggested that *z/d* positioning will not affect the temperature reading significantly, anywhere on the interior surface. Their predictions also indicated that for the 0° position, the angular coordinate did not offer a significant contribution to temperature uncertainty. However, at the 45° position, an estimate showed that position might cause a reported $\Delta\phi_i$ as high as 0.02. This easily accounts for the differences observed between gauges, indicating that any additional uncertainty due to the attachment procedure was small.

The production of h/h_0 measurements was complicated by the fact that the measurement would only work if the calibration could be assumed to be constant. This assumption is supported by the data like that presented in Figure 2.5.3. In this figure, the calibration for a given gauge using the thermal grease method is compared to a different method of attachment that did not ensure good thermal contact. The data show that even though the calibration constant was

less than half of the measured value, it was still linear. It is important to note that this assumption cannot be verified using any of the test data taken using silver paint. Gauge degradation was a serious problem that ultimately disabled half the gauges (5/10, the remaining 2 which had to be discarded were mechanically damaged). It cannot be completely ruled out that prior to complete, obvious failure the gauges' calibration ceased to be a linear function of heat flux. The data from the remaining gauges was only kept after careful examination, and verification that the measurements were repeatable. It is also important to note that this degradation likely occurred after the internal heat flux measurements were completed, since those tests had gauge-to-gauge repeatability and produced reasonable heat flux levels.

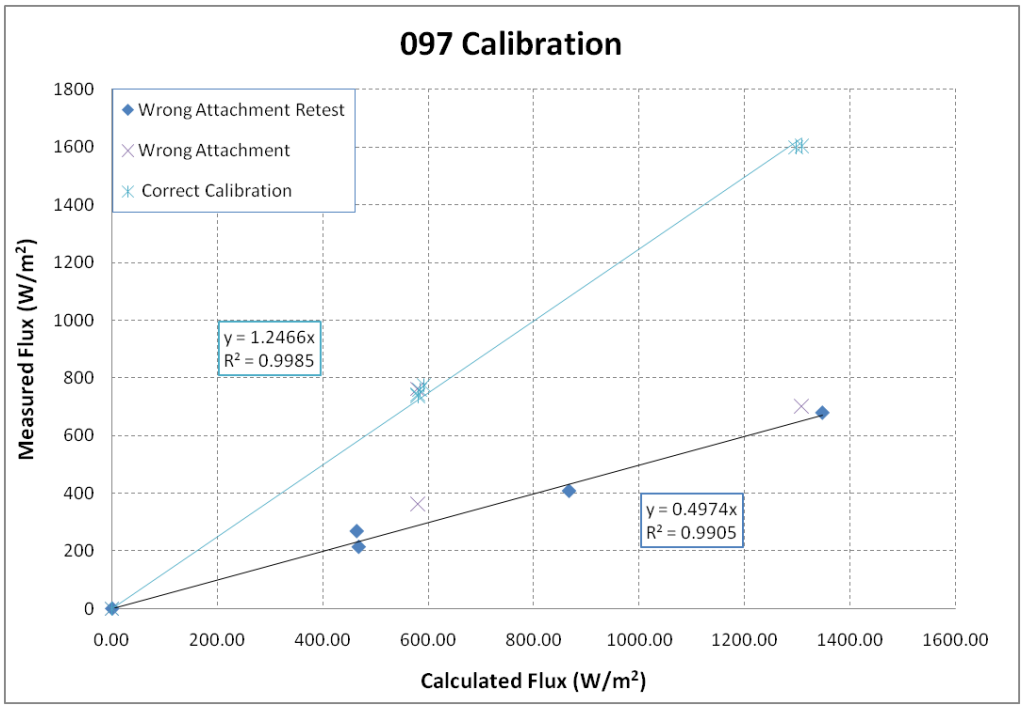

Figure 2.5.3: Heat flux calculated using the manufacturer's specification compared to a known heat flux using the thermal grease method and another method

With that understanding, the uncertainty in the measurements still had to be estimated. The heat transfer coefficient data were generated by taking the ratio:

$$\frac{h}{h_0} = \frac{q''(T_{w,0a} - T_\infty)}{q''_{0a}(T_{w,f} - T_\infty)} \tag{2.5.1}$$

Recall that the heat flux in the denominator is not the same as the heat flux without film cooling, q''_0. However, the heat transfer coefficient is insensitive to flux. Combining Equation 2.3.2 with Equation 2.5.1, a perturbation analysis

estimated the uncertainty. Because so few points were considered usable, each point's uncertainty was calculated individually. These values are presented in Table 2.5.1, along with the corresponding uncertainty in the calculated heat flux ratio. A significant contributor to the uncertainty was the gauge temperature, which was used as the wall temperature in Equation 2.5.1. This temperature was taken from a "clean equivalent" point. That is, the temperature of the gauge was assumed to be the same as a surface point in the same location with no gauge placed upon it. This was necessary since not all of the gauges were visible in the IR viewing area. Since the IR camera was being used to determine the surface temperature, $\delta\bar{\phi}$ was used as the gauge temperature uncertainty. Any additional uncertainty from gauge positioning was small in comparison. The result shows that uncertainty was typically about 10% for the values of h/h_0. Combining this result with the known uncertainties of $\bar{\phi}$ and $\bar{\phi}_0$ gives a typical uncertainty for q_f''/q_0'' of well over 30%, which was mostly due to the high percentage uncertainty in ϕ_0. Under some conditions, uncertainty due to ϕ_0 alone was over 50%. There was also some additional uncertainty from the assumption that the contribution to the flux from radiation was a constant percentage, regardless of surface conditions. However, this was likely to be small, and since the uncertainty from other sources was so large, this additional contribution was neglected.

Table 2.5.1: Uncertainty values for external heat flux measurements in absolute terms and as a percentage of the measurement for the given condition

M	Position	$\delta\left(h/h_0\right)$		$\delta\left(q''_f/q''_0\right)$	
		Abs.	%	Abs.	%
0.5	*x/d* = 4.9 *z/d* = 8.7	0.1	11	0.34	57
	x/d = 4.9 *z/d* = 10	0.12	11	0.36	57
	x/d = 1.8 *z/d* = 6.2	0.086	10	0.35	52
1.0	*x/d* = 4.9 *z/d* = 8.7	0.074	9	0.29	38
	x/d = 4.9 *z/d* = 10	0.077	9	0.28	41
	x/d = 1.8 *z/d* = 6.2	0.058	9	0.22	68
1.5	*x/d* = 4.9 *z/d* = 8.7	0.076	9	0.24	38
	x/d = 4.9 *z/d* = 10	0.083	9	0.26	34
	x/d = 1.8 *z/d* = 6.2	0.057	9	0.17	180
2.0	*x/d* = 4.9 *z/d* = 8.7	0.063	8	0.19	44
	x/d = 4.9 *z/d* = 10	0.066	8	0.20	40
	x/d = 1.8 *z/d* = 6.2	0.065	9	0.18	58

Uncertainty for direct heat flux measurements taken on the inner wall of the model was strongly dependent on the uncertainty in calibration constant. The manufacturer's specification was used, but no uncertainty was provided. As an estimate, the differences between the factory calibration constants and those measured using the testing process described in Section 2.3 were analyzed

statistically. Combining this uncertainty with other measurement uncertainties (including the uncertainty in gauge temperature due to placement) using a perturbation analysis showed that all q_i'' measurements had a nearly constant uncertainty of 16%. The resulting values of h_i were also dependant on the uncertainty in the temperature sensor placement. For the 0° position, the additional uncertainty only increased the typical uncertainty to 18%. However, at the 45° position there was a stronger temperature gradient, so the uncertainty was increased to about 24%. These values also apply to reported Nusselt numbers, as uncertainties in the dimensional factors used to non-dimensionalize were considered very small.

Internal jet velocity was calculated from *M*, *U*, *DR* and known geometry. A perturbation analysis showed that the uncertainty in Re_j was as high as 4% for *M* = 0.5, but the remaining blowing ratios had a value of approximately 0.5%.

3 Results and Discussion

The primary goal of this study was to examine the effects of pitch variation on cooling performance on the leading edge of a simulated turbine blade. In pursuit of this goal, pitch values of *p/d* = 7.6, 8.6, 9.6 and 11.6 were examined using matched Biot number models at blowing ratios of 1.0, 1.5, 2.0, 2.5 and 3.0. blowing ratio of *M* = 0.5 was also evaluated at *p/d* = 7.6 and 8.6. Angles of attack of 0°, ±0.6°, ±1.5°, ±4.6° and ±7.7°[1] were evaluated, which represents the approximate deflection of the stagnation line from an unsteady wake. Results were compared not only in terms of $\bar{\phi}$, but also using the new lateral minimum overall effectiveness parameter, ϕ_{min}. This parameter is arguably more important than the lateral average in determination of cooling performance. Internal temperature distributions were also collected for *p/d* = 7.6, 8.6 and 9.6.

Additionally, an adiabatic test was undertaken for *p/d* = 7.6 to gain an increased understanding of the coolant distribution. These experiments evaluated the same blowing ratios and angles of attack as those of the overall effectiveness tests.

Lastly, the direct measurement of heat flux was also performed at *p/d* = 7.6 on both the internal and external surfaces. For the internal heat flux, the data are compared to similar cases from the impingement cooling literature and the

[1] These angles are equivalent to angles of ±0.4°, ±1.0°, ±3.0° and ±5.0° reported in previous angle of attack studies using the TTCRL facility ([18], [22],[15], and [31]). Though α was calculated improperly, the data were gathered consistently.

computational study of Ravelli *et al*. which exactly duplicated the geometry used for these tests. External heat flux results were converted to a net heat flux reduction using data from Dobrowolski [23] in order to compare to past experiments which made use of η and h_f/h_0 to predict NHFR.

All tests had a common Tu = 5% and Re = 50,000 to properly represent the conditions experienced by a first stage blade. All tests were also performed at a common DR of 1.5. Engine conditions are usually closer to 2.0, but as discussed in Section 1.2 the differences should be small and this facility was limited to lower density ratios. A summary of all the experiments undertaken for this study and the data available from each test is presented in Table 3.1.

Table 3.1: All experiments performed during the course of this study. Xs indicate available data with adjacent numbers indicating repeat points.

Geometry	M						α								Other
	0.5	1.0	1.5	2.0	2.5	3.0	-7.7	-4.6	-1.5	-0.6	0.6	1.5	4.6	7.7	
p/d = 7.6	X	X	X	X3	X	X	X	X	X	X	X	X	X	X	Internal Temp
	X	X		X2											Heat Flux
	X	X	X	X2	X	X									Heat Flux
p/d = 7.6, no impingement	X	X		X2		X									Heat Flux
	X	X		X2		X									Heat Flux
p/d = 7.6 plastic impingement	X	X	X	X2	X	X									Heat Flux
p/d = 8.6	X	X	X	X3	X		X	X	X	X	X	X	X	X	Internal Temp
	X	X	X		X	X									Internal Temp
p/d = 8.6, Corian		X	X	X4	X	X			X			X			more calibration data
		X	X	X4	X	X	X	X	X	X	X	X	X	X	
p/d = 9.6		X	X	X4	X	X	X	X	X	X	X	X	X	X	Internal Temp
p/d = 7.6, Adiabatic	X2	X	X2	X	X	X									
				X3			X	X	X	X	X	X	X	X	α = ±0.9
p/d = 11.6		X	X	X	X	X	X	X	X	X	X	X	X	X	

3.1 Adiabatic Effectiveness Results

Before examining the results of the overall effectiveness tests it is useful to examine the behavior of the coolant on the surface. Knowing how the coolant is behaving on the surface can provide important insight when examining the surface temperature distribution. Results are presented as both lateral average values and contour plots.

3.1.1 Effects of Blowing Ratio Variation

The effect of increasing blowing ratio is most succinctly summarized by observation of $\bar{\eta}$ values shown in Figure 3.1.1. Adiabatic effectiveness was quite low under the stagnation row for M = 0.5, Increasing the blowing ratio to M = 1 dramatically improved η in the region. Subsequent increases in M showed some improvement up to M = 2, where performance levels off within $0 < x/d < 3.5$. Downstream of the off-stagnation row results were largely within the uncertainty of $\delta\bar{\eta} = \pm 0.02$ except for $4 < x/d < 6$ when considering the difference between the maximum and minimum blowing ratios, which exhibited $\Delta\bar{\eta} = 0.05$. It is safe to say that $\bar{\eta}$ was decreasing with increasing blowing ratio in this region. The normal expectation might be that any increase in coolant would necessarily improve effectiveness. This is not always the case, because an increased coolant jet velocity can cause the jet to separate from the surface. Therefore the surface is less protected, and coolant is being wasted. The trend of decreasing $\bar{\eta}$ indicates that there was some jet separation from the off-stagnation holes at higher

blowing ratios. As *x/d* is further increased, the difference between blowing ratios reduced to negligible levels.

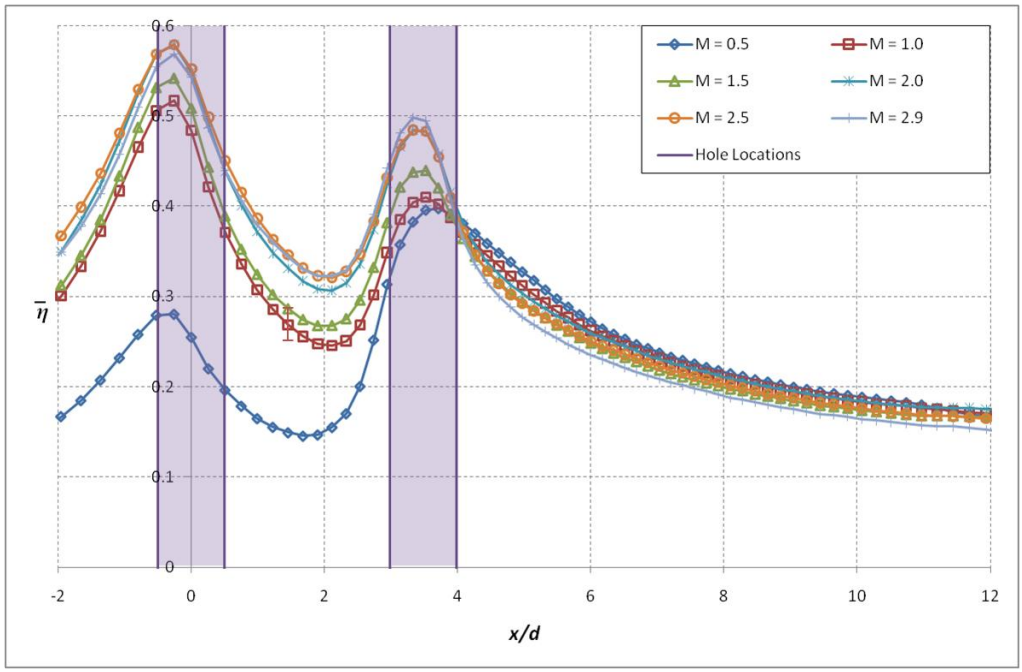

Figure 3.1.1: Comparison of $\overline{\eta}$ under changing *M* for *p/d* = 7.6 and α = 0°

The extreme difference between the lowest blowing ratio and the remaining cases bears further discussion. The very low coolant flow rate was likely because the internal coolant pressure was constant but the external pressure distribution peaks over the stagnation row of holes. The result was that at lower coolant flow rates there was a difference in local blowing ratio, *M**, between the stagnation row of holes and the off-stagnation rows. On the stagnation row, *M** was necessarily lower than the overall blowing ratio. Most of the time this difference was very small, but at very low blowing ratio the internal

feed pressure was very close to the stagnation pressure, resulting in greater sensitivity. The flow rate out of any given hole can be estimated from,

$$\dot{m}_c = \frac{\pi}{4} d^2 C_d p_c \left(\frac{p_\infty}{p_c}\right)^{\frac{\gamma+1}{2\gamma}} \sqrt{\frac{2\gamma}{(\gamma-1)RT_c}\left(\left(\frac{p_c}{p_\infty}\right)^{\frac{\gamma-1}{\gamma}} - 1\right)} \qquad (3.1.1)$$

The external pressure distribution, p_∞, was computationally predicted by Kohli [27]. The discharge coefficient, C_d, was assumed to be 0.7 and constant for all three rows. Though it was recognized that discharge coefficient varies with flow rate and many geometric factors, this value was chosen as typical for an inclined round hole [28]. The results of this analysis are presented in Table 3.1.1. Of particular importance is the low value of M^* on the stagnation row when M = 0.5, resulting in high uncertainty. Since the true value of C_d was unknown, these ratios are only an estimate, but they support the idea that overall blowing ratio is a good representation of the blowing ratio except at very low coolant flow rates.

Table 3.1.1: *M for the stagnation and off-stagnation rows of holes for a given *M***

Overall *M*	Stagnation *M**	Off-stagnation *M**
0.5	0.35	0.58
1.0	0.93	1.04
1.5	1.45	1.52
2.0	1.96	2.02
3.0	2.98	3.01

Even more information can be extracted through examination of the contour plots. Figures 3.1.2 and 3.1.3 show the contours for all blowing ratios. Along the stagnation, line there is strong evidence for jet separation for $M \geq 1.5$. Regions of high η between the coolant holes (the coldest visible feature) are strong indications that a detached jet has reattached to the surface. As blowing ratio was further increased, this reattachment moves further downstream and was no longer visible for $M = 2.9$. It was thought that the coolant jets along the stagnation line merge together into a continuous stream, which may become more and more separated from the surface, causing $\bar{\eta}$ to remain level with increasing blowing ratio. For the off-stagnation row of holes, evidence of separation can be observed as a decreasing area of high η immediately downstream of the holes, which suggests that the coolant jet was further from the surface. This is likely the reason that this region saw a decrease in η with increasing blowing ratio.

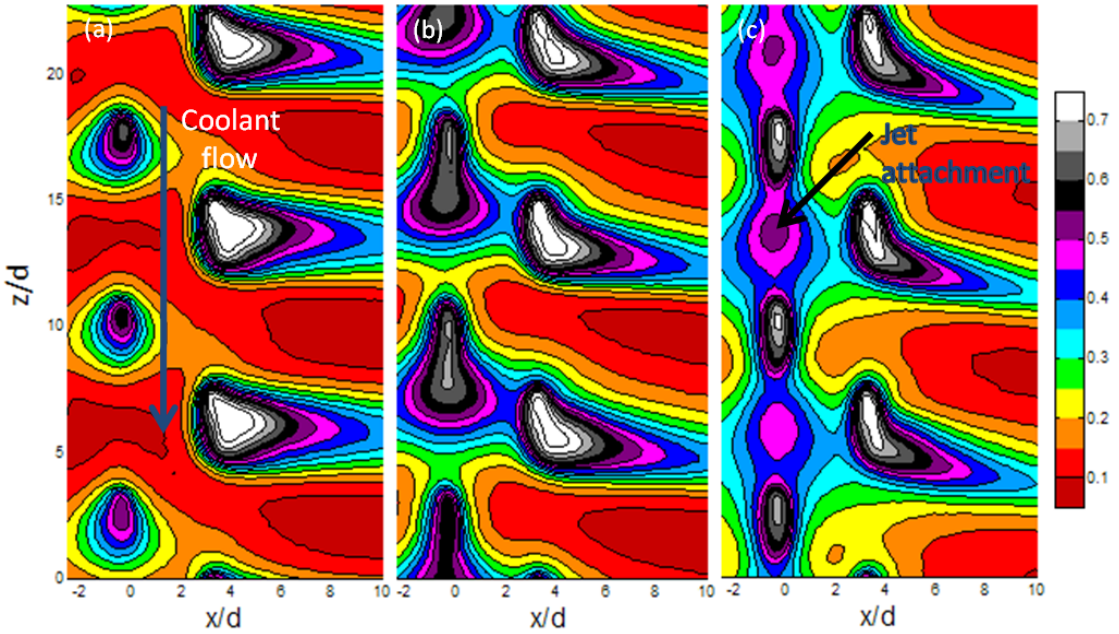

Figure 3.1.2: Contours of η for *p/d* = 7.6, and (a) *M* = 0.5, (b) 1.0 and (c) 1.5

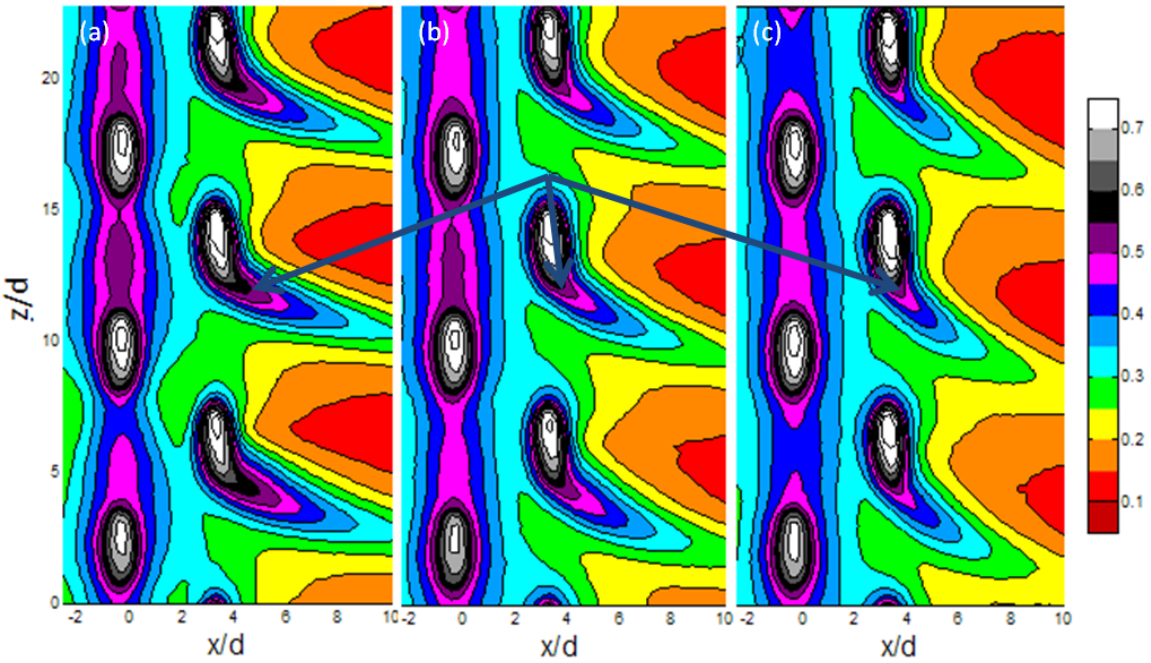

Figure 3.1.3: Contours of η for *p/d* = 7.6 and (a) *M* = 2.0, (b) 2.5 and (c) 2.9

The data are also compared to the works of Johnston [29] and Yuki [30]. Both made use of a model constructed from a quarter cylinder with bypass suction used to produce a stagnation line in the correct location. Yuki's data were taken at *DR* = 1.1 and Johnston's at 1.8, but the effect of *DR* has been shown to be very weak on η [8]. Both results were taken at *Tu* = 0.5%, which, according to the findings of Johnston *et al*. [9], should provide higher adiabatic effectiveness levels than the *Tu* = 5% used in the current study.

Figures 3.1.4 and 3.1.5 compare conditions of *M* = 1 and *M* = 2, respectively. It is interesting to note that even though both Johnston and Yuki were measuring nominally the same conditions, there is a significant difference between the results in the region between rows of holes. Yuki's data show slightly greater adiabatic effectiveness than that of this study, which is consistent with the change in mainstream turbulence. However, Johnston's data show substantially lower values of $\bar{\eta}$. Downstream of the off-stagnation row of holes, all the data fall more closely together. There is agreement within uncertainty among all the data with the exception of Johnston's *M* = 1 data, which are still enough below other values that they likely represent a lower adiabatic effectiveness.

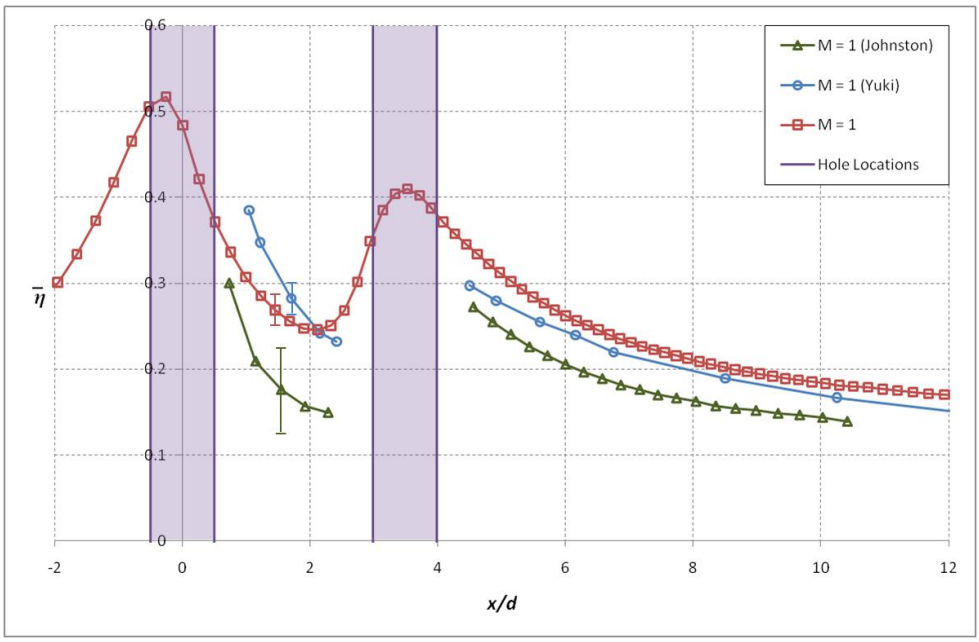

Figure 3.1.4: Comparison to the *Tu* = 0.5% data of Johnston (*DR* = 1.8) and Yuki (*DR* = 1.1) at *M* = 1

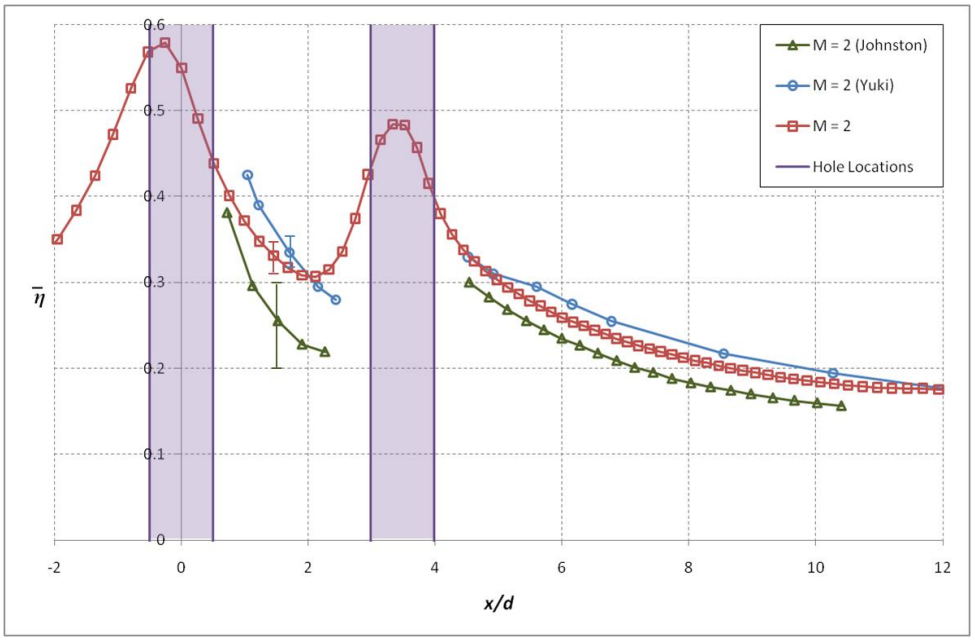

Figure 3.1.5: Comparison to the *Tu* = 0.5% data of Johnston (*DR* = 1.8) and Yuki (*DR* = 1.1) at *M* = 2

3.1.2 Effects of Angle of Attack Variation

As a blade rotates, the airfoil passes through the wake generated by upstream vanes, effectively changing the angle of attack of the approach flow. Johnson *et al*. [31] showed that performance under unsteady wake conditions can be predicted by averaging steady state results at varied angle of attack. For this reason, data were also gathered at angles of 0.6°, 1.5°, 4.6° and 7.7° at both positive and negative orientations. More important to the behavior of cooling performance was the actual position of the stagnation line. Johnson [15] measured the position for each angle of attack, and his results are reproduced in Table 3.1.2. The movement of the stagnation line also changes the local blowing ratios from each row of holes somewhat. Though the streamlines were curved when the model was placed at an angle, an estimate of the local blowing ratio was produced by assuming that the pressure distribution remained the same and the position of the holes changed relative to the stagnation line. The predicted change in local blowing ratio is presented in Table 3.1.3. These data show that there was likely a slight increase in M^* on the positive side relative to the other rows, but even at the maximum angle this was expected to be small.

Table 3.1.2: Position of the stagnation point under changing angle of attack

Angle of Attack (°)	Stagnation Position (*x/d*)
0.6	-0.26
1.5	-0.65
4.6	-1.97
7.7	-3.36

Table 3.1.3: Estimated *M for each α with an overall *M* = 2**

Angle of Attack (°)	Negative Side Row	Center Row	Positive Side Row
0.6	2.01	1.96	2.03
1.5	2.00	1.96	2.04
4.6	1.96	1.97	2.07
7.7	1.92	1.97	2.10

Though the data were not time averaged as Johnson *et al.* did, an examination of the angle of attack variation results should show any point where a significant change in performance between pitches might cause the time averaged performance to alter significantly. Combined $\bar{\eta}$ results from both positive and negative α conditions are presented in Figure 3.1.6. The initial expectation would be that as more coolant was swept to the positive side of the model there would be an increase in performance on that side and a corresponding reduction in adiabatic effectiveness on the negative side. This was true for the smallest change in α, but any further change in angle of attack was detrimental to $\bar{\eta}$ on both sides of the model. The reason for this is made apparent through examination of the contour plots for α = 0°, ±0.6° and ±1.5°, shown in Figures 3.1.7 and 3.1.8. The coolant stream in the stagnation region was visibly disrupted, even at a small angle of attack change of 0.6°.

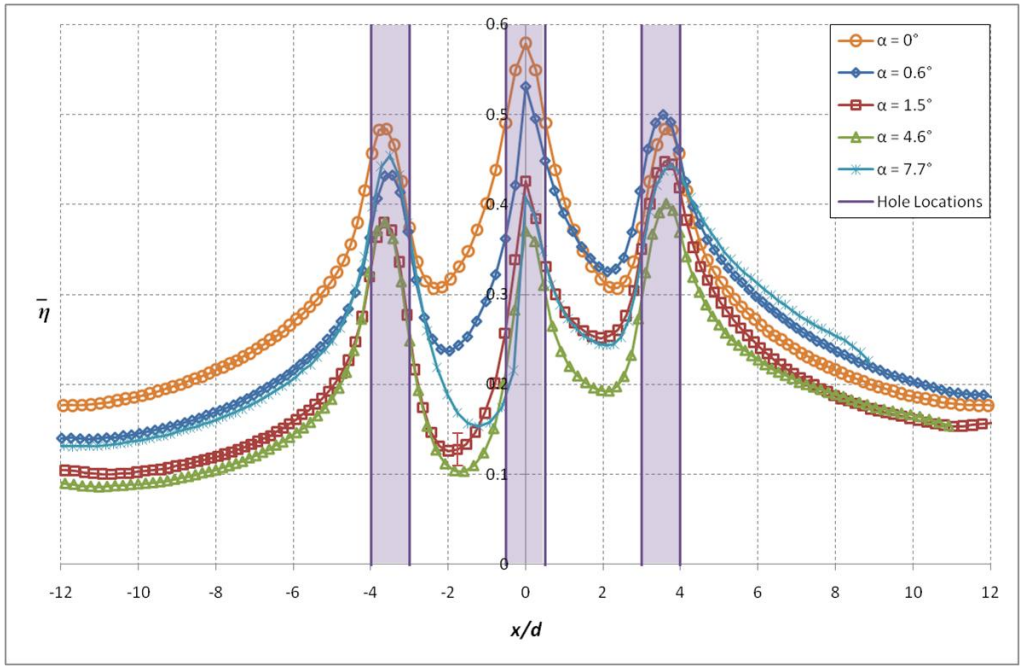

Figure 3.1.6: Comparison of $\overline{\eta}$ under changing α for *p/d* = 7.6 and *M* = 2.0

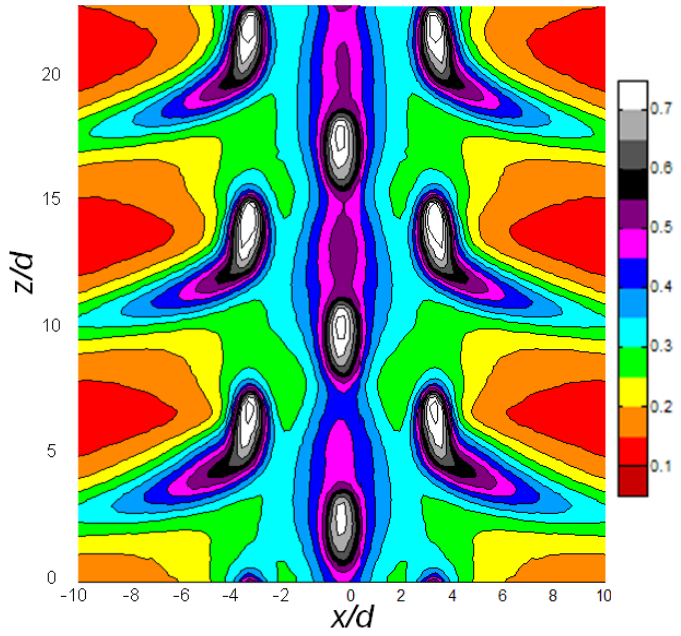

Figure 3.1.7: Contours of η for α = 0° for *p/d* = 7.6 and *M* = 2

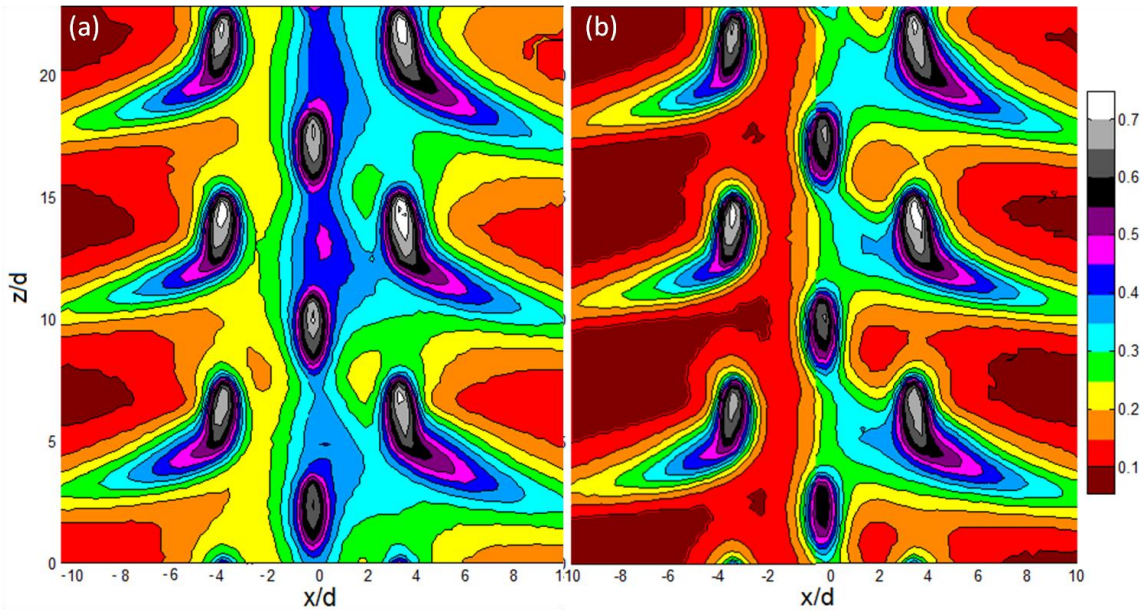

Figure 3.1.8: Contours of η for α = ±0.6° (a) and ±1.5° (b) for *p/d* = 7.6 and *M* = 2

Further increasing the angle to α = ±4.6° served to even further degrade performance, reducing coverage on the positive side to the lowest levels observed. Interestingly, as α was increased to 7.7°, shown in Figure 3.1.9 (b), the adiabatic effectiveness improved relative to smaller changes in α. This was because the position of the stagnation line had moved to be very close to the off-stagnation row of holes on the negative side. As the stagnation region moved to *x/d* = -3.36, part of the row of holes was overlapped by the very low velocity around the stagnation point (measured with a tuft to be approximately one hole diameter across), which produced an effect similar to that seen with the stagnation point over the center row of holes. The local mainstream velocity above the holes at *x/d* = 0 and 3.5 was also increasing. This could lead to better jet attachment, accounting for the improved $\bar{\eta}$ observed on the positive side for this angle. The contour plots strongly suggest that both the *x/d* = 0 and *x/d* = 3.5 rows of holes had improved jet attachment. The α = 7.7° plot also clearly shows the region of poor data produced by interference from the salt crystal window around *x/d* = 9. This was often a problem at high positive angles of attack, so $\bar{\eta}$ and $\bar{\phi}$ plots are cut off here.

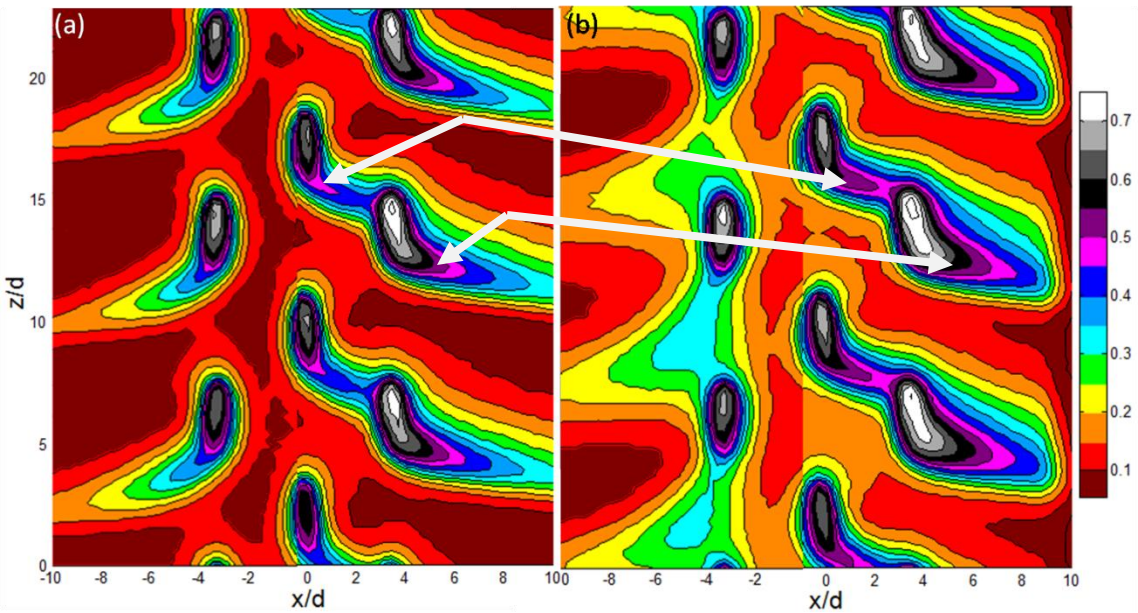

Figure 3.1.9: Contours of η for α = (a) 4.6° and (b) 7.7° for *p/d* = 7.6 and *M* = 2

3.2 Effects of Pitch Variation

Adiabatic effectiveness tests for jets on a flat plate have shown that $\bar{\eta}$ is reduced directly with increasing pitch beyond the jet-to-jet interaction limit. The work of Schmidt *et al*. [19] compared two pitches – *p/d* = 3 and 6 – using 60° compound angle holes on a flat plate. Their reported $\bar{\eta}$ values for *p/d* = 6 were approximately half that of *p/d* = 3, supporting the idea that $\bar{\eta}$ will be inversely proportional to the increase in pitch. Based on this result, one might predict that this trend may apply to other areas. However, the adiabatic effectiveness results already presented indicate that the stagnation row of holes was experiencing jet-to-jet interaction even at *p/d* = 7.6, well outside the range generally considered to interact in flat plate studies. No study could be located that evaluated the effect of pitch in the leading edge region, adiabatic or otherwise.

Coolant distribution is not the only factor governing ϕ. Through-hole convection and internal impingement cooling both affect the external temperature distribution. As the impingement jet spacing on the interior was increased with pitch, the internal cooling was expected to reduce somewhat. However, the heat transfer on the inner surface is driven in large part by strong mixing away from the impingement jets. Bunker and Metzger [32] have shown that average heat transfer coefficients on the inner surface are only weakly tied to impingement jet pitch (a 30% increase in pitch resulted in a ~10% drop), so it was expected that h_i would remain relatively constant. It was also expected that the through-hole heat transfer coefficient would be unaffected.

However, a constant heat transfer coefficient does not mean that heat flux and surface temperature would remain constant. The high *h* encountered in through-hole convection means that even small changes in wall temperature can dramatically change the balance of q_h'' and q_i''. It is difficult to predict the further interaction with external cooling and the resulting overall effectiveness.

To investigate this, overall effectiveness results were obtained for four *p/d* values: 7.6, 8.6, 9.6 and 11.6. For all pitches, *M* of, 1.0, 1.5, 2.0, 2.5 and 3.0 were tested, and *M* = 0.5 was tested for 7.6 and 8.6. Additionally, the angle of attack was varied from -7.7° to +7.7°. All *M* variation tests were done at angle of attack of 0°, and all tests were carried out using *DR* = 1.5 and *Re* = 50,000.

3.2.1 Effects of M *Variation*

Figure 3.2.1 shows $\bar{\phi}$ for *p/d* = 7.6 under varying *M*. There is some similarity to the $\bar{\eta}$ results in that the overall effectiveness started out very low, improved dramatically at *M* = 1.0 and continued to improve somewhat thereafter. However, where $\bar{\eta}$ leveled off around *M* = 2, $\bar{\phi}$ continued to improve up to the maximum blowing of *M* = 3. The overall effectiveness dropped off less between the rows of holes and more slowly downstream of the off-stagnation row than the adiabatic effectiveness. This was not unexpected when considering conduction effects.

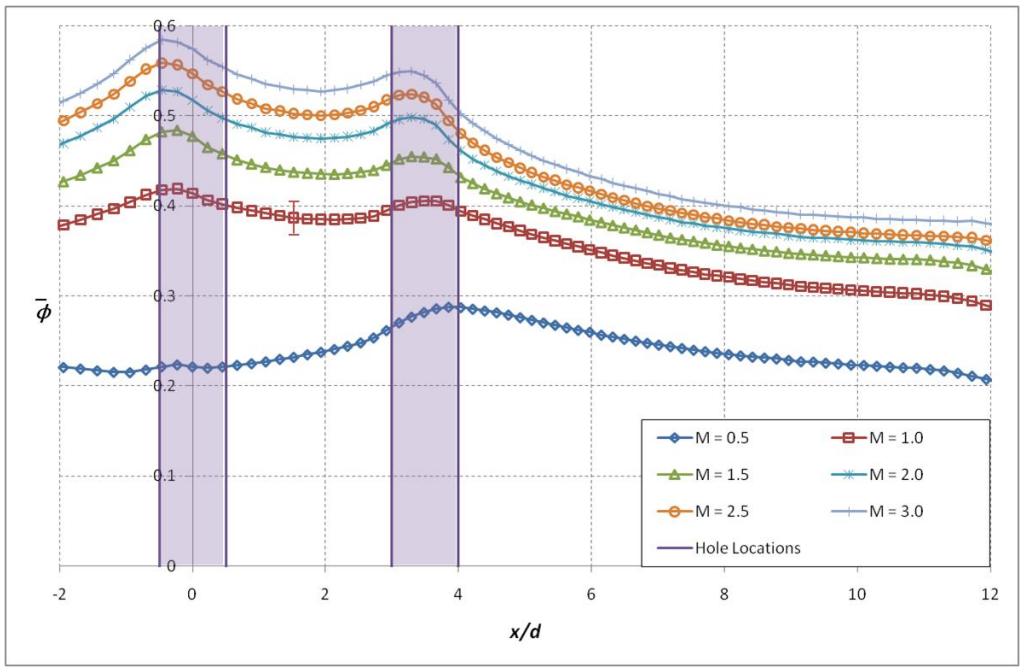

Figure 3.2.1: $\bar{\phi}$ comparison for various blowing ratios with *p/d* = 7.6

These results are mostly consistent with those of Maikell *et al*. [18], who used an identical *p/d* = 7.6 model in their study. However, a direct comparison with their results, shown in Figure 3.2.2, reveals a few differences. For *M* = 0.5, the difference between tests was not surprising given the additional uncertainty that this low blowing ratio suffers. The comparison at *M* = 1 may appear poor, but is still within experimental uncertainty. *M* = 2 agrees very well. Most notable is the large difference between the data collected at *M* = 3. Maikell *et al*. reported that $\bar{\phi}$ ceased to improve for *M* ≥ 2, while these new data show a continued improvement all the way to *M* = 3. There are some relatively involved arguments that could possibly explain this discrepancy. However, the *M* = 3 data from Maikell *et al.* were not repeated, but this point was repeated for the current study. The available repeat point agreed well with that shown in Figure 3.2.1, so it was considered reliable, and representative of the real performance at this level.

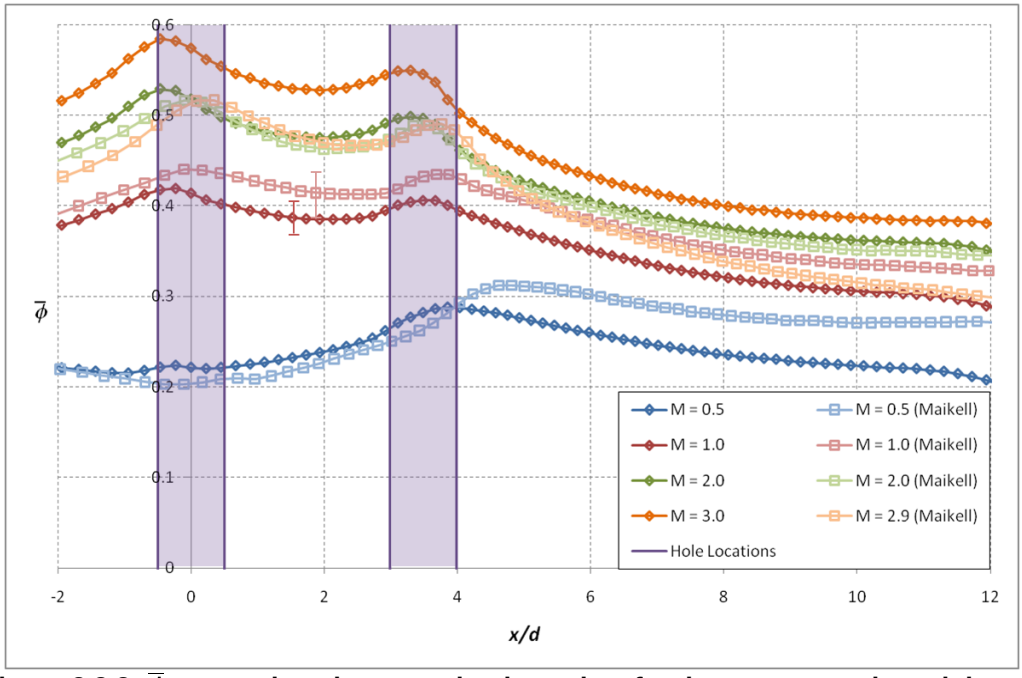

Figure 3.2.2: $\bar{\phi}$ comparison between the data taken for the current study and that of Maikell *et al.* using *p/d* = 7.6

All the $\bar{\phi}$ data show that increasing *p/d* from 7.6 to 9.6 resulted in, at most, a small degradation in overall effectiveness. Further increasing the pitch to *p/d* = 11.6 in all cases showed a significant drop-off in performance. A change in pitch of 26% was shown to change the average overall effectiveness, and consequently surface temperature, by only about 4%. Perhaps more important, the 13% pitch change between *p/d* = 7.6 and 8.6 resulted in no appreciable change in surface temperature. This means there is some point at which decreasing the pitch will no longer improve performance, allowing available coolant to be spent on other parts of the blade, or not used at all, resulting in an efficiency boost to the engine overall. Even a 53% increase to *p/d* = 11.6 only

decreased the overall effectiveness around 15% compared to *p/d* = 7.6. This raises the question of whether this relatively small drop in performance might be corrected with an increase in blowing ratio. This question is evaluated later, in Section 3.4.

For $M \leq 1.5$, the laterally averaged overall effectiveness distributions for *p/d* = 7.6, 8.6 and 9.6 were very similar, always lining up within experimental uncertainty. In the same blowing ratio range, $\bar{\phi}$ for *p/d* = 11.6 value was lower by a $\Delta\bar{\phi}$ as high as 0.1 from the other pitches. An example is shown in Figure 3.2.3.

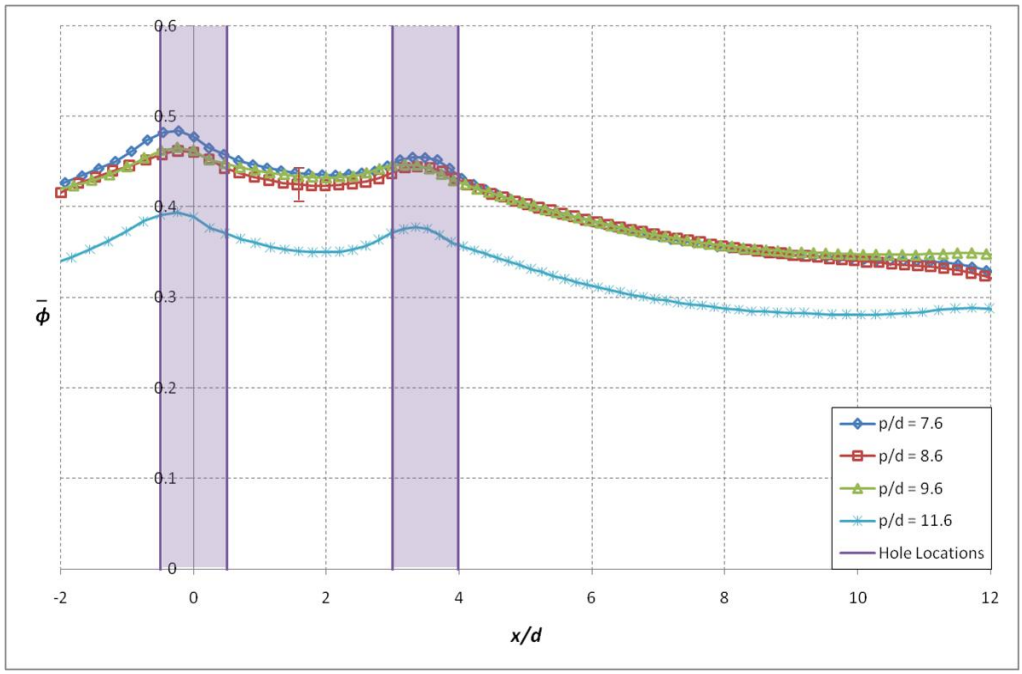

Figure 3.2.3: $\bar{\phi}$ vs. *x/d* for *M* = 1.5

For the *M* = 2 condition, $\Delta\bar{\phi}$ between *p/d* = 7.6 and 9.6 was initially considered to be within experimental uncertainty. However, given the unexpected

nature of the agreement between two pitches representing an increase in area of 26%, additional care was taken for this blowing ratio. Enough data existed to allow $\delta\bar{\phi}$ to be reduced from = ±0.02 to ±0.01 for this condition through averaging multiple tests. When comparing these averaged values, shown in Figure 3.2.4, $\Delta\bar{\phi}$ between *p/d* = 7.6 and 9.6 falls just outside uncertainty with a $\Delta\bar{\phi}$ of just more than 0.02 over the majority of the *x/d* range, while the *p/d* = 8.6 data remained identical in appearance to *p/d* = 7.6. The change in $\bar{\phi}$ between *p/d* = 7.6 and 11.6 was, as with all other tested values of *M*, significantly more than the other *p/d* values. Over the *x/d* range presented, it was nearly uniformly lower with $\Delta\bar{\phi}$ = 0.06 on average.

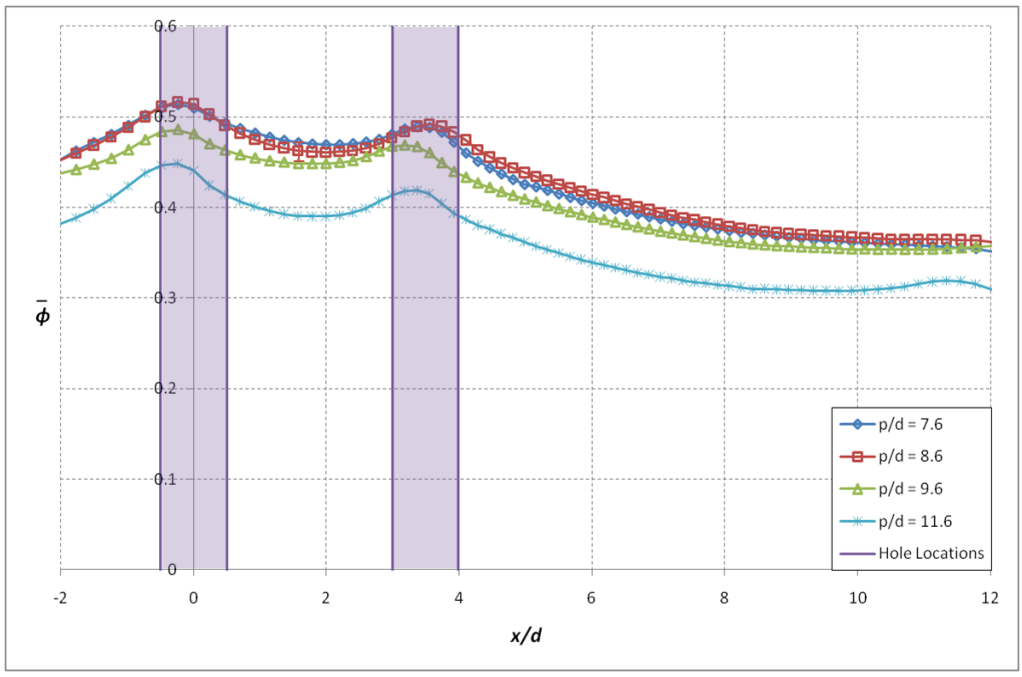

Figure 3.2.4: Average $\bar{\phi}$ values from multiple data points for *M* = 2.0

A look at the contour plots for this data can help elucidate why such a small change might be present. Figure 3.2.5 shows M = 2 for all the pitches. For p/d = 7.6, 8.6 and 9.6 the temperatures in and around the cooling holes appear to be nearly the same. Hot points can be seen forming along the stagnation line, where the adiabatic effectiveness results showed that the coolant was continuous for p/d = 7.6. These potential gaps in coverage continue downstream, and the warmest areas visibly increase in size. However, these comprise a relatively small area in comparison to the entire pitch, so it is not surprising that these three pitches showed very little change on a laterally averaged basis. Finally, p/d = 11.6 shows the result for a more extreme change. The hot points visible at p/d = 9.6 have grown to encompass much of the stagnation line, dramatically increasing the temperature throughout. There is also strong evidence of jet reattachment between the holes, visible as cold spots having nearly the same temperature as the holes themselves. To a lesser extent, the hottest regions on the p/d = 9.6 contour could also be the result of jet separation, though there is also the fact that the holes were closer to the surface in the colder region, so conduction effects certainly played a part.

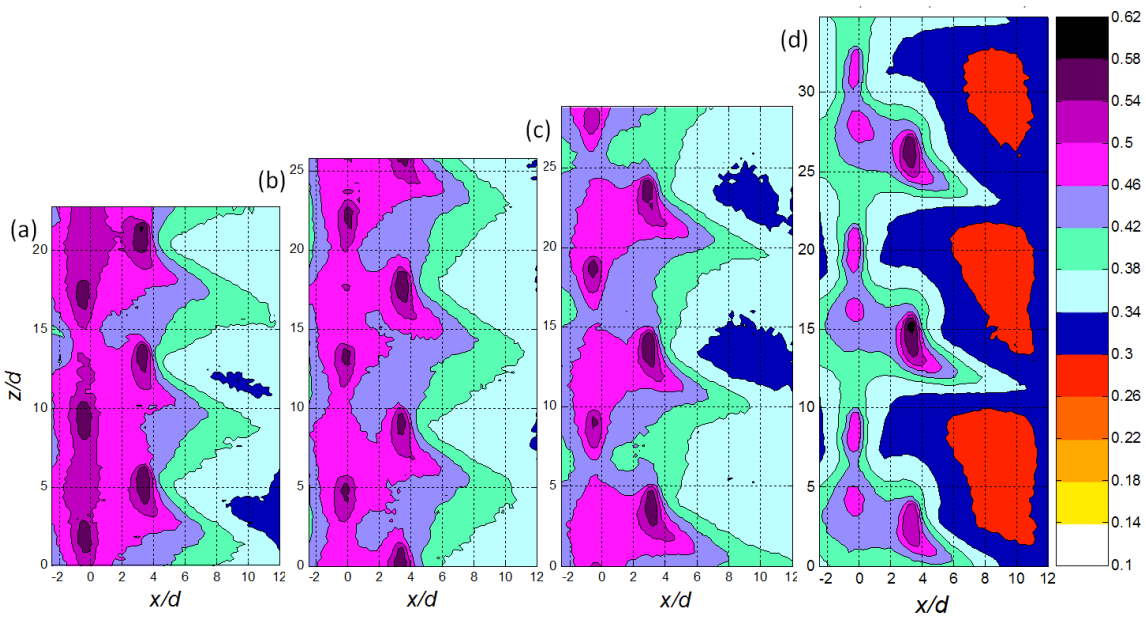

Figure 3.2.5: Contours of ϕ for *M* = 2 and *p/d* = (a) 7.6, (b) 8.6, (c) 9.6 and (d) 11.6

Also notable in Figure 3.2.4 is the behavior as *x/d* increases. It is evident that downstream from the coolant holes $\Delta\bar{\phi}$ between *p/d* = 7.6 and 9.6 reduced until *x/d* = 8, where it was no longer outside of experimental uncertainty. Nearer the leading edge, the effects of through-hole cooling and film cooling are the strongest. At higher *x/d*, the cooling from film cooling (represented by $\bar{\eta}$) has greatly diminished, as shown in Figure 3.2.6. While the exact behavior of $\bar{\eta}$ under increasing pitch is unknown, its contribution to surface temperature for high *x/d* would be small, since even for *p/d* = 7.6, $\bar{\eta}$ = 0.22 at *x/d* = 8. However, internal cooling has not fallen off the same amount. In fact, Dobrowolski [23] showed that with internal cooling only, the temperature remained almost constant ($\bar{\phi}_0$ = 0.22) for the entire *x/d* range. Coupled with the idea that the internal cooling is

relatively constant with increasing pitch, it is not surprising then that the overall effectiveness data converge far downstream of the holes. Even *p/d* = 11.6 displayed some convergence with the other pitches for increasing *x/d*. At *x*/d = 2 and *M* = 2, $\Delta\bar{\phi}$ between *p/d* = 7.6 and 11.6 was approximately 0.08 (16%), while at *x/d* = 10 the difference was reduced to 0.05 (13%).

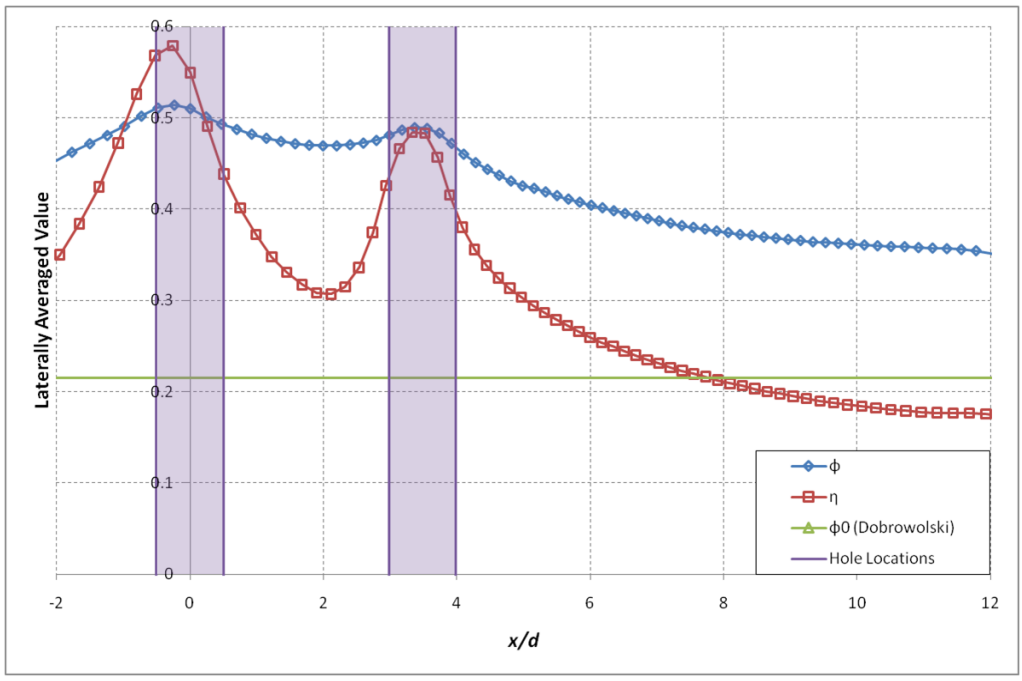

Figure 3.2.6: Comparison of $\bar{\phi}$ and $\bar{\eta}$ for *p/d* = 7.6 and $\bar{\phi}_0$

The highest blowing ratio examined, *M* = 3, also showed notable differences in $\bar{\phi}$ between *p/d* = 9.6 and the shorter two pitches. This blowing ratio is shown in Figure 3.2.7. For much of the *x/d* range, the $\bar{\phi}$ value for *p/d* = 9.6 was about 0.03 below that for *p/d* = 7.6, though right on the stagnation line the

difference exceeded 0.04. While this is nominally within uncertainty for this measurement, it is extremely unlikely that both values would be at opposite extremes. As with all other blowing ratios, the difference between *p/d* = 11.6 and all the shorter pitches was pronounced, exceeding $\Delta\bar{\phi}$ = 0.07 in some locations, with 0.05 being seen even far downstream of the off-stagnation row of holes. The convergence at high *x/d* is also visible.

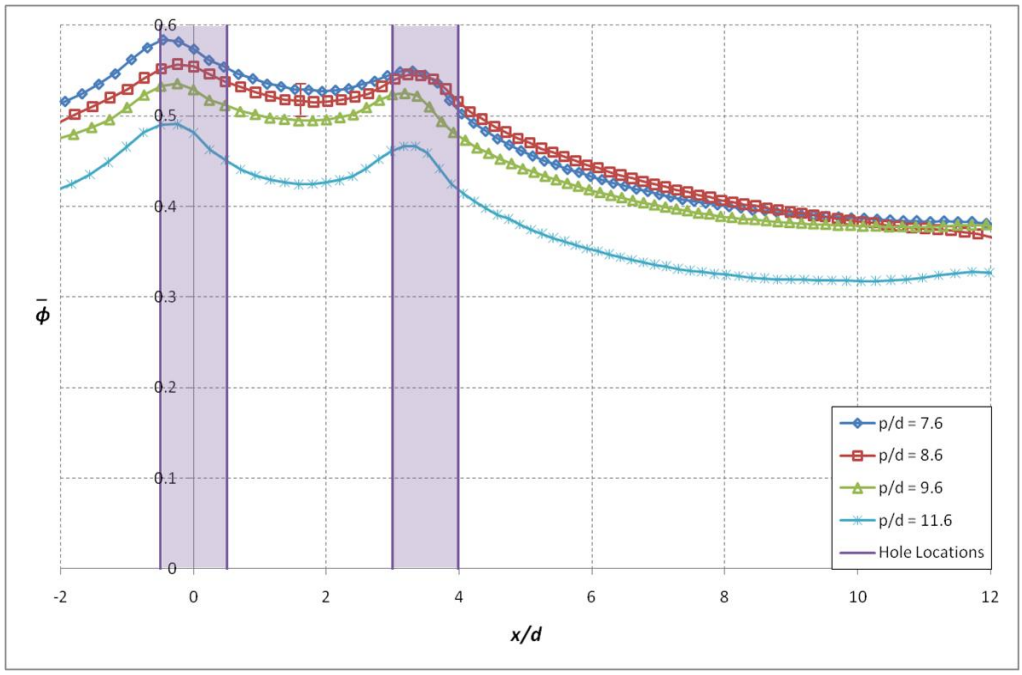

Figure 3.2.7: $\bar{\phi}$ vs. *x/d* for *M* = 3.0

Figure 3.2.8 shows the comparison of $\bar{\phi}$ for *M* = 0.5. No data were available for *p/d* = 9.6 or 11.6. Using the conventional uncertainty limits it would appear that *p/d* = 8.6 was likely outperforming *p/d* = 7.6 on the stagnation line. However, this particular blowing ratio suffers from additional uncertainty, so it is

unlikely that this actually represents an increase in $\bar{\phi}$ when increasing *p/d* from 7.6 to 8.6.

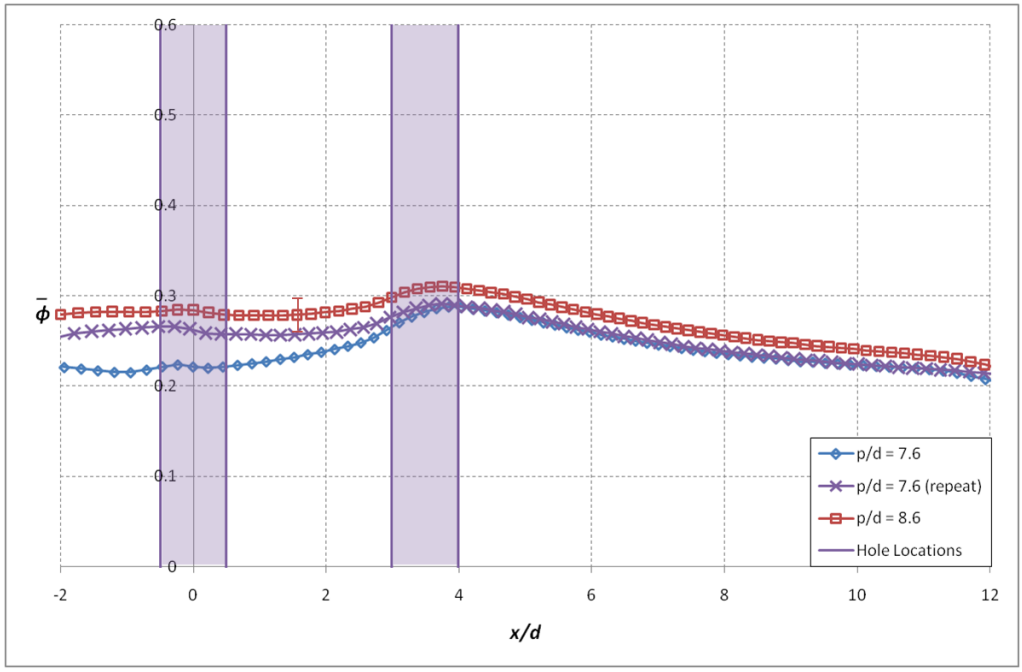

Figure 3.2.8: $\bar{\phi}$ vs. *x/d* for *M* = 0.5

3.2.2 Effects of α Variation on $\bar{\phi}$ with Varying Pitch

The adiabatic effectiveness results showed some dramatic changes under changing angle of attack. Maikell [22] did the same study with a conducting model, which showed the same trends, but with the largest $\Delta\bar{\phi}$ being 0.05 compared to a maximum $\Delta\bar{\eta}$ of 0.2. Given these results there was an expectation that an increased pitch would not produce substantial changes, even though there was the potential for differing coolant distribution to affect the results.

The overall change was much like what was seen with blowing ratio variation. For *p/d* = 7.6, 8.6 and 9.6 there was little difference between models. A further increase to *p/d* = 11.6 caused a noticeable reduction, between 10 and 20% depending on the conditions. However, a comparison of the performance change at various pitches showed that models at an increased pitch were perhaps slightly less sensitive to changes in angle of attack than *p/d* = 7.6.

Figure 3.2.9 shows $\bar{\phi}$ for all tested angles of attack at *p/d* = 7.6 reproduced from Maikell [22]. There was a marked decrease in performance on the negative side for all angles, as the coolant was swept away from this side. The positive side also saw some degradation for α = 1.5° and 4.6°, due to reduced coverage from the stagnation row of holes. At α = 7.7°, the performance improved due to the previously discussed improved adiabatic effectiveness. In comparison, the data for *p/d* = 9.6 (Figure 3.2.10) had less degradation in performance visible. In fact, for the majority of the *x/d* range, the variation was considerably less than the uncertainty. Even the largest visible changes – the drop relative to α = 0° at α = 4.6° and the improvement at α = 7.7° downstream of the off-stagnation row – only produced a change in $\bar{\phi}$ of 0.03. The same level of insensitivity to α was also observed for *p/d* = 8.6. The plot of $\bar{\phi}$ under changing α for *p/d* = 11.6, presented in Figure 3.2.11, shows a return to levels of performance degradation on the negative side similar to *p/d*= 7.6 in magnitude ($\Delta\bar{\phi}$ = 0.04), but the positive side remained insensitive.

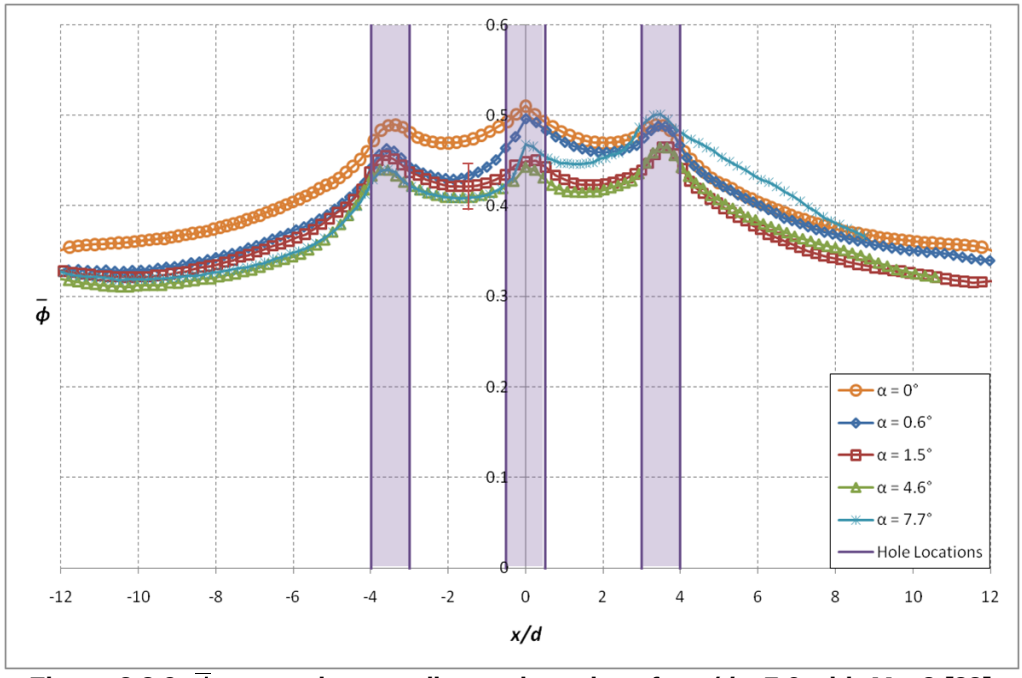

Figure 3.2.9: $\bar{\phi}$ comparison at all tested α values for *p/d* = 7.6 with *M* = 2 [22]

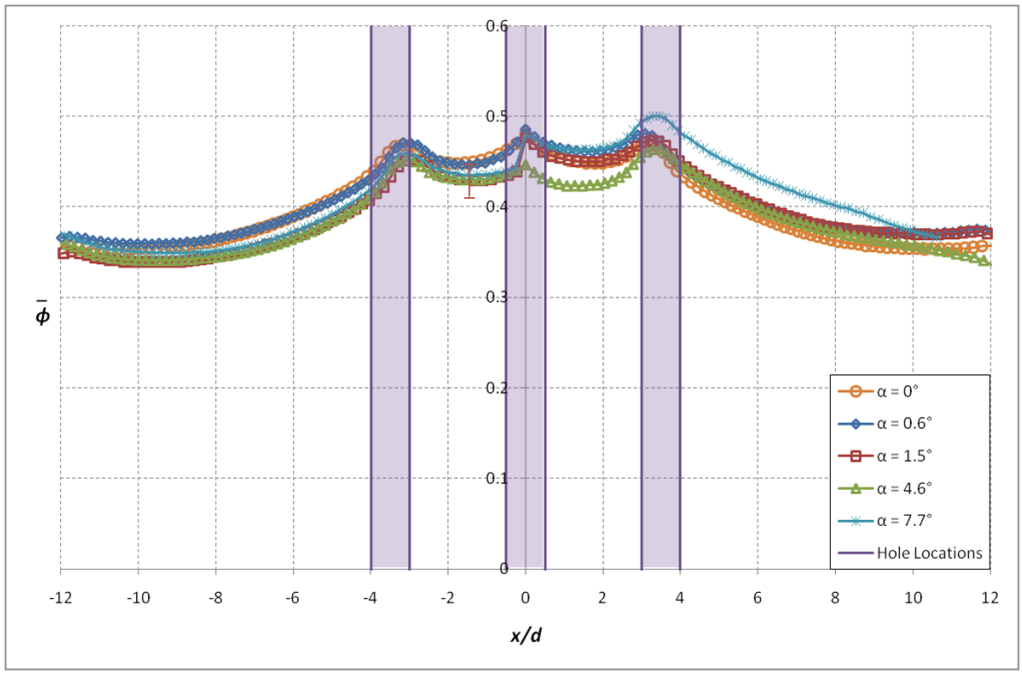

Figure 3.2.10: $\bar{\phi}$ comparison at all tested α values for *p/d* = 9.6 with *M* = 2

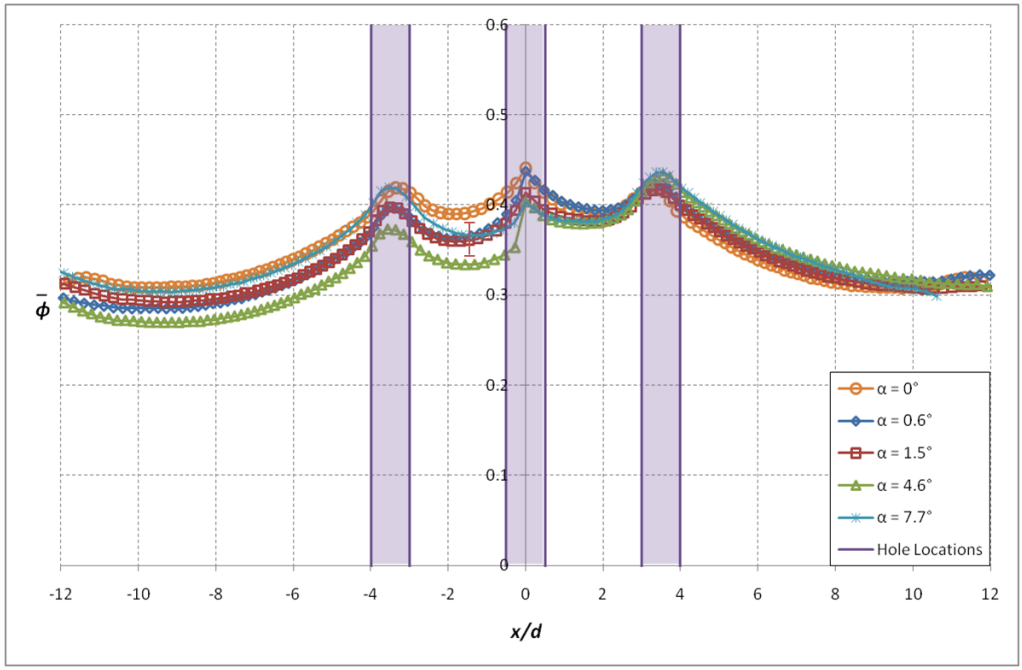

Figure 3.2.11: $\bar{\phi}$ comparison at all tested α values for *p/d* = 11.6 with *M* = 2

At α = 1.5° and 7.7° for *p/d* = 9.6 and α = 4.6° for *p/d* = 11.6 there were noticeable step increases in $\bar{\phi}$. As a reminder, these plots are composites of two separate images. Nominally, the data at *x/d* = 0 should be identical for both, however there was a combined effect of increased *x/d* uncertainty for the -α data (due to increased angle relative to the camera) and averaging additional points inside the holes on the positive side. Figure 3.2.12 shows the lateral distribution for *p/d* = 11.6 and *x/d* = 0 at positive and negative angles of attack. The positive side has wider and colder ($\Delta\phi$ = 0.05) hole region, a result of the observation angle, *i.e.* for positive angle of attack the IR camera was imaging deeper into the holes. Outside this area the data are within 0.02 of each other.

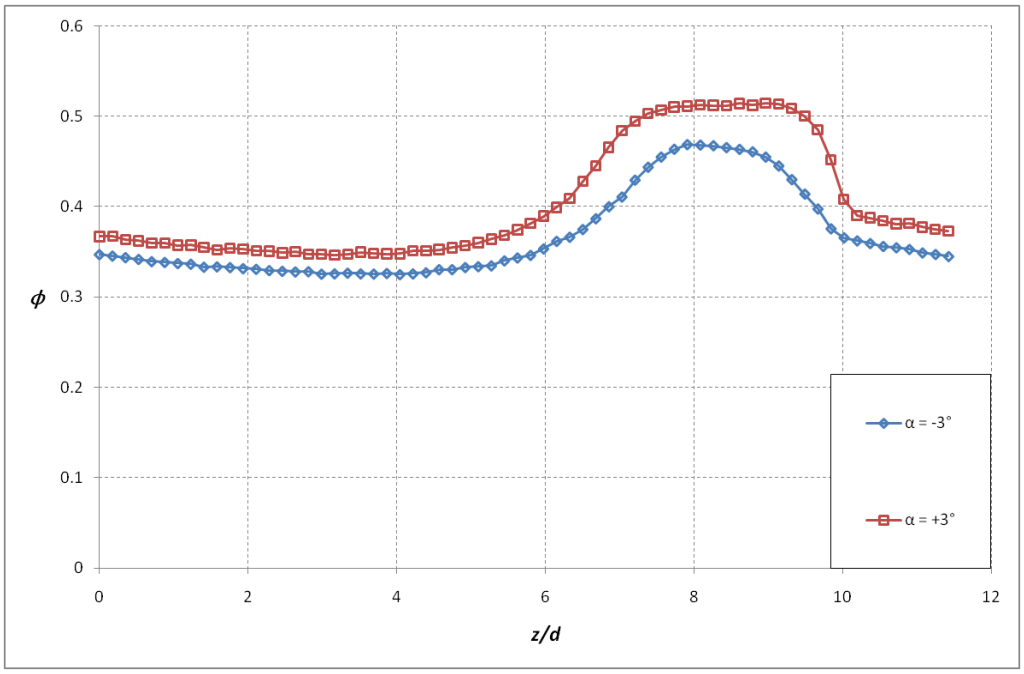

Figure 3.2.12: Lateral comparison of ϕ for *p/d* = 11.6, *M* = 2 at *x/d* = 0

What may not be immediately evident from the plots already presented is that the laterally averaged overall effectiveness for *p/d* = 8.6 was in some cases higher than *p/d* = 7.6. This is more clearly shown in Figure 3.2.13, which compares α = 4.6° for all pitches. The change in $\bar{\phi}$ between *p/d* = 7.6 and 8.6 lies between 0.03 and 0.04 over the entire *x/d* range. This sort of change was most apparent at this angle of attack. For the two smaller values of α, the difference was within experimental uncertainty. For α = 7.7°, $\Delta\bar{\phi}$ was less, making the difference marginal.

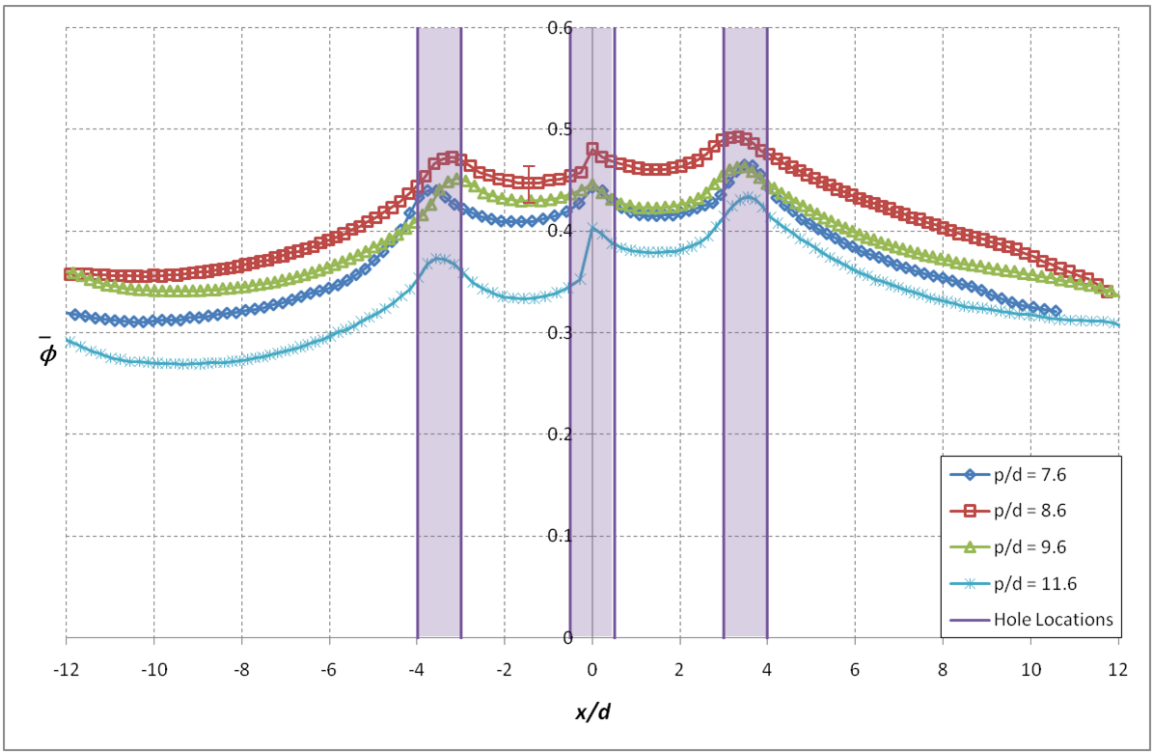

Figure 3.2.13: Pitch variation at *M* = 2.0 and *α* = ±4.6°

Since the lateral position of the off-stagnation row of holes was always positioned at ½ *p* relative to the stagnation row, there was a change in the relative hole stagger. At α = 0°, the effect of changing the stagger is diminished because of the coolant buildup along the stagnation line. This was visible in Figure 3.2.5, where until *p/d* = 11.6 the coolant distribution does not appear to have multiple distinct streams. However, the changes became much more apparent when the coolant from the center row was turned. Contour plots for α = 4.6° (Figures 3.2.14, 3.2.15, 3.2.16 and 3.2.17) show there was a visible progression in the change in coverage. At *p/d* = 7.6, the jet turned from the *x/d* = 0 row of holes intersects the off-stagnation row of holes, likely combining the jets.

For *p/d* = 8.6, the same stream was positioned just on the edge of the hole. At *p/d* = 9.6, the streams were becoming distinct from each other, and *p/d* = 11.6 had definitively separate jets between the two rows. For *p/d* = 8.6 and 9.6, the change in coverage varied with α as the jets turned progressively more with increasing angle of attack, while the *p/d* = 11.6 model always had very little interaction between rows.

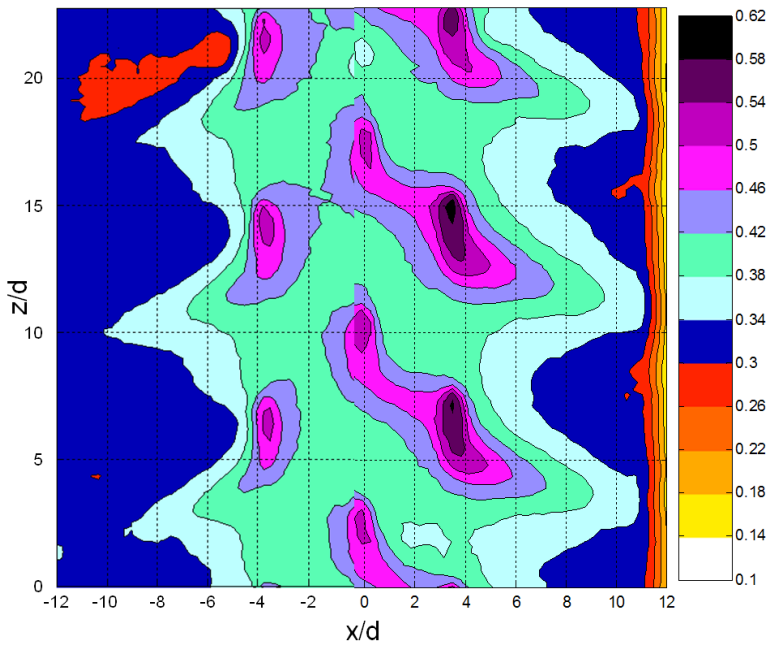

Figure 3.2.14: Contours of ϕ for *p/d* = 7.6 at α = 4.6° and *M* = 2 [22]

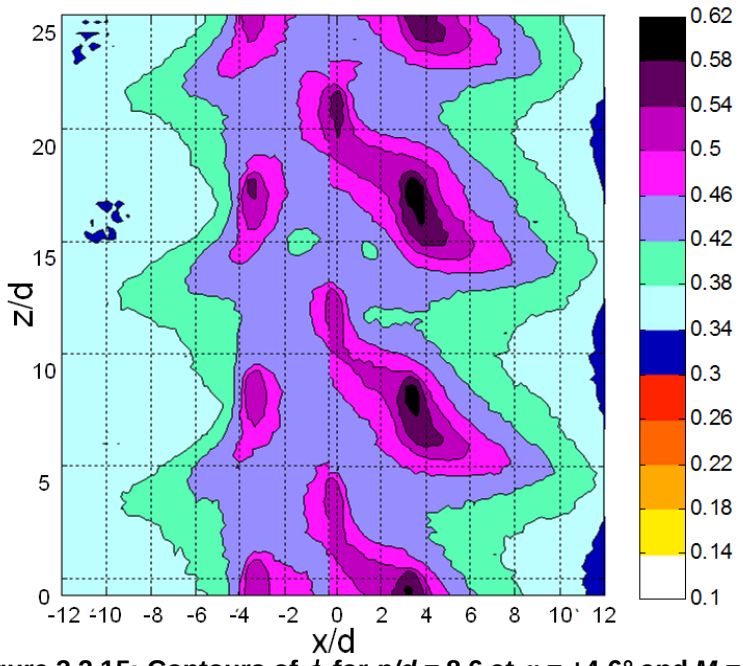

Figure 3.2.15: Contours of ϕ for *p/d* = 8.6 at α = ±4.6° and *M* = 2

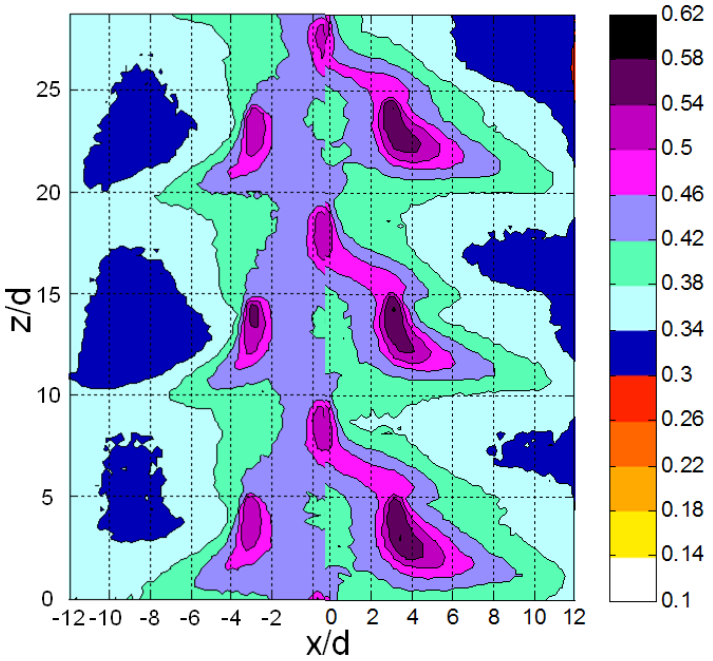

Figure 3.2.16: Contours of ϕ for *p/d* = 9.6 at α = ±4.6° and *M* = 2

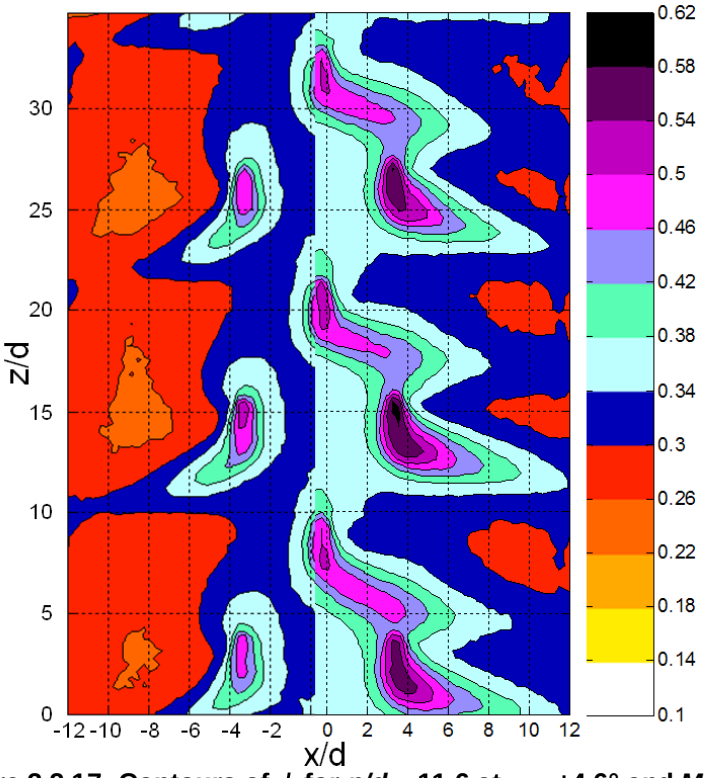

Figure 3.2.17: Contours of ϕ for *p/d* = 11.6 at α = ±4.6° and *M* = 2

The change in coverage does not explain the improvement on the negative side for *p/d* = 8.6 or the relative insensitivity on the negative side for *p/d* = 8.6 and 9.6. Focus so far has been on the potential coolant distribution along the surface. However, the surface temperature was also a product of the heat transfer coefficient distribution, which may also be affected by changing pitch. It is possible for a change in the interaction with the mainstream to alter *h* independent of η. A relatively small change in *h* could account for the small observed change in $\bar{\phi}$.

Ultimately though, the change in performance was small. The conclusion that the change in pitch does not strongly affect $\bar{\phi}$ remains whether the performance went up or down. It should also be noted that the uncertainty analysis does not take into account angle of attack variation. It is possible that the inclusion of α = 0° bias and other factors could add to the uncertainty. Since no data had any repeat points, the assumption that the uncertainty will remain the same during angle of attack variation as for blowing ratio variation should not be taken lightly.

3.2.3 Simplified Analysis

As the results were analyzed, the small relative change in $\bar{\phi}$ was somewhat perplexing. In order to better understand the physical process responsible for causing ϕ to remain high in spite of the increased surface area per cooling-hole, a one dimensional analysis was performed.

Neglecting radiation, radial conduction and surface convection must balance, which produces the following equations for the internal and external surfaces:

$$h_f\left(T_{aw} - T_{w,o}\right) = -\frac{k\left(T_{w,i} - T_{w,o}\right)}{r_o \ln\left({}^{r_o}/_{r_i}\right)} \tag{3.2.1}$$

$$h_i\left(T_{w,i} - T_{c,i}\right) = -\frac{k\left(T_{w,i} - T_{w,o}\right)}{r_i \ln\left({}^{r_o}/_{r_i}\right)} \tag{3.2.2}$$

In order to express these equations in terms of non-dimensional parameters, the assumption was made that $T_{c,o}$ and $T_{c,i}$ (from the definitions of ϕ and η) are nearly the same. For a conducting model, this is not true. However, Terrell *et al.* [17] found on a model similar to this study's *x/d* = 7.6 model that the temperature change between inlet and outlet was never more than 10%, and less than 5% for *M* > 0.5.

It is also helpful to define two Biot numbers:

$$Bi_o = \frac{h_f r_o \ln\left(r_o/r_i\right)}{k} \tag{3.2.3}$$

$$Bi_i = \frac{h_i r_i \ln\left(r_o/r_i\right)}{k} \tag{3.2.4}$$

When combined with the definitions of ϕ and η, Equations 3.2.1 and 3.2.2 can be solved simultaneously for ϕ. The result,

$$\phi = \frac{Bi_i + \eta Bi_o(1 + Bi_i)}{Bi_i + Bi_o(1 + Bi_i)} \tag{3.2.5}$$

can also be expressed in terms of the heat transfer coefficient ratio h_f/h_i,

$$\phi = \frac{1 - \eta}{1 + Bi_o + \dfrac{r_o h_f}{r_i h_i}} + \eta \tag{3.2.6}$$

which is very similar to the result presented by Johnson *et al.* [31], but for a cylindrical surface.

The purpose of Equation 3.2.6 is to estimate the change in overall effectiveness relative to adiabatic effectiveness. As previously discussed, for many situations it has been well established that an increase in pitch will reduce the average adiabatic effectiveness through introducing additional surface area that is essentially untouched by coolant, effectively reducing $\bar{\eta}$ by exactly the percentage that the pitch was increased. Because of the jet-to-jet interaction for this model, as shown in Figure 3.1.3 (a), it is not expected that the reduction in η would be a direct relation to pitch, but it can be taken as a worst case estimate.

Taking Bi_o and Bi_i to be constant with an increase in pitch (the details underlying these assumptions are not trivial, and can be viewed in Section A.1), the change in ϕ was then estimated as a linear function of η. A final assumption required that $\bar{q}_f'' = \bar{h}_f(\bar{T}_{aw} - \bar{T}_w)$, which is in general not true. An analysis of the results calculated using lateral averages and local values found the difference to be small (~5%). The result was that a calculation using laterally averaged values should still offer reasonable results.

This analysis is most valid far away from the highly three-dimensional conduction around the film cooling holes. A location of *x/d* = 6 for *M* = 2 was chosen. Under these conditions, Bi_o and Bi_i are approximately 2 and 1 respectively. Laterally averaged adiabatic effectiveness for *p/d* = 7.6 was 0.25. Using this information and the assumptions already discussed, Equation 3.2.6

predicted that $\bar{\phi}$ = 0.40 for *p/d* = 7.6, which is exactly the value measured at *x/d* = 6 in the experiment. When $\bar{\eta}$ was reduced by 26% to simulate an increase in *p/d* to 9.6, the resulting prediction was $\bar{\phi}$ = 0.35. This represents a 13% change, somewhat more than the 4% change that was measured. However, this serves to show that if changes in pitch alter the adiabatic effectiveness, the overall effectiveness will change a smaller amount.

This analysis primarily serves to show that ϕ is reduced less than η under an increase in pitch. Consider then that the adiabatic effectiveness in the vicinity of the jet was not expected to change under increasing pitch. The difference between pitches with regard to $\bar{\eta}$ comes from the introduction of additional area where η = 0. Then, considering that ϕ is less dependent on surface conditions, and that conduction from areas that are still cooled equally well will act to buffer changes, the lateral distribution of temperature would seem to stretch to accommodate the new pitch, reaching a new minimum in only a very small region. An illustration of this is shown in Figure 3.2.18, which displays a lateral ϕ distribution for all the tested pitches at *x/d* = 2. With the exception of *p/d* = 11.6, the peak under the jet was nearly the same, while the minimum had changed significantly. The change in ϕ_{min} from *p/d* = 7.6 to 8.6 was a negligible 3%, but at *p/d* = 9.6 there was a more substantial 10% drop in ϕ_{min}. The *p/d* = 11.6 data were substantially warmer throughout, suggesting that the internal cooling had been affected. For *x/d* = 6, shown in Figure 3.2.19, the situation was similar. Here, perhaps due to row-to-row jet interaction effects, the minimum overall

effectiveness was approximately the same for *p/d* = 7.6, 8.6 and 9.6, but the hotter region was clearly elongated as the pitch increased.

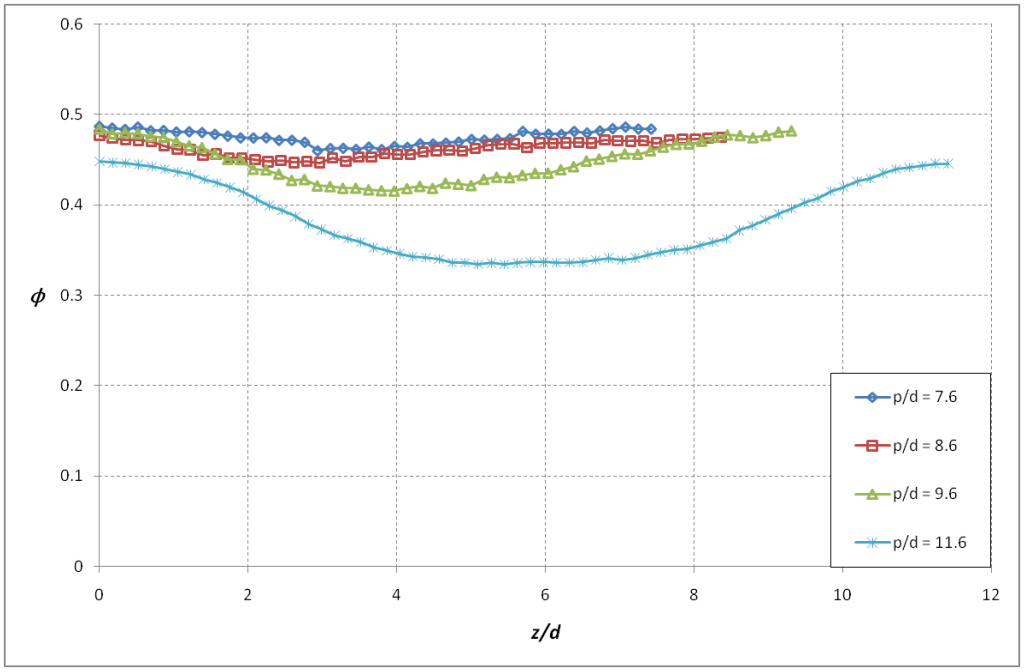

Figure 3.2.18: Lateral ϕ at *x/d* = 2 for *M* = 2 and α = 0°

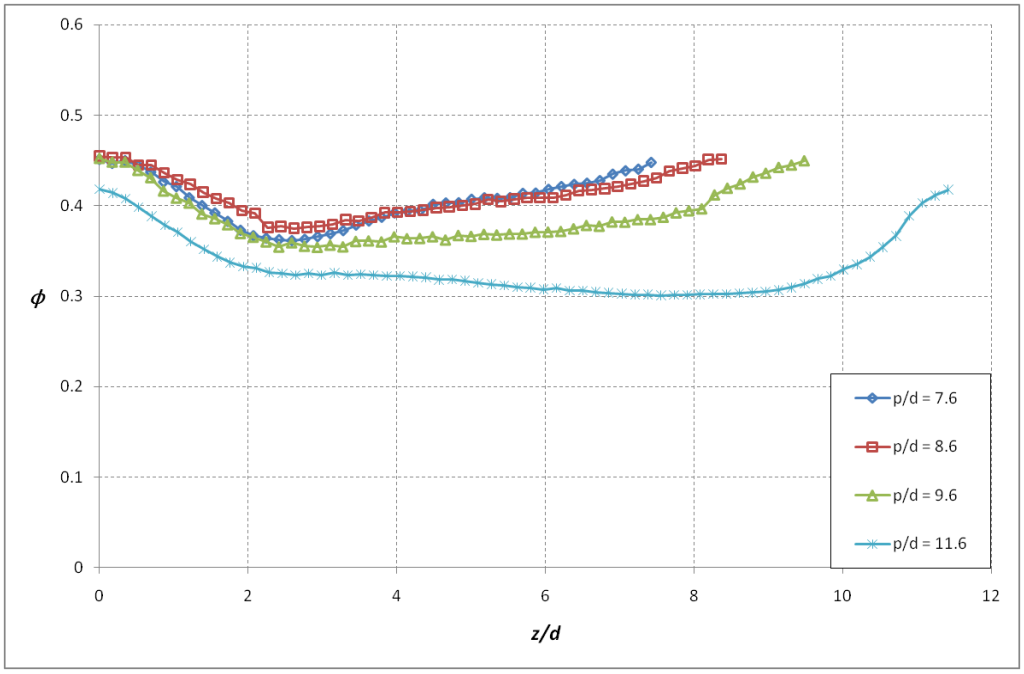

Figure 3.2.19: Lateral ϕ at *x/d* = 6 for *M* = 2 and α = 0°

3.3 Effects of Pitch Variation Using ϕ_{min} Analysis

A key feature of this study was the inclusion of "hot spot" analysis. This form of analysis, fully described in Section 2.4, allows easy comparison of all the hottest points over the whole *x/d* range. Since these points often limit the life of a part, it is perhaps more important to understand performance in terms of ϕ_{min} than $\bar{\phi}$. Normally, this might be done through examination of contour plots, but in most cases plotting the minimum overall effectiveness versus *x/d* produces a clearer comparison due to the resolution requirements of the contour.

It has already been shown that at some locations the laterally averaged overall effectiveness was obscuring larger changes in local ϕ between *p/d* = 7.6 and 9.6. Even though the $\bar{\phi}$ only changed a negligible amount, the hottest points,

those between coolant streams, could change substantially. Under blowing ratio variation, the most notable differences were observed in the 0 < *x/d* < 4 region.

Figure 3.3.1 compares all the pitches at *M* = 2. Once again, *p/d* = 7.6 and 8.6 were nearly identical. It is interesting to note that $\Delta\phi_{min}$ between *p/d* = 7.6 and 9.6 was slightly greater than that seen using $\bar{\phi}$ (Figure 3.2.4). When comparing the region between rows of holes for these pitches, the $\bar{\phi}$ analysis only showed $\Delta\bar{\phi}$ = 0.02, while the ϕ_{min} analysis shows $\Delta\phi_{min}$ = 0.03. Beyond the off-stagnation row of holes the difference was no longer outside the margin of uncertainty. The difference between *p/d* = 7.6 and 11.6 pitch was more pronounced using this analysis method. Again, the *x/d* region between the off-stagnation rows of holes showed the greatest difference, with $\Delta\bar{\phi} - \Delta\phi_{min}$ as high as 0.05. This can be seen visually in Figure 3.3.2. Like the $\bar{\phi}$ plots, as *x/d* increases the difference between pitches was reduced.

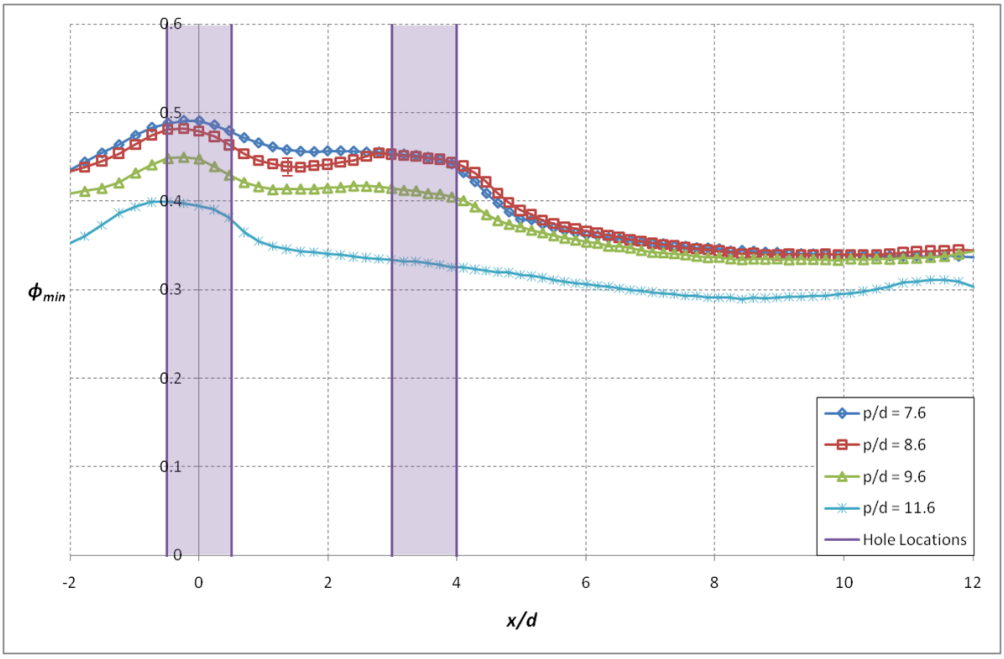

Figure 3.3.1: ϕ_{min} plot for *M* = 2 and α = 0° with all four values of *p/d*

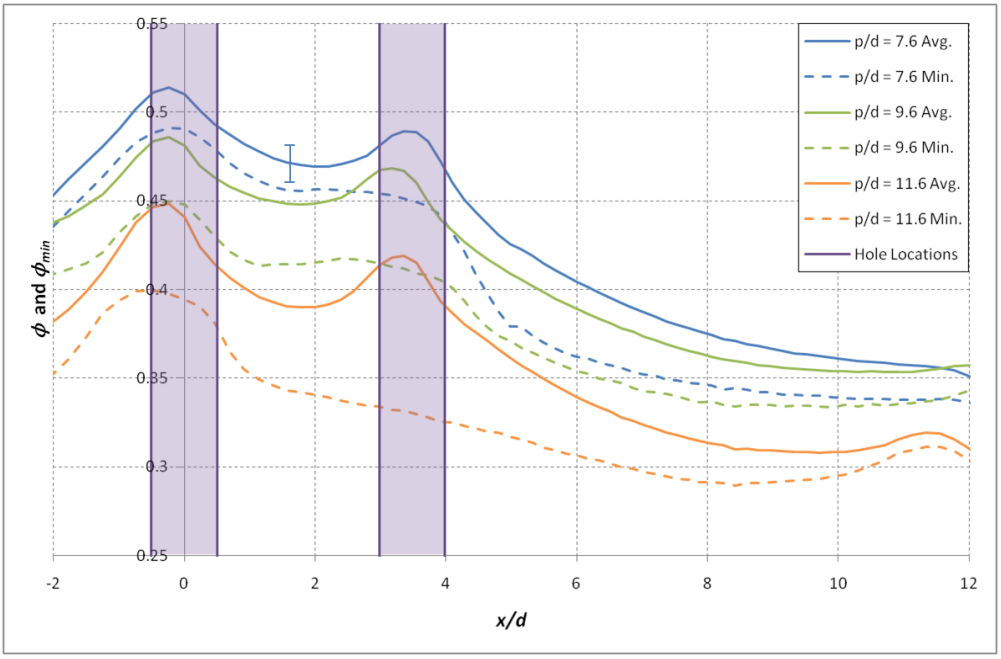

Figure 3.3.2: Comparison of $\overline{\phi}$ and ϕ_{min} for *p/d* = 7.6, 9.6 and 11.6 at *M* = 2. Note the enlarged scale.

These data clearly show the benefit of using a hot spot analysis. The remaining values of *M* showed similar changes in $\Delta\bar{\phi}$ vs. $\Delta\phi_{min}$. While it was uncommon for a ϕ_{min} plot to show a change outside the uncertainty margin that did not show up in conventional $\bar{\phi}$ plots, a more pronounced drop in ϕ_{min} compared to $\bar{\phi}$ was observed for *p/d* = 11.6 at all values of *M*, which can be observed in Figure 3.3.3.

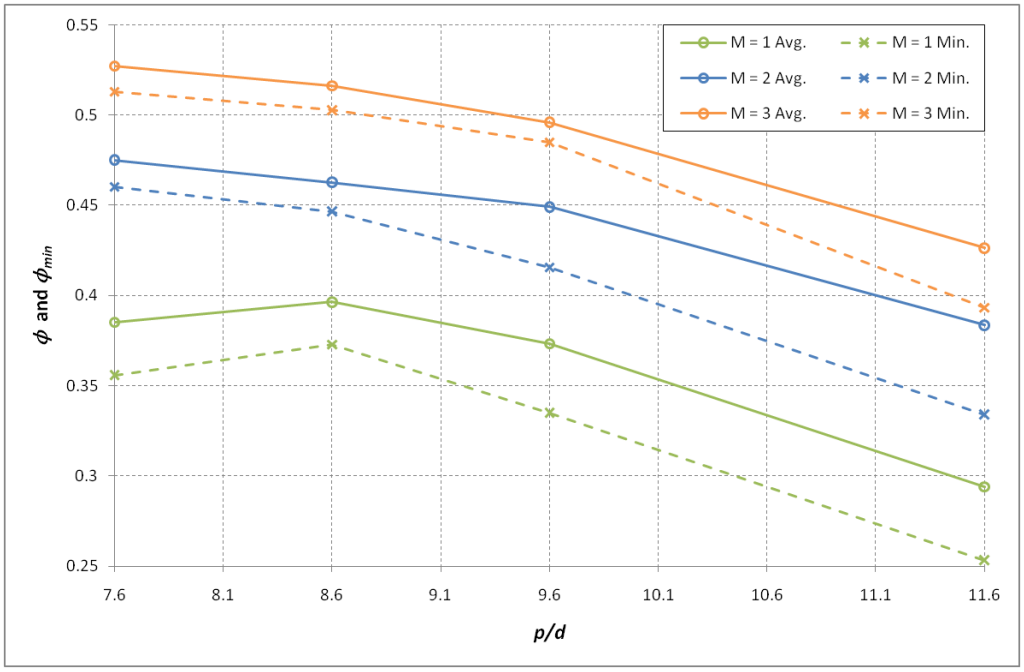

Figure 3.3.3: Comparison of $\bar{\phi}$ and ϕ_{min} for all pitches with *M* = 2 and α = 0° at *x/d* = 2

3.3.1 Effects of α Variation under Varying Pitch Using ϕ_{min} Analysis

A hot spot analysis was also undertaken on data with varying angle of attack. Like all the other data, *p/d* = 7.6, 8.6 and 9.6 were generally shown to be very close to each other. The hot spot analysis did better show the difference

between the closer pitches for low angles. Figure 3.3.4 compares all the pitches at α = ±0.6°. Unlike the $\bar{\phi}$ analysis, the *p/d* = 9.6 data were clearly differentiated from the other pitches on the positive side between the stagnation line and the off-stagnation holes even at this small change in angle of attack.

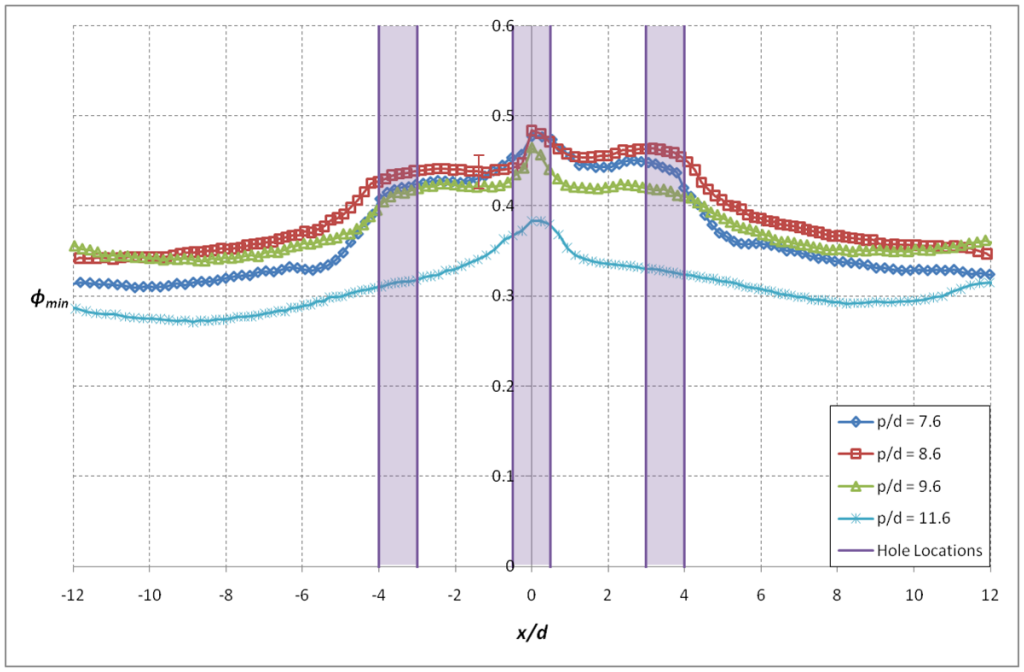

Figure 3.3.4: ϕ_{min} plot for *M* = 2.0 and α = ±0.6°

Figure 3.3.5 shows a comparison of all pitches at α = ±4.6°. Like the $\bar{\phi}$ plot of the same data, *p/d* = 8.6 was well above *p/d* = 7.6. However, using this analysis the $\Delta\phi_{min}$ between these pitches was in the 0.04 to 0.05 range, making the possibility that the *p/d* = 8.6 test was an outlier somewhat less likely. Something which helps support the idea that changing mainstream interaction could be affecting *h* is also visible. Recall that the stagnation line is nominally

located at *x/d* = -2. This would normally be the location where the highest heat loading would be expected, and without any film coverage, temperatures should be notably higher. Instead there was a region between the holes around *x/d* = 1 that was markedly warmer than the equivalent point at *x/d* = -1 ($\Delta\phi_{min}$ = 0.04) for *p/d* = 7.6 and 9.6. This indicates that the side with less coolant, and lying nearer the expected stagnation line, was actually colder. However, if jet interaction was instead creating a wider stagnation region, *h* would be substantially reduced, allowing the change observed.

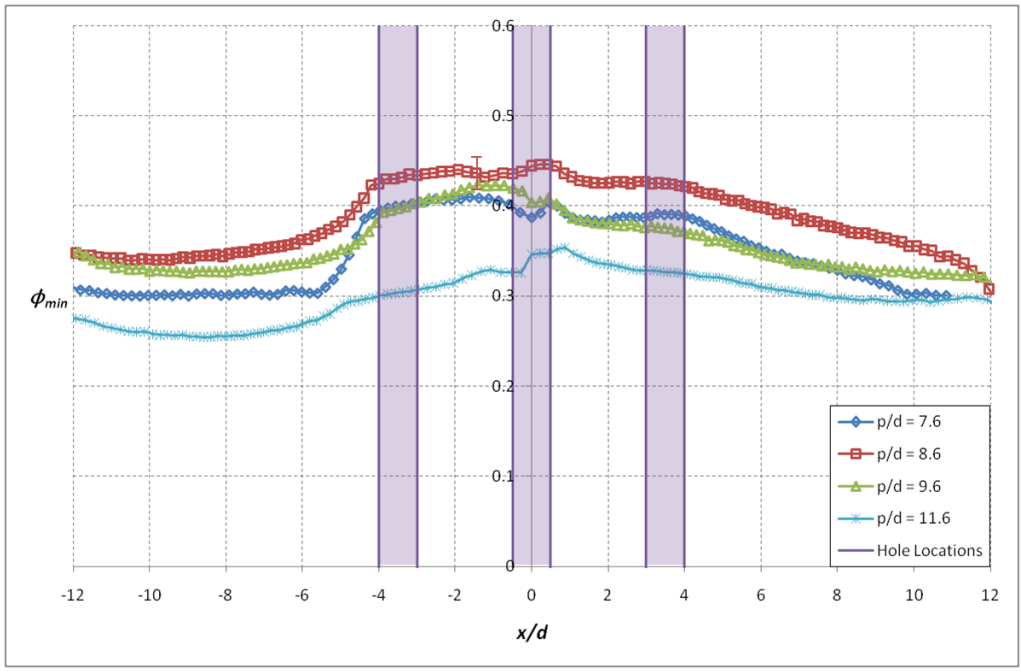

Figure 3.3.5: ϕ_{min} plot for *M* = 2.0 and α = ±4.6°

The small drop in ϕ_{min} with change in angle of attack was very similar to that observed using $\bar{\phi}$ analysis. The most significant differences were observed

in the range 0.5 < *x/d* < 3. For example, Figure 3.3.6 compares several angles for *p/d* = 7.6. In this region, $\bar{\phi}$ had a minimum of 0.41, while ϕ_{min}dropped as low as 0.38. A difference of 0.03 seems small, but $\Delta\phi$ of 0.05 could represent halving of part life. It is also interesting to note that between the holes on the negative side, $\bar{\phi}$ and ϕ_{min} were equal. This was because with all the coolant pushed to one side of the model or the other, this area was cooled purely through conduction. This could be seen in the contour plots, which show a nearly uniform temperature.

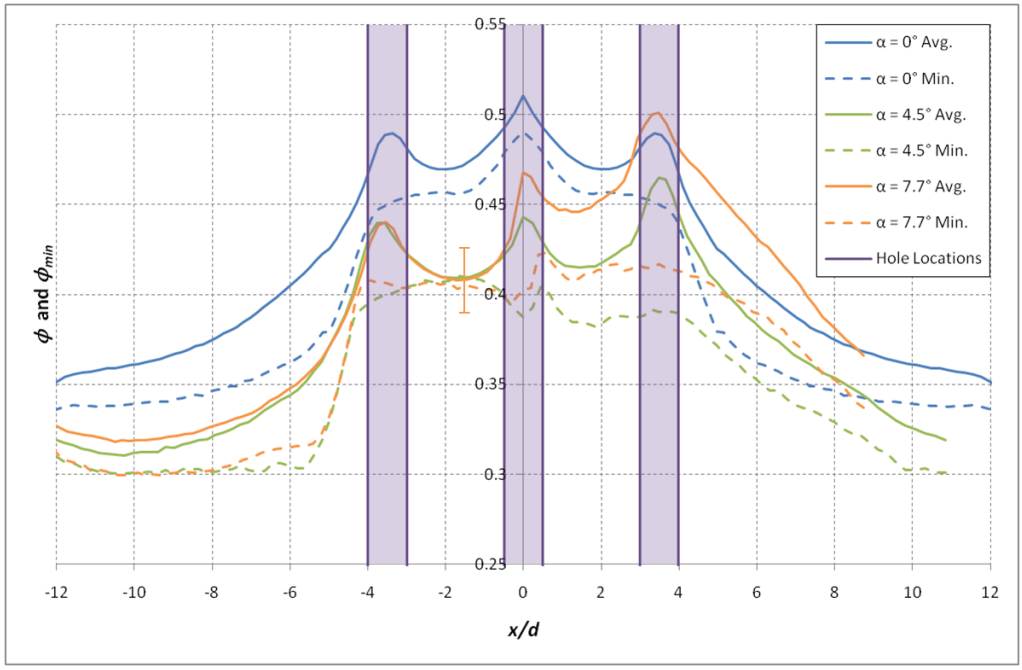

Figure 3.3.6: Comparison between ϕ_{min} and $\bar{\phi}$ for some α values at *p/d* = 7.6 and *M* = 2. Note the expanded scale.

3.4 Effects of Pitch Variation Using Constant Mass Flow Analysis

When the pitch is increased, the size of the coolant holes remains the same while the area each hole must cool increases. Thus far, comparisons have been made between equivalent values of *M*, *i.e.* a constant mass flow rate from each hole. Consequently, for these comparisons the mass flow per unit area decreases with increasing pitch. It is also relevant to compare the performance on a constant total coolant mass flow rate basis. To do this, data are compared using *M/(p/d)*. This parameter is equivalent to scaling the mass flux of the model by the normalized area. This method makes sense from the standpoint of having a constant amount of available coolant mass flow, so increasing the pitch would reduce the number of holes overall, resulting in an increase in the amount of coolant through each hole. Using the spatially averaged overall effectiveness, $\bar{\bar{\phi}}$, this form of comparison is made in Figure 3.4.1. For comparison, the same data are presented relative to *M* alone in Figure 3.4.2. It is unclear whether *M* or *M/(p/d)* provides a better scale for the data, though *p/d* = 11.6 falls somewhat closer to the remaining pitches using the constant mass flow comparison.

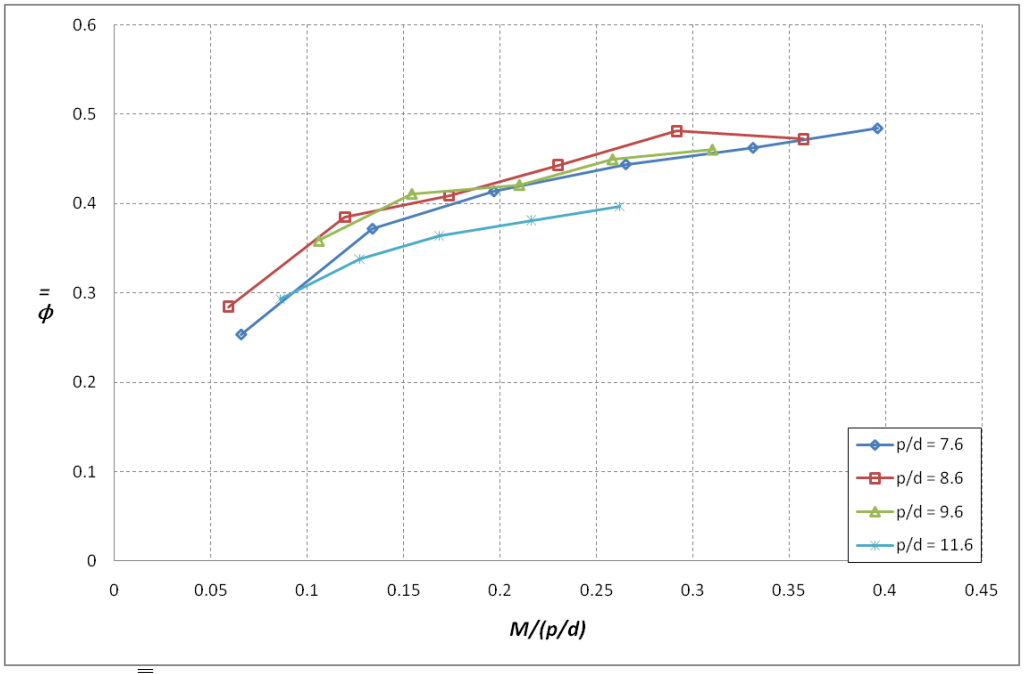

Figure 3.4.1: $\bar{\bar{\phi}}$ comparison plot for all values of *p/d* using constant overall mass flow

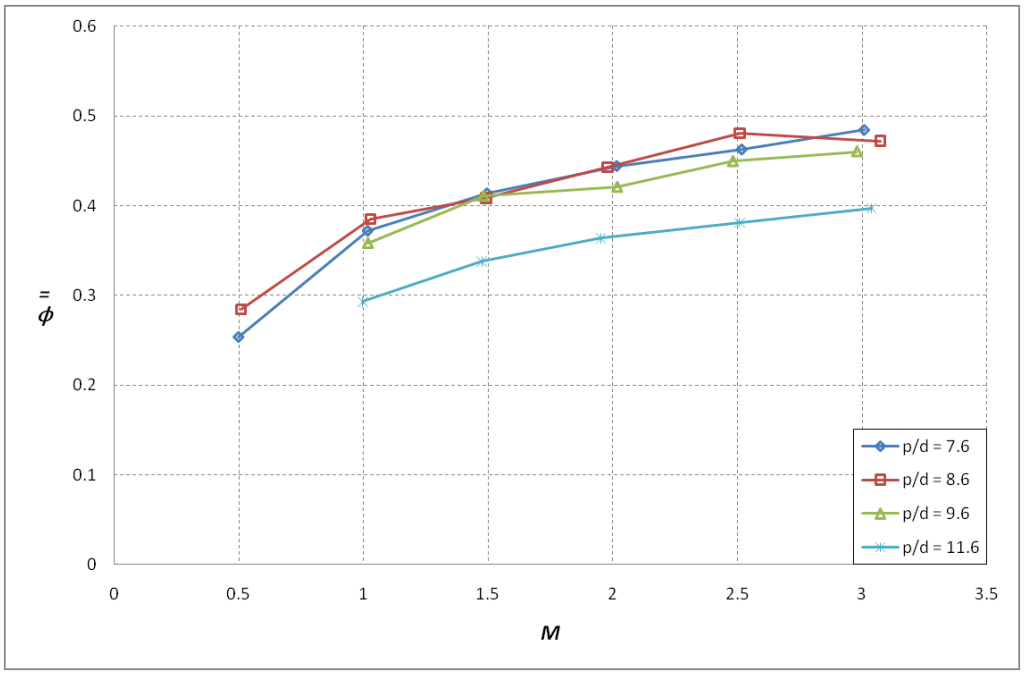

Figure 3.4.2: $\bar{\bar{\phi}}$ comparison plot for all values of *p/d* using constant mass per hole

It is interesting to note that when using either scale *p/d* = 7.6, 8.6 and 9.6 fall (within uncertainty) along the same line. This suggests that a given performance target could be achieved by increasing *M* as the coolant holes are spread out. However, this is not sustainable, as at some point the pitch will be large enough that the cooling holes will be effectively isolated and $\bar{\bar{\phi}}$ must decrease. This has clearly occurred at *p/d* = 11.6, where the data become separated from the other pitches. It was previously remarked that the overall effectiveness drop for *p/d* = 11.6 was about 15% relative to *p/d* = 7.6. This plot shows that in order to make up the difference, total coolant flow would have to be increase by roughly 30% to achieve the same level of performance. For the other values of *p/d*, maintaining the same total coolant flow rate while increasing the pitch would retain the same level of $\bar{\bar{\phi}}$.

Another interesting plot that can be taken from the $\bar{\bar{\phi}}$ data is a comparison of overall effectiveness as a function of pitch alone, shown in Figure 3.4.3. This helps illustrate how performance with pitch was relatively level before significantly dropping as the pitch was further increased.

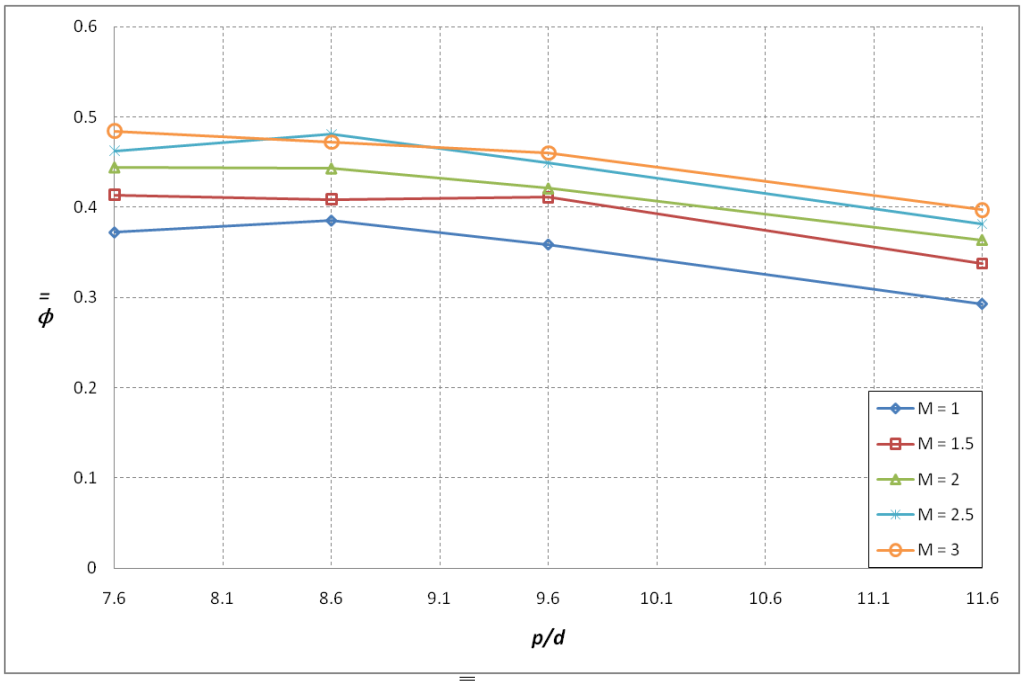

Figure 3.4.3: Comparison of $\overline{\overline{\phi}}$ vs. *p/d* for all tested blowing ratios

3.5 Internal Cooling

One of the additional goals of this study was to examine the effect of internal cooling on ϕ, internal temperature and heat flux. As part of that goal, internal temperature sensors were installed for three of the pitches to establish a temperature profile. Additionally, for *p/d* = 7.6, an attempt was made to use heat flux sensors to measure q_i'', which was then reduced to h_i. These data are compared to the literature in terms of Nu_j and Re_j, the relevant non-dimensional parameters scaled with the diameter of the impingement jet.

3.5.1 Internal Temperature Profiles

Often in the impingement literature, different designs are compared in terms of a non-dimensional temperature similar to η. For this study, there was the opportunity to measure internal effectiveness, ϕ_i, a reflection of metal temperature on the inner surface of a simulated blade. As shown in Figure 2.2.6, a number of thermocouples were installed to take readings at various positions. Only data for *p/d* = 7.6, 8.6, and 9.6 were measured. For the *p/d* = 7.6 configuration, a "no impingement" condition was also tested. For this test, the impingement plate was removed entirely, but the same flow parameters (*DR*, *M*, etc.) were maintained.

Of interest to this study was the effect of pitch variation on the internal temperature profile. Figure 3.5.1 compares ϕ_i profiles for all pitches tested and the no impingement condition at *M* = 2. First, it is notable that the wall temperature at 0° was constant within uncertainty for all pitches. Since this position was centered directly beneath the impingement jet, the lack of change in temperature there could have been merely due to the high h_i at that location. However, data collected at different *z/d* locations shown in Figure 3.5.2 revealed that the temperature profile was quite uniform, so the center temperature can be considered representative.

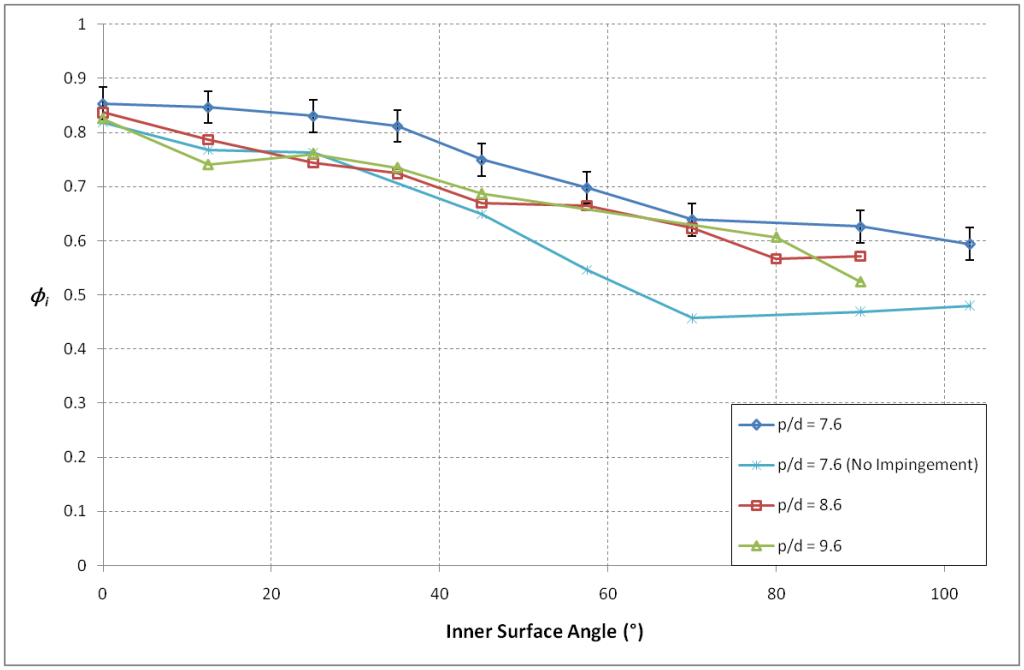

Figure 3.5.1: Comparison of ϕ_i for *M* = 2 and *p/d* = 7.6, 8.6, and 9.6 with no impingement

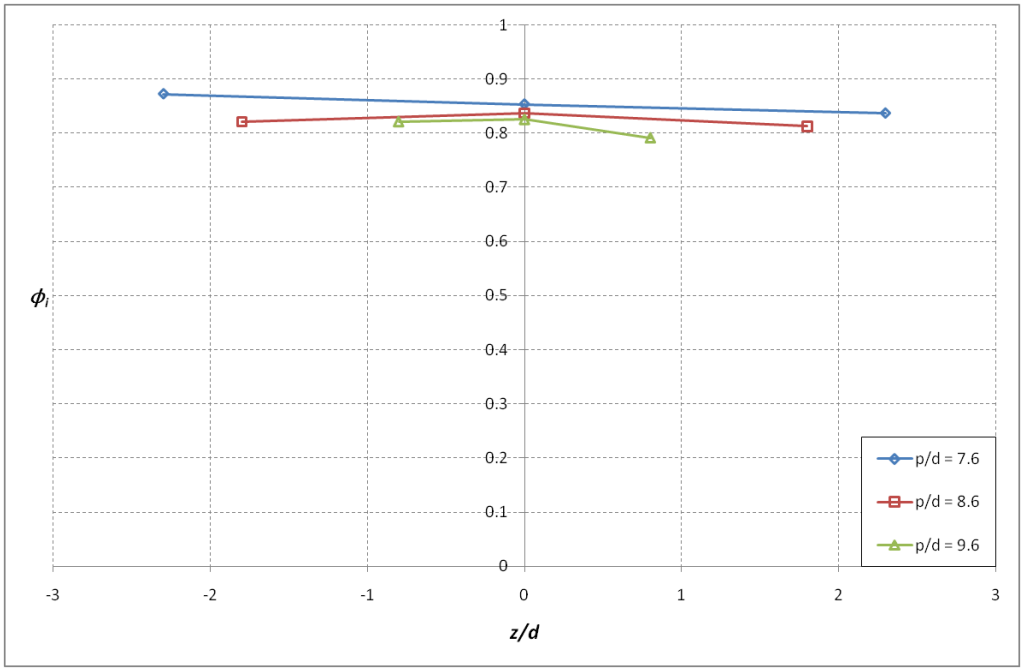

Figure 3.5.2: Temperature uniformity at the 0° position

Between 0° and 45°, the *p/d* = 8.6 and 9.6 data were distinctly warmer than *p/d* = 7.6, which was expected. However, the fact that *p/d* = 8.6 and 9.6 were indistinguishable was not. The difference between these two pitches and *p/d* = 7.6 was near $\Delta\phi_i$ = 0.08 (~10%) in this region. This is interesting since the drop in $\bar{\phi}$ for the same region on the external surface was less (~0.04, or ~5%), and often hard to measure for the change in pitch from *p/d* = 7.6 to 9.6. Since internal temperature notably increased while external temperature remained nearly constant, this lends to the theory that through-hole convective cooling was the main compensating factor for any increased heat load due to higher pitch. Further away from the cooling holes, all three pitches came closer together with the exception of the 90° point. All tested values of *M* produced very similar looking plots in terms of the relative performance between pitches and, consequently, they are not presented.

The removal of the impingement plate also served to substantially increase the internal temperature. From 0° to 45° the level of change was the same as that observed by increasing the pitch from *p/d* = 7.6 to 8.6 or 9.6. However, where the pitch variation data collapsed together the no-impingement case continued to diverge, leveling off at $\Delta\phi_i$ = 0.14. These trends in internal temperature, and, presumably, h_i, could explain why the external temperature was not notably affected by removal of the impingement plate except far downstream of the holes, as seen in Figure A.2.1.

It is also interesting to compare to Ravelli *et al.*'s [21] computational predictions for the internal temperature profile. Figure 3.5.3 shows comparisons at the thermocouple locations for her data alongside the measured values for *p/d* = 7.6 with impingement cooling, and Figure 3.5.4 shows the same comparison with no impingement plate. With impingement, the predictions were within experimental uncertainty for surface angels greater than 25° at *M* = 2. However predictions with an impingement plate for *M* = 1 were much colder compared to the measured values, generally around $\Delta\phi_i$ = 0.09, though the temperature gradient was correctly predicted. Without impingement, the agreement was good for surface angles greater than 25° for both *M* = 1 and *M* = 2. These data validate the use of Ravelli *et al*.'s predictions in estimation of placement uncertainty, which used computed gradients near the 45° position.

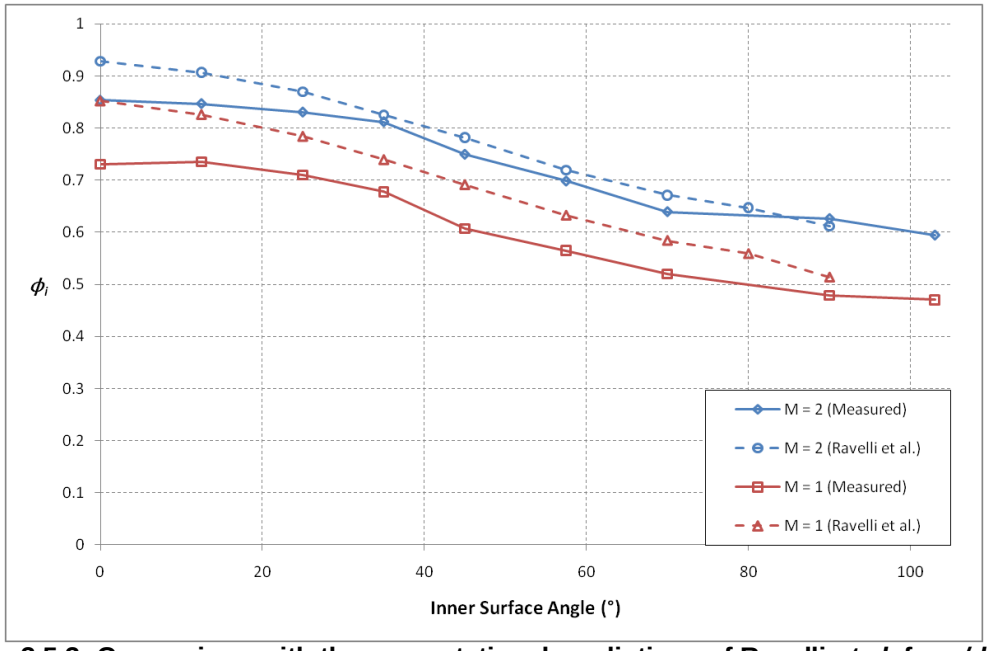

Figure 3.5.3: Comparison with the computational predictions of Ravelli *et al*. for *p/d* = 7.6 using impingement cooling with a metal plate

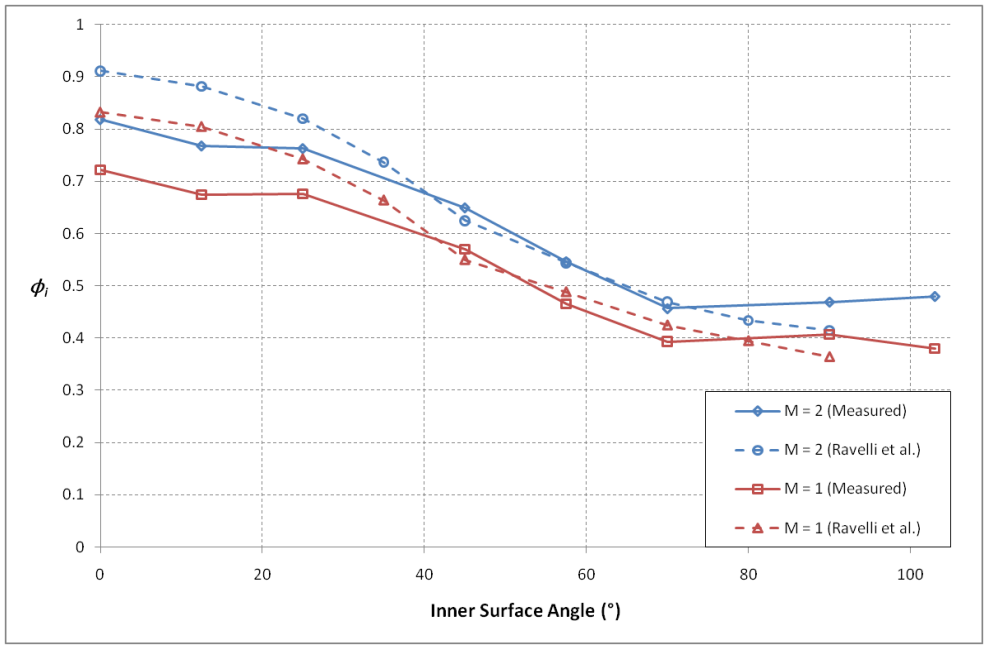

Figure 3.5.4: Comparison with the computational predictions of Ravelli *et al*. for *p/d* = 7.6 with no internal impingement

These data also provide an explanation for the lack of impact of impingement cooling near the coolant holes. They showed that even though h_i increased by approximately a factor of three when impingement cooling was added, the temperature remained nearly the same. This was because the temperature difference between the wall and the fluid was so small that even large changes in the heat transfer coefficient produced only small changes in the total heat flux. Their prediction of h_i was somewhat supported by the heat flux measurements made for this study, though none of that data were good enough to provide accurate estimates of h_i. Also, their correct prediction of the performance trends for both cases, as shown in Figure 3.5.5, lends strength to this argument.

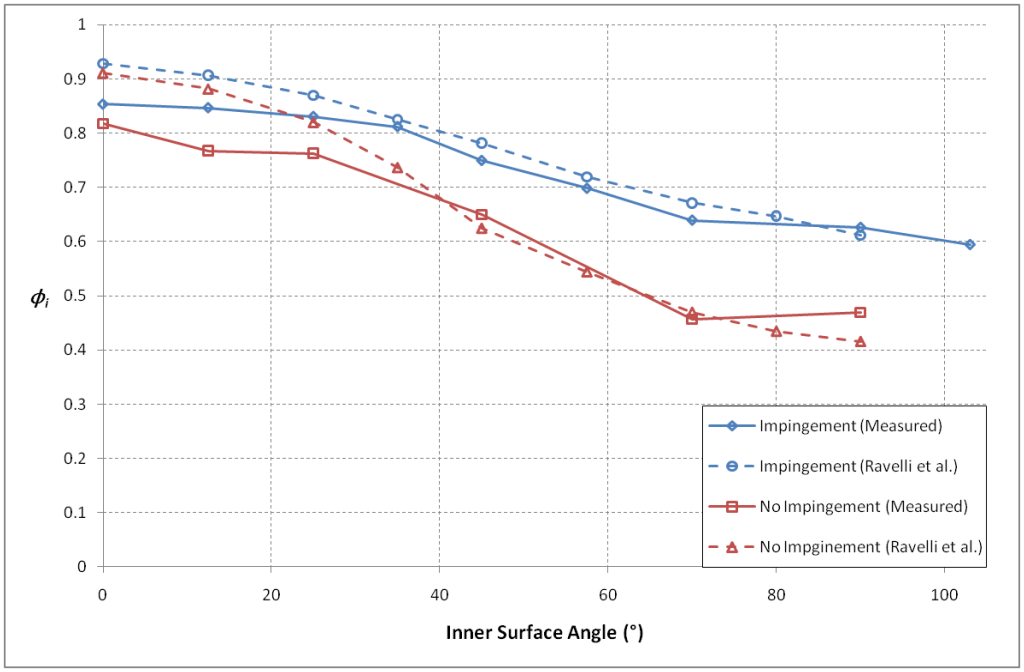

Figure 3.5.5: Comparison between measured values of ϕ_i and the computational predictions of Ravelli *et al*. with impingement and without for *M* = 2

3.5.2 Internal Heat Flux

Given the difficulty in using the heat flux gauges, it was very desirable to compare to data in the literature as validation of the experimental method. Other than the computational work of Ravelli *et al*. [21], no study could be found which matched the experiments performed for the current study. The main difference between this study and all others was the use of a "fully confined" jet – a setup where cooling gas can only escape through holes in the target plate – and a curved target surface. It is unknown how much the flow field in the test section varies when compared to a standard confined jet. Excepting that parameter, the works of Bunker and Metzger [32] and Taslim *et al*. [33] matched the best with the conditions of this study, and are presented in Figure 3.5.6. However, some

discussion is required to appreciate the differences between these results and that of the current study.

The closest match located was the data of Bunker and Metzger [32], which still had several differences. First, as with most impingement studies, the cooling air was not exhausted out of cooling holes. Their setup used a simulated leading edge which contained a cylindrical section of varying radius set into an isosceles triangle with an apex of 36°. Using relative curvature defined as the ratio of the diameter of the inset section, D_i, to the diameter of the coolant jet, d_j, they tested several values including 0.48 and 0.2. This is important because the majority of their results were presented for d_j/D_i = 0.48 but the value used for the current study was 0.2. Their comparison showed that near the stagnation point, the laterally averaged Nusselt numbers were slightly different, with the larger relative curvature being slightly greater (~10%). However, beyond x/d_j ~1, the Nu_j curves collapsed together, indicating that their d_j/D_i = 0.48 data may be reasonably compared to this study's 0.2 data. Further, they used a slightly closer jet-to-target spacing of 5.1, compared to the 5.6 used in this study. A closer spacing will produce higher values of Nu_j, but the magnitude of the change should be small for data this close together. Bunker and Metzger's p/d_j was 4.67 compared to this study's value of 4.8.

The study of Taslim *et al*. [33] used a jet-to-target spacing of 5.2 and their relative curvature was 0.37, slightly larger than this study's but within the range evaluated by Bunker and Metzger as being relatively constant. Taslim *et al*. also

made use of a considerably shorter p/d_j of 1.98. Bunker and Metzger's data also showed that increasing pitch from 3.33 to 4.67 did not appreciably affect laterally averaged Nu_j for $x/d_j > 2$, with only a small effect (~10%) nearer the stagnation point. However, Taslim *et al*.'s data were reported as spatial averages over the range x/d_j ±1.6. For large relative curvatures, peak Nu_j is not located directly beneath the jet, occurring instead in the range $0 < x/d_j < 2$, presumably where strong vortexes form along the wall. The exact location depends on Re_j and geometry. For this reason it was expected then that the Taslim *et al*. data would have significantly higher Nusselt numbers.

Additionally, Chupp *et al*. (1969) formulated a correlation for leading edge impingement cooling:

$$Nu_{stag} = 0.44 Re_j^{0.7} \left(\frac{d_j}{p}\right)^{0.8} e^{-0.85\left(\frac{\zeta}{d_j}\right)\left(\frac{d_j}{p}\right)\left(\frac{d_j}{D_i}\right)^{0.4}} \tag{3.5.1}$$

The details of their setup and the ranges over which their correlation was considered valid were not fully specified, but encompassed the p/d_j and jet-to-target spacing used in this study. Their maximum relative curvature was 0.17, which should still provide a good comparison. The primary weakness of this correlation is that the jet Reynolds number range extended only to Re_j = 10,000. For this study, everything except the jet Reynolds number was constant, which reduced the relation to 0.075 times the Re_j term.

Figure 3.5.6 compares the previously discussed data with that of this study and the simulation of Ravelli *et al*. at the stagnation point location. As expected, the data from Taslim *et al*. show substantially higher Nu_j values than the current study. Though only one point from Bunker and Metzger overlapped the tested Re_j range, it fell within experimental uncertainty of the data. Ravelli *et al*. over-predicted Nu_j, especially for the higher jet Reynolds number. The correlation from Chupp *et al*. was reasonably close to measured values, and was within experimental uncertainty for $Re_j \leq 10{,}000$. However, Han *et al.* [28], the reference from which the Chupp *et al*. correlation was extracted, suggest that the exponent of Re_j might be closer to 0.6 for curved surfaces. They presented a correlation by Hrycak (1981), which used a constant of 0.65, but remarked that there were insufficient data to produce an adjustment to this constant for different relative curvatures. Using 0.6 for the Reynolds number power and adjusting the constant such that the first data point aligned with the Chupp *et al.* correlation, the relation became:

$$Nu_{stag} = 0.16 Re_j^{0.6} \tag{3.5.2}$$

This relation is also plotted, and can be seen to match the data well for all Reynolds numbers.

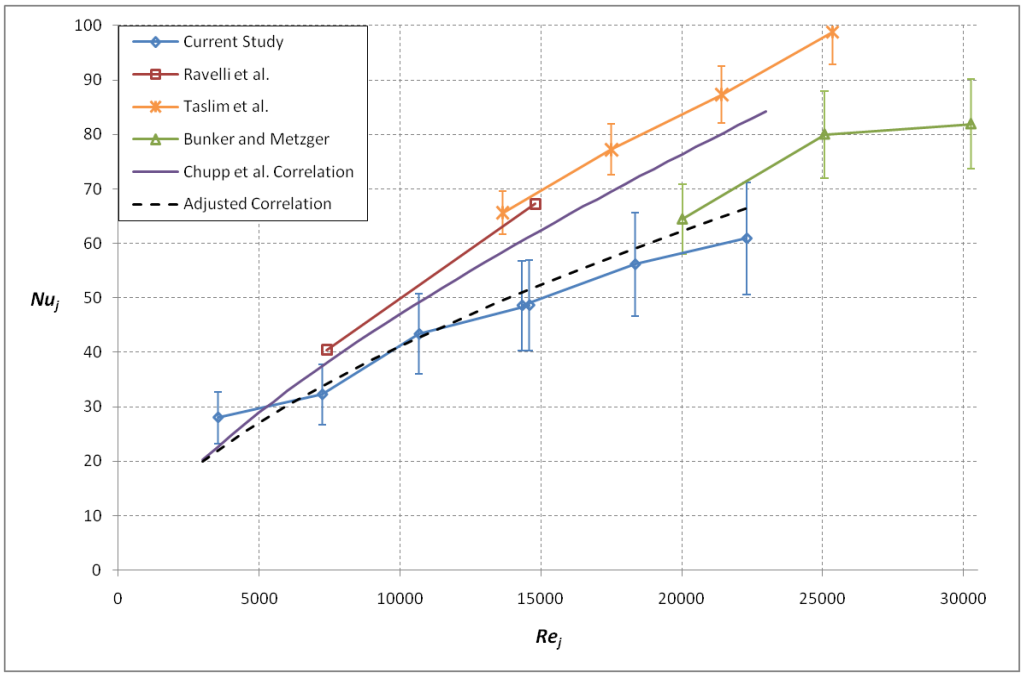

Figure 3.5.6: Nu_j vs. Re_j comparison for internal impingement with data from the literature and Ravelli *et al*.'s computational predictions for $x/d_j = 0$

The same comparison is made at the 45° position (x/d_j = 1.96) in Figure 3.5.7. The agreement here between the data of Bunker and Metzger and this study was poor. This is likely due to a change in the position of the Nu_j peak resulting from the differences in geometry between studies. The location of the peak is sensitive to jet-to-target spacing and other factors. Ravelli *et al*. once again over-predicted heat transfer, though they were nearly within experimental uncertainty. Adjusting the constant in Equation 3.5.2 to 0.09 produced a good fit to the data.

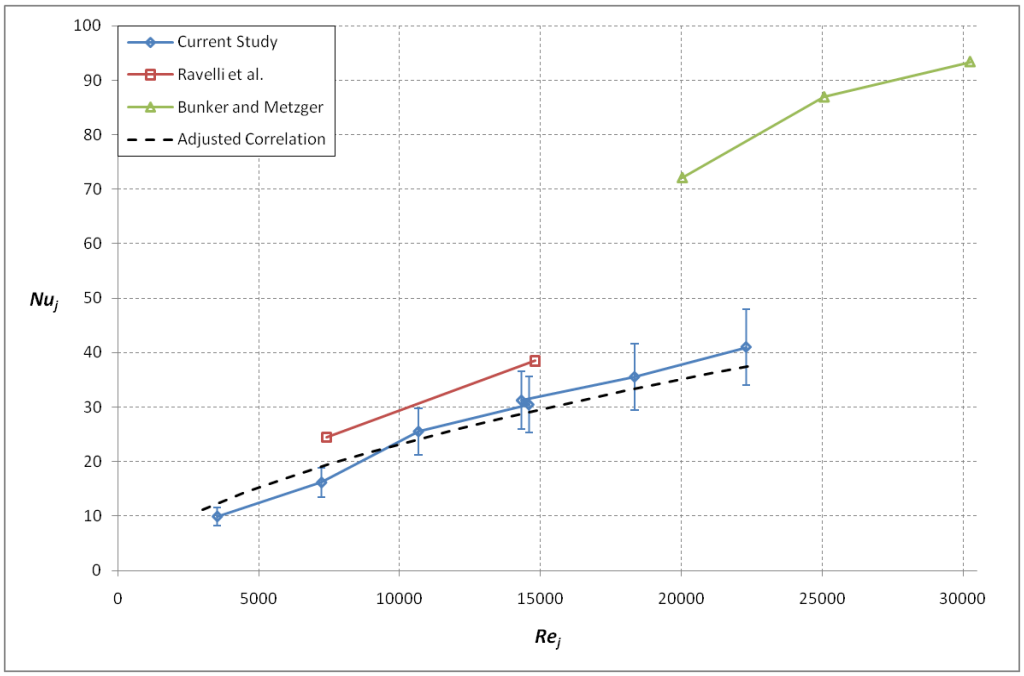

Figure 3.5.7: Nu_j vs. Re_j comparison for internal impingement with data from the literature and Ravelli *et al*.'s computational predictions for $x/d_j = 2$

3.6 External Heat Flux Data

One method for evaluating film cooling performance has been the net heat flux reduction, NHFR. Mouzon *et al*. [16] showed that even though there are strong gradients in the NHFR, the resulting gradients in surface temperature were comparatively smooth. This study aimed to further elucidate the behavior of heat flux on the surface by measuring it directly. Unfortunately, the heat flux gauges were only able to produce reliable data when considering a ratio, producing the h/h_0 ratio as discussed in Chapter 2. Additionally, the majority of positions investigated did not produce good data. Only three positions could be used: x/d = 4.9, z/d = 8.7; x/d = 4.9, z/d = 10; and x/d = 1.8, z/d = 6.2. Most

unfortunately, all the gauges nearer the coolant jets did not produce good data. The h/h_0 data obtained are presented in Figure 3.6.1.

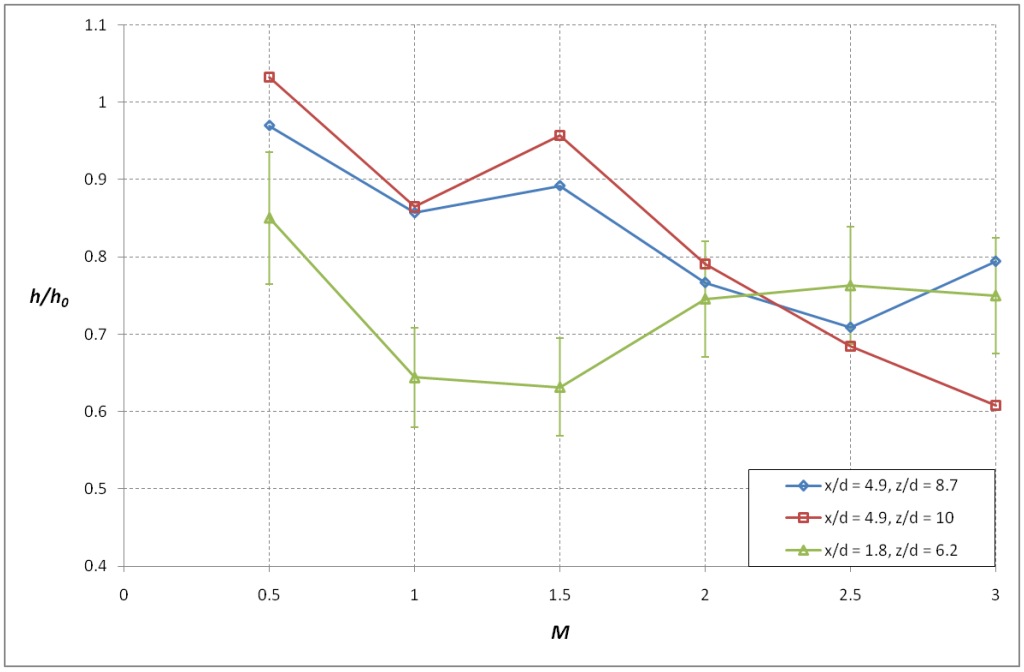

Figure 3.6.1: h/h_0 for all available positions on the external surface with p/d = 7.6

When examining the change in h/h_0, it is useful to see the accompanying η contours. Figures 3.6.2 and 3.6.3 show all the tested blowing ratios, and have the positions of the three gauges overlaid. The topmost gauge is the x/d = 4.9, z/d = 10 gauge. At the lowest blowing ratio, all three gauges were mostly uncovered by coolant, so heat transfer augmentation was near unity. As M increased to 1, coverage was most improved for the x/d = 1.8, z/d = 6.2 gauge, which is evident with the dramatic reduction in heat transfer ratio. As blowing ratio was further increased, coverage progressively improved for the gauges at x/d = 4.89,

resulting in the steady decrease of heat observed heat transfer augmentation. At the same time, coverage for the *x/d* = 1.75 gauge worsened somewhat before leveling off.

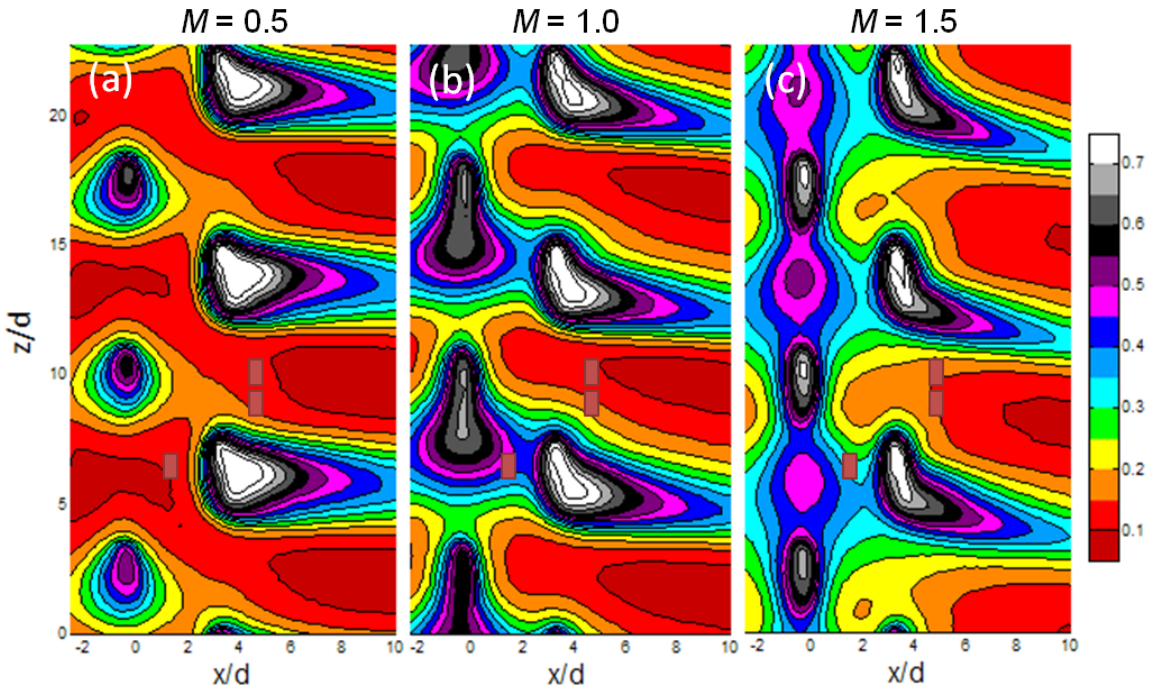

Figure 3.6.2: Contours of η for *M* = (a) 0.5, (b) 1.0 and (c) 1.5 with scale heat flux gauges shown

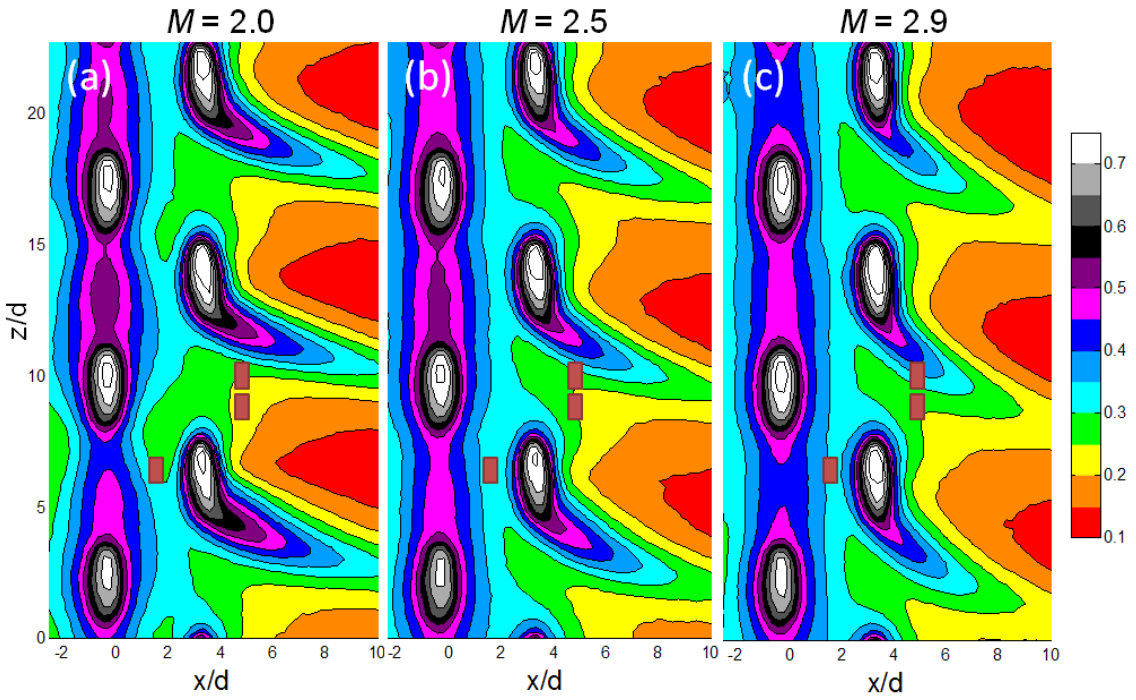

Figure 3.6.3: Contours of η for *M* = (a) 2.0, (b) 2.5 and (c) 2.9 with scale heat flux gauges shown

The heat flux ratio defined by Equation 2.3.3 may provide a more meaningful comparison. Using ϕ_0 data obtained by Dobrowolski [23], the data were reduced to a NHFR. However, these NHFR values were not expected to be the same as NHFR data obtained using the conventional means. The actual surface temperature, which is influenced by factors other than the adiabatic effectiveness, was taken into account, where traditional NHFR calculations are forced to assume a constant surface temperature. Therefore, the traditional method for calculating NHFR (defined with Equation 1.2.8) is really only a prediction of the heat flux ratio. For this study, the real heat flux ratio was measured.

A plot comparing the *x/d* = 4.9, *z/d* = 8.7 with the data from Johnston *et al.* [9] and Mouzon *et al.* [16] is shown in Figure 3.6.4. They made use of shaped holes, which improve η and act to reduce heat transfer augmentation compared to round holes. However, theirs was the most complete data that could be located. A comparison to the single point offered by Johnston *et al*. gives an idea of the level of improvement between hole geometries. The predictions of Mouzon and Johnston both indicate that NHFR should always be greater than zero, *i.e.* the heat flux was always reduced when using film cooling. In stark contrast, the values measured during this study show that under all conditions NHFR was less than zero, indicating that heat flux was always increased. Contrary to the basic concept of the NHFR parameter, this increase in heat flux was not accompanied by an increase in surface temperature.

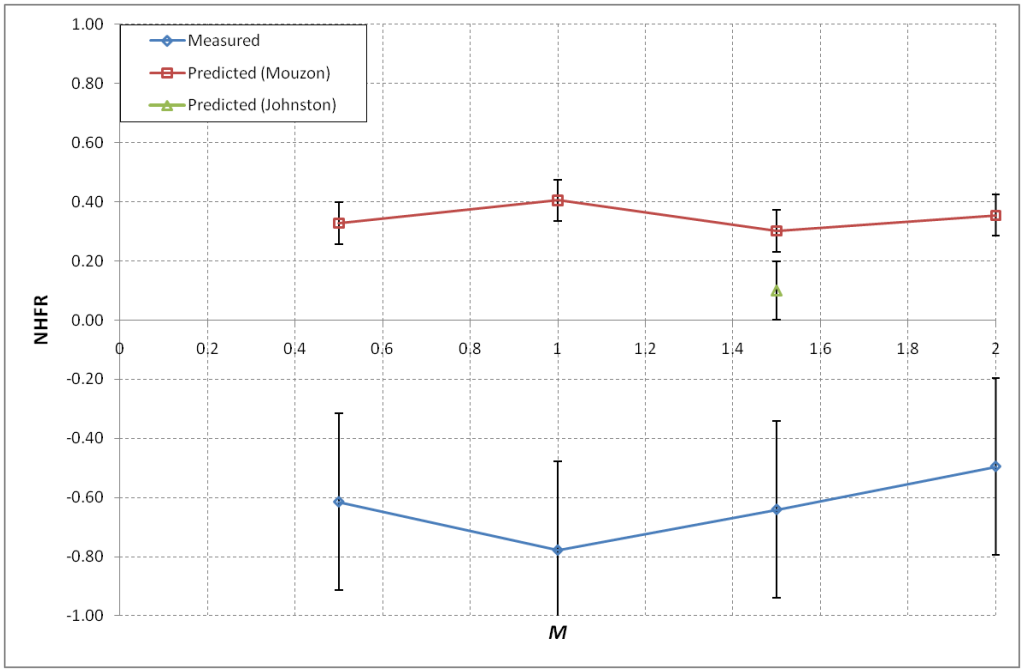

Figure 3.6.4: Overall and adiabatic NHFR for *x/d* = 4.9 and *z/d* = 8.7 with variation in *M* from 0.5 to 2.0 and approximate uncertainty bands

The reason for this contradiction is provided by further examining the assumptions made in the derivation of NHFR. In order to express the ratio q''_f/q''_0 as a relation between η and ϕ, T_w must be assumed to be the same both with and without film cooling. This is clearly incorrect.

Comparing the laterally averaged overall effectiveness with and without film cooling – depicted in Figure 3.6.5 – shows that film cooling always produced much colder temperatures. Even a comparison to ϕ_{min} would show that film cooling has a large benefit. Even if h_f/h_0 were unity, the heat flux would necessarily increase because of the increased temperature difference between the mainstream and the surface. While it is theoretically possible for an extremely

effective film cooling solution to both reduce heat flux and surface temperature, it is much more likely that the additional cooling capacity provided by through-hole convection and surface cooling will always produce an overall increase in heat flux throughout the blade even while reducing the surface temperature. Figures 3.6.6 and 3.6.7 further show that the same inversion of heat flux expectation was maintained at other positions.

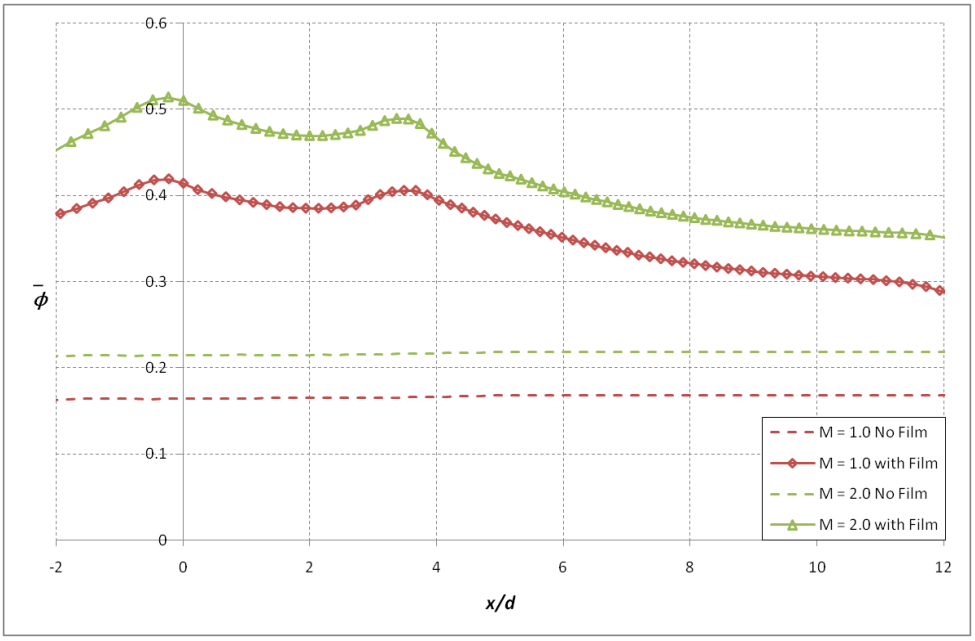

Figure 3.6.5: Comparison of $\bar{\phi}_0$ from Dobrowolski and $\bar{\phi}$ for *M* = 1 and 2

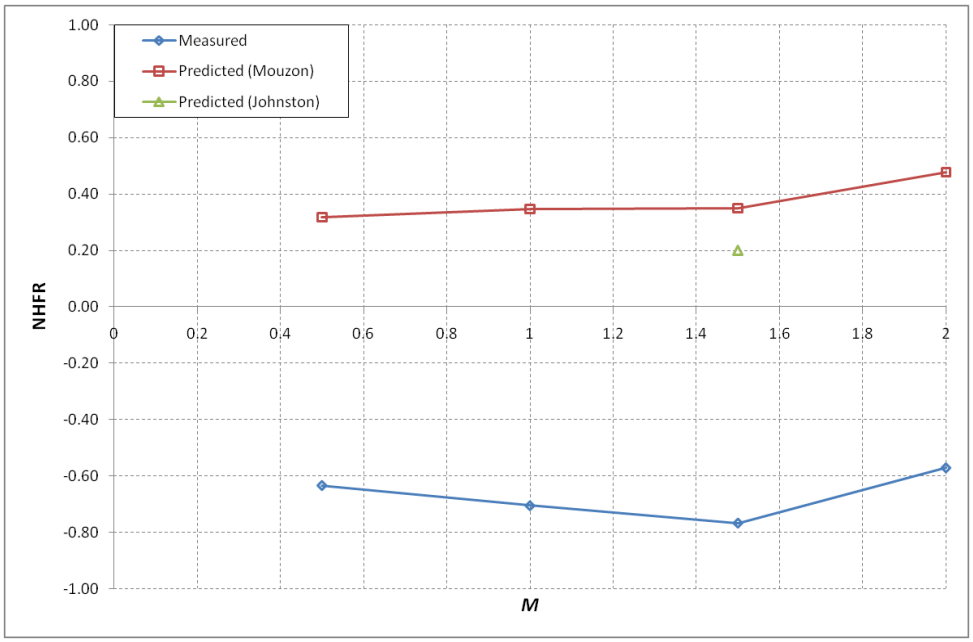

Figure 3.6.6: Overall and adiabatic NHFR for *x/d* = 4.9 and *z/d* = 10 with variation in *M* from 0.5 to 2.0

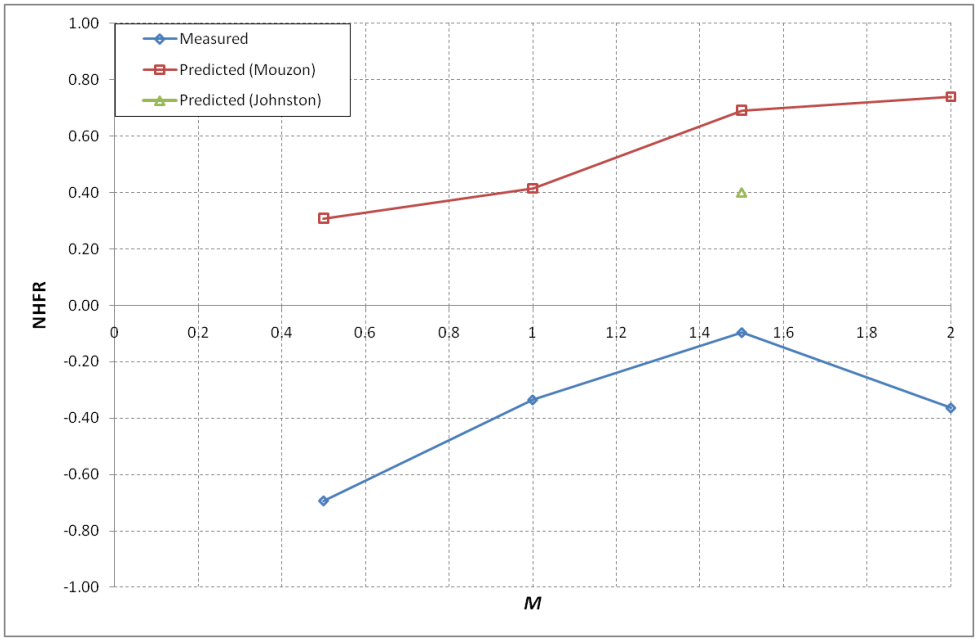

Figure 3.6.7: Overall and adiabatic NHFR for *x/d* = 1.8 and *z/d* = 6.2 with variation in *M* from 0.5 to 2.0

The conclusion here is that measuring NHFR on a conducting model is not a good metric to use in evaluation of film cooling solutions. This may also lead to the idea that traditionally predicted NHFR is a valueless parameter. A better comparison might be the relative surface temperature with and without film cooling as depicted by the ratio ϕ/ϕ_0, shown in Figure 3.6.8. For the two positions at *x/d* = 4.9, the comparison shows that NHFR and ϕ/ϕ_0 both remain relatively constant. However, for the *x/d* = 1.8, *z/d* = 6.2 position, NHFR shows the opposite trend of the surface temperature data. So, NHFR may accurately capture the trend in heat flux (most clearly seen in Figure 3.6.7), but it could still be in error in terms of the parameter that matters most, the actual surface temperature.

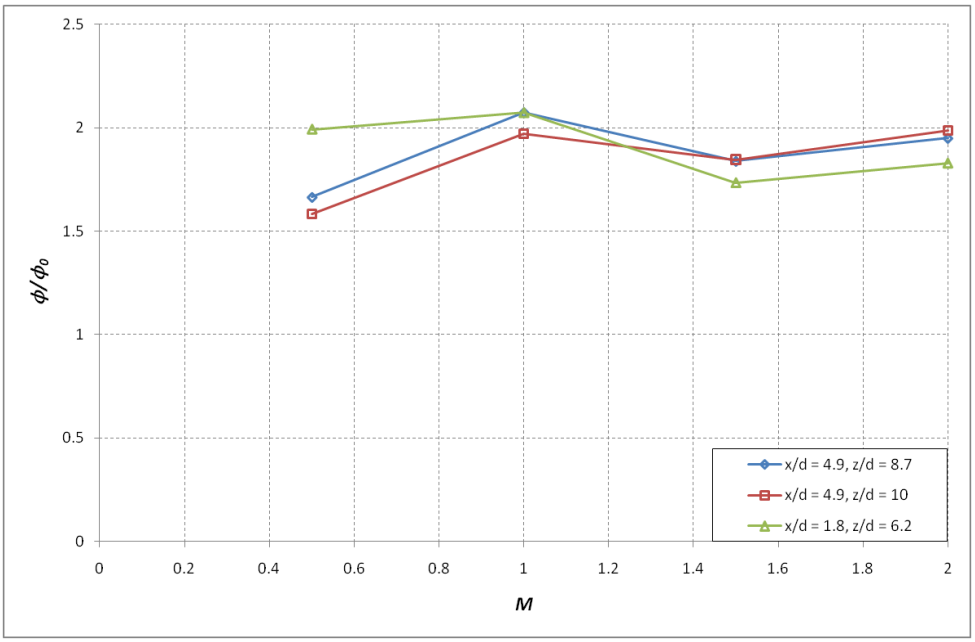

Figure 3.6.8: The ratio of non-dimensional surface temperature with and without film cooling for the positions of the three heat flux gauges

This analysis shows that comparing conjugate studies to more conventional measurements of η and h_f/h_0 remains problematic. It has already been pointed shown by Mouzon *et al.* that comparison to ϕ directly was also a poor means of comparison.

4 Conclusions

This study primarily examined the effect of increasing pitch on a simulated turbine blade leading edge. To better understand the coolant distribution, the adiabatic effectiveness for *p/d* = 7.6 was examined in detail. Then, the effects of pitch variation were explored on matched Biot number models for *p/d* = 7.6, 8.6, 9.6 and 11.6. An important contribution was the presentation of not only the laterally averaged overall effectiveness values, but also the minimum overall effectiveness, which is potentially more important from a design perspective.

Both methods of looking at the data showed that increasing the pitch from *p/d* = 7.6 to 8.6 produced no measurable change in overall effectiveness. Further increasing the pitch to 9.6 caused a small drop in $\bar{\phi}$ of about 4-6% over the *x/d* range investigated. However, when ϕ_{min} was examined, it displayed noticeably more variation, with certain areas of the model displaying up to a 10% decrease, highlighting the importance of this parameter. The last pitch considered, *p/d* = 11.6, showed an overall decrease relative to *p/d* = 7.6 of about 15% when considering $\bar{\phi}$. Again, when ϕ_{min} was examined considerably more variation was visible, with as much as a 27% reduction in some areas.

Internal effectiveness was also evaluated for *p/d* = 7.6, 8.6 and 9.6, which showed approximately a 10% drop for *p/d* = 9.6 relative to 7.6. Additionally, for *p/d* = 7.6, the internal effectiveness with and without impingement cooling was examined. The lack of impingement cooling reduced the internal effectiveness

about as much as increasing the pitch from *p/d* = 7.6 to 9.6, though surface angles greater than 45° displayed more than a 20% reduction.

Lastly, heat flux for both the internal and external surface of the *p/d* = 7.6 model were examined. The internal heat flux was converted to appropriate Nusselt numbers and compared to the literature. For the external data, only the ratio h/h_0 was measureable. This parameter did allow a comparison of measured heat flux ratio to the NHFR parameter, providing some evidence that NHFR is an inappropriate measure of film cooling performance.

4.1 Adiabatic Effectiveness for *p/d* = 7.6

The adiabatic effectiveness tests provided more insight into the behavior of the coolant streams on the surface. The most important result was that at some optimal blowing ratio, near *M* = 2, $\bar{\eta}$ could no longer be improved by increasing the blowing ratio. Higher values only served to decrease the adiabatic effectiveness downstream of the off-stagnation row of holes. Coolant emerging from both stagnation and off-stagnation rows was observed to be separating, with higher blowing ratios producing more separation. More than about 3 hole diameters downstream from the off-stagnation row, the blowing ratio did not noticeably affect the laterally averaged adiabatic effectiveness. Angle of attack testing showed that at high angle (α = ±7.7°), the stagnation line overlaped the off-stagnation row on the negative side, spreading the coolant and producing higher $\bar{\eta}$ values than lower angles, though still less than that seen for α = 0°.

Additionally, the jets for the other two rows of holes were observed to attach better with increasing angle.

When compared to data previously collected using a quarter cylinder model, these experiments agreed well with the data of Yuki [30], but not with that of Johnston [29], even though both were measuring nominally the same geometry. Differences in testing methodology are likely to blame.

4.2 Effects of Pitch Variation on Film Cooling Performance

One of the major goals of this study was to study the effects of pitch variation using matched *Bi* models and the new ϕ_{min} parameter. This was done by producing simulated blade leading edges with an increasing *p/d* of 8.6, 9.6 and 11.6, and comparing to the baseline data taken with *p/d* = 7.6. Each model was tested under blowing ratios of *M* = 1, 1.5, 2, 2.5 and 3 and angle of attacks of α = ±0.6°, ±1.5°, ±4.6° and ±7.7°.

The results showed that the change with increasing pitch was smaller than might have been expected given the increase in surface area that each hole was required to cool. The increase from *p/d* = 7.6 to 8.6, a 13% change in pitch, showed no measureable difference for any tested blowing ratio. For *p/d* = 9.6, the drop in $\bar{\phi}$ compared to *p/d* = 7.6 was only outside the margin of uncertainty for *M* ≥ 2, producing a scant 4% increase in surface temperature for an increase in area of 26%. For all blowing ratios, *p/d* = 11.6 clearly performed worse than *p/d* = 7.6. However, this increase in pitch of 53% only caused about a 15% drop in $\bar{\phi}$.

Analysis of minimum overall effectiveness, ϕ_{min}, showed some similarity with the $\bar{\phi}$ results, but more clearly highlighted potentially life limiting temperatures at some locations. For *p/d* = 8.6 the change was still negligible for all blowing ratios. However, the difference between *p/d* = 7.6 and 9.6 was more pronounced when compared to the $\bar{\phi}$ results. While the majority of *x/d* locations still displayed approximately a 4% decrease in ϕ_{min}, the reduction in minimum overall effectiveness was about 10% in the range 0 < *x/d* < 4. For *p/d* = 11.6, the change was even more noticeable, with $\Delta\phi_{min}$ around 25% over the same *x/d* range. Outside this area immediately around the film cooling holes, both *p/d* = 9.6 and 11.6 showed approximately the same level of performance drop as was observed using $\bar{\phi}$.

The angle of attack data also showed relatively little change in performance between *p/d* = 7.6 and 9.6. Though the increased pitches all appeared to be somewhat less sensitive to changes in α, almost all results were within experimental uncertainty of *p/d* = 7.6. However, there may have actually been a small improvement in performance when increasing *p/d* to 8.6. The change was only marginally outside uncertainty when considering $\bar{\phi}$, but examination of ϕ_{min} showed that there likely was a 15% improvement over the majority of the *x/d* range. This change was possibly caused by a change in how the mainstream was interacting with the surface, producing reduced *h* and therefore colder surface temperatures. Further increasing *p/d* to 9.6 brought the overall effectiveness back within experimental uncertainty of *p/d* = 7.6. For all

tested angles of attack the *p/d* = 11.6 data were significantly warmer than *p/d* = 7.6, at levels similar to that seen with the blowing ratio variation (15% lower), though this pitch also displayed insensitivity to α on the positive side.

A simplified analysis was performed which helped to clarify why the changes in surface temperature were so small compared to the increase in pitch. Using a one dimensional conduction approximation, an equation relating ϕ to η and *Bi* for a cylindrical surface was presented.

Using a few more assumptions, this equation made the general prediction that, for this geometry, $\bar{\phi}$ will change half as much as $\bar{\eta}$ on a percentage basis. Additionally, the decreases in ϕ would occur in small areas between holes, producing a weak effect on $\bar{\phi}$. Even changes in minimum adiabatic effectiveness would be mitigated by conduction from less affected areas and the fact that internal heat transfer coefficients were expected to remain essentially the same with increasing pitch.

Another method of comparing the pitch variation data was plotting the spatially averaged overall effectiveness against the total coolant flow rate using the parameter *M/(p/d)*. While it was not clear if this parameter provided a better scaling for the data than *M*, it was shown that the data collapsed along a single line for *p/d* = 7.6, 8.6 and 9.6. The implication was that an increase in pitch may be compensated for by a corresponding increase in *M*, which occurs naturally if the total coolant flow rate is held constant. This would allow fewer holes to be drilled, reducing the cost of a part. However, the overall effectiveness data for *p/d*

= 11.6 clearly showed that there is some limit where this scaling no longer applies, since it did not collapse along the same line. In order to match a given $\bar{\bar{\phi}}$ from a closer pitch, the total coolant flow rate for *p/d* = 11.6 would have to be increased about 30% relative to *p/d* = 7.6.

The internal effectiveness data showed that over the majority of the inner surface, there was a measureable increase in temperature between *p/d* = 7.6 and *p/d* = 8.6. However, further increasing *p/d* to 9.6 did not show any additional change. The measurement of the no impingement case showed that while there was a substantial increase in h_i, there was barely any change in ϕ_i when compared to the case with impingement jets. The most likely explanation is that the temperature difference between the cooling gas and the surface was so small near the cooling holes that even a factor of three increase in h_i did not remarkably change the heat flux. For surface angles greater than 45° – farther from film-cooling holes and the impinging jets – impingement cooling did have a very clear effect, producing a 20% increase in ϕ_i.

4.3 Internal and External Heat Flux Measurements

Unfortunately, the heat flux gauges used in this study were damaged during the course of learning to use them properly, producing some unreliable data. After considerable analysis, some of the data were still considered to be useful, but very little of the originally desired data was obtained. However, what data were extracted still provide some important conclusions.

On the interior surface, no other impingement study has attempted to measure impingement jets confined completely by a highly curved cavity and exhausted only through holes in the target surface. Therefore, these data possibly represent a more accurate representation of blade leading edge internal cooling than is currently available in the literature.

The data of Bunker and Metzger [32] was similar to this study's with the exception of jet confinement and coolant exhaust path. At the jet stagnation point, their data were within experimental uncertainty of this study. However, the same data compared at x/d_j = 2 did not agree with their data, which showed nearly double the Nusselt number. Geometric differences between models are much more likely to affect heat transfer away from the impinging jet, so even this large difference was not that surprising.

The computational predictions of Ravelli *et al.* [21] matched this study's geometry exactly. One of the contributions of this study was to provide some data to validate their predictions. They over-predicted the Nusselt number by about 40% at the stagnation point. At the x/d_j = 2 position, predicted Nusselt number was high but close to the experimental uncertainty of 17%.

A simple correlation was developed for the stagnation point that matched well with the data. A separate correlation provided a good fit for the x/d_j = 2 position.

On the exterior, only data making use of the ratio h/h_0 could be used. No direct heat flux measurements were considered useful. The h/h_0 measurements

confirmed that h would be reduced by film cooling. Because h_f is typically measured in the literature, not h, there was no other data suitable for comparison.

Using ϕ_0 data from Dobrowolski [23], the h/h_0 data was converted to a heat flux ratio similar to NHFR. It was shown that while NHFR would always predict that heat flux was reduced by film cooling, in fact the opposite was true. Further, it was shown that NHFR may not even accurately predict trends in surface temperature, since at a location where NHFR was increasing with M – which should indicate that the performance of film cooling relative to a surface without film cooling should be improving – the measured value ϕ/ϕ_0 was actually decreasing, indicating that locally increasing blowing ratio was not helping.

This evidence that NHFR is not a useful parameter may be the most significant finding of this study. However, the high uncertainty and extreme sparsity in the measurements mean that more data would be required before a strong recommendation could be made to completely abandon NHFR as a predictive tool.

4.4 Recommendations for Future Work

The most tantalizing results from this study were the limited data obtained with the heat flux gauges. On the interior, more, better data would be extremely useful in determining why Nusselt number did not match up with other experimental data away from the stagnation point, showing where extant

impingement studies may be lacking in performance prediction. Additionally, directly measuring heat flux through the internal wall under different impingement scenarios would help better quantify the increase in through-hole convection that may be compensating for increases in heat loading due to an increased pitch. Additionally, this data would provide more validation of computational predictions using this geometry.

On the exterior, a better map of flux into the surface would be useful in a number of ways. First, the validity of using NHFR as a predictive measure could be assessed over the whole surface. There was some indication that NHFR may an inappropriate measure, but the data are admittedly very limited. To support the idea that NHFR should be abandoned, more, higher quality data would be required. Additionally, some computational studies (Dobrowolski [23] contains a list) have recently questioned the validity of using the T_{aw} assumption near the coolant holes and under the coolant jets. This assumption could be evaluated experimentally using heat flux measurements.

Evaluating more pitches would help identify the point at which performance begins to drop more significantly. Additionally, a correlation might be created to predict the change in temperature for a given change in pitch. While several explanations were proposed for the unexpected lack of sensitivity of the longer pitches to angle of attack, revisiting this data could provide further insight. If nothing else, repetition of the data may allow firmer conclusions about the relative performance between p/d = 7.6 and 8.6 to be drawn.

A. Appendix

This appendix contains additional explanation of some finer points, the details of which are not completely germane to the primary discussion. Additionally, some data which were used to verify the overall effectiveness results did not have a bias due to convective heating of the coolant as it passed through the impingement plate.

A.1 Explanation for Constant Internal and External Heat Transfer Coefficients

The reason that h_f remains relatively unchanged with a (small) increase in pitch is conceptually simple. Consider the point *x/d* = 6.3 for *p/d* = 7.6. For this location, Dobrowolski [23] computed that $\overline{h}_f/\overline{h}_0$ = 1.19. A reasonable assumption for the behavior of the heat transfer augmentation is that it will be confined to the region around the jet. An increase in pitch then would serve only to increase the length of the region away from the jet where the heat transfer coefficient is unaffected *i.e.* $\overline{h}_f/\overline{h}_0$ = 1. The new value of $\overline{h}_f/\overline{h}_0$ is simply determined from an average including the new length. Even for the full increase in pitch of 53%, $\overline{h}_f/\overline{h}_0$ is only reduced to 1.12, a slightly less than 6% reduction.

For the internal surface, the assumption might be that more widely spaced impingement jets would dramatically change the internal flow and therefore h_i. However, Bunker and Metzger [32] showed using a target with similar relative

curvature (d_j/D_i = 0.48) and jet-to-target spacing (5.1d_j) that an increase in impingement jet pitch of 40% resulted in values of $\overline{h}_i$ that were only very slightly different near the stagnation line (~10%) and within experimental uncertainty for values of x/d_j higher than 1. Although they did not use an impingement jet pitch quite as long as that used in this study (3.33 and 4.67 vs. 4.8 to 6), their results indicate that away from the jet (approximately x/d_j > 2) lateral h_i variations were negligible, indicating that the heat transfer might be driven by a larger vortical structure that forms along the entire length of the span.

A.2 Verification that the Aluminum Impingement Plate was Not Adversely Affecting Effectiveness Measurements

There was some concern that the convective cooling of a metal impingement plate, which was in direct contact with a support bracket heated by mainstream air, could be affecting results. This heating across the impingement plate could artificially reduce measured overall and internal effectiveness levels. A comparison of the metal and plastic impingement data is presented in Figure A.2.1, along with the data where no impingement plate was present at all. The change from metal to plastic impingement plate had no measurable effect on overall effectiveness. More surprising was the fact that completely removing the impingement plate also had no visible effect until about x/d = 8. Even this far away from the cooling holes the difference was only 0.03, which is still nominally within experimental uncertainty.

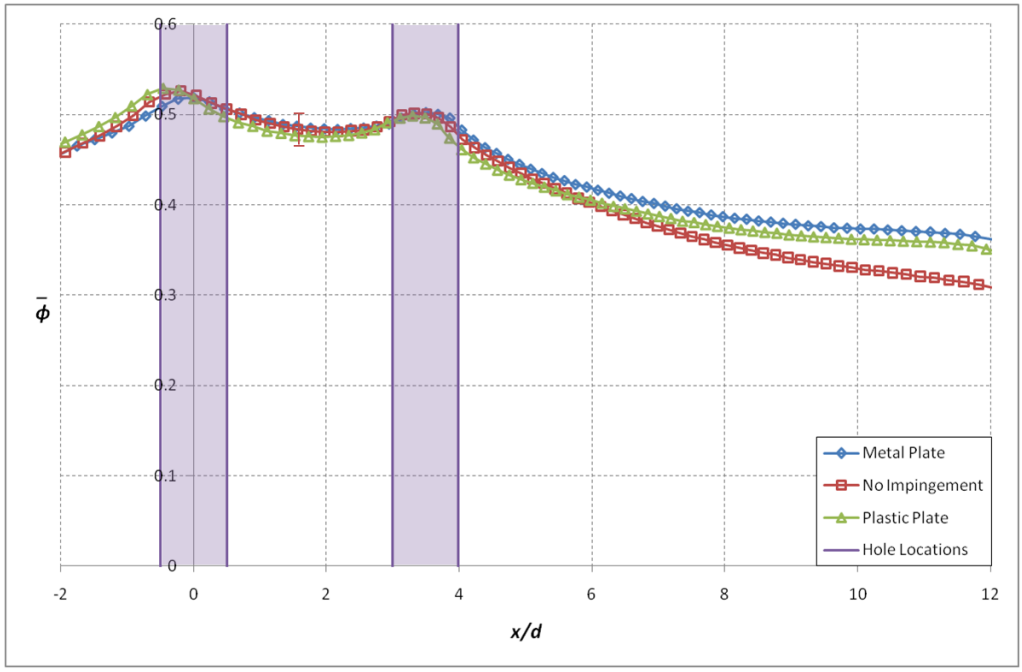

Figure A.2.1: Comparison different impingement conditions using $\bar{\phi}$ for *M* = 2 and *p/d* = 7.6

. Figure A.2.2 compares the internal effectiveness for the two plates at *p/d* = 7.6 and *M* = 2. At all measured points, the values fall very close to each other with the exception of the 45° point. This point is still within experimental uncertainty. All tested blowing ratios show similar levels of agreement between the metal and plastic impingement plate cases.

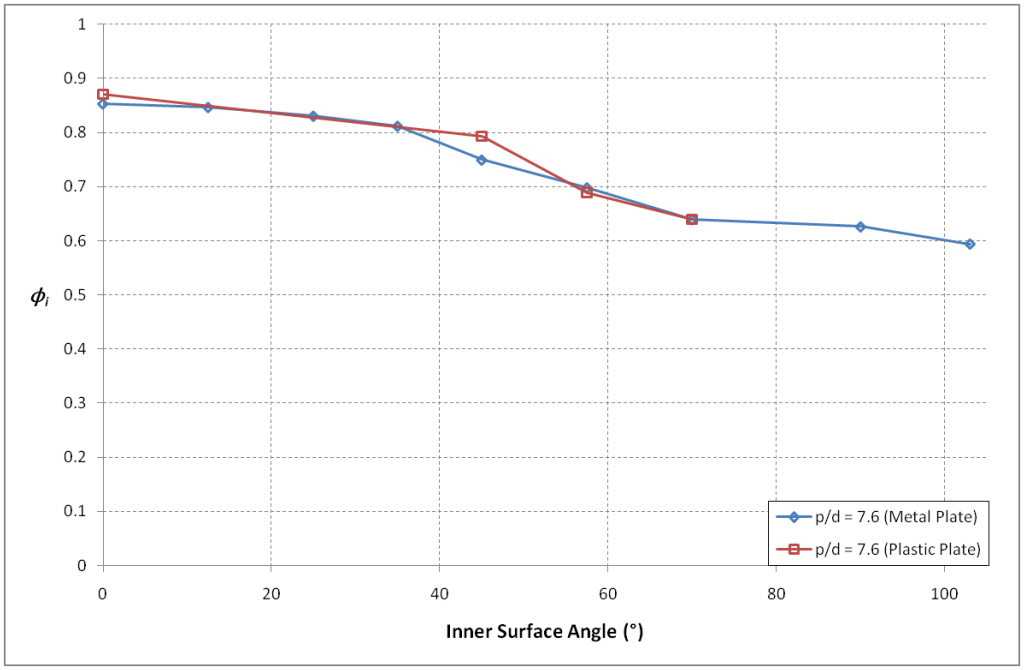

Figure A.2.2: Comparison of ϕ_i for *M* = 2 and *p/d* = 7.6 for aluminum and acrylic impingement plates

The sensitivity of internal temperature to the temperature of the gas is unknown. A recognized oversight of this test was that the gas temperature for the two cases was not measured directly. However, given that neither the internal nor external temperatures were notably affected by changing impingement plats, there is strong reason to believe that any heating of the coolant or conduction losses by the model into the impingement plate was very small.

References

[1] George B. Brayton, "Improvement in Gas-Engines," 125166, April 2, 1872.

[2] Duk. (2006, March) Wikipedia.org. [Online]. http://en.wikipedia.org/wiki/File:Brayton_cycle.svg

[3] Michael J. Moran and Howard N. Shapiro, *Fundamentals of Engineering Thermodynamics, 4th ed.* New York: John Wiley & Sons, Inc., 1999, pp. 441-477.

[4] Fred O. Soechting, "A Design Perspective on Thermal Barrier Coatings," *Journal of Thermal Spray Technology*, vol. 8, pp. 505-511, 1999.

[5] Derek D. Haas, "Directed Vapor Deposition of Thermal Barrier Coatings," Charlottesville, Ph. D. Dissertation 2000.

[6] Elon J. Terrell, "A Study of the Convective Heat Transfer through Film Cooling Holes of a Gas Turbine Leading Edge," Austin, M. S. Thesis 2004.

[7] Marcia I. Ethridge, J. Michael Cutbirth, and David G. Bogard, "Scaling of Performance for Varying Density Ratio Coolants on an Airfoil with Strong Curvature and Pressure Gradient Effects," in *Proceedings of ASME Turbo Expo 2000*, Munich, Germany, 2000.

[8] S. V. Ekkad, J. C. Han, and H. Du, "Detailed Film Cooling Measurements on a Cylindrical Leading Edge Model: Effect of Free-Stream Turbulence and Coolant Density," *Journal of Turbomachinery*, vol. 120, pp. 799-807, October 1998.

[9] C. A. Johnston, David G. Bogard, and M. A. McWaters, "Highly Turbulent Mainstream Effects on Film Cooling of a Simulated Turbine Airfoil Leading Edge," in *ASME Turbo Expo 1999*, Inianapolis, 1999.

[10] Yoran Pichon, "Turbulence Field Measurments for the Small Wind Tunnel," The University of Texas at Austin, Austin, TTCRL Internal Report 2009.

[11] U. M. Yuki, David G. Bogard, and J. M. Cutbirth, "Effect of Coolant Injection on Heat Transfer for a Simulated Turbine Airfoil Leading Edge," in *ASME Turbo Expo 1998*, Stockholm, 1998.

[12] W. J. Mick and R. E. Mayle, "Stagnation Film Cooling and Heat Transfer, Including Its Effect Within the Hole Pattern," *Journal of Turbomachinery*, vol. 110, pp. 66-72, 1988.

[13] B. Sen, D. L. Schmidt, and D. G. Bogard, "Film Cooling with Compound Angle Holes: Heat Transfer," *Journal of Turbomachinery*, vol. 118, no. 4, pp. 800-807, October 1996.

[14] Jason E. Albert, "Adiabatic and Overall Film Cooling Effectiveness Measurement of a Forward-Diffused Film Cooling Configuration for a Turbine Blade Leading Edge," Austin, M. S. Thesis 2003.

[15] Ross G. Johnson, "Experimental Study of the Effect of Oscillating Stagnation Line on Overall Cooling Performanec on a Leading Edge with One Row of Cooling Holes," The University of Texas at Austin, Austin, M. S. Thesis 2008.

[16] Brian D. Mouzon, Elon J. Terrell, Jason E. Albert, and David G. Bogard, "Net Heat Flux Reduction and Overall Effectiveness for a Turbine Blade Leading Edge," in *ASME Turbo Expo 2005: Power for Land, Sea and Air*, Reno, 2005.

[17] Elon J. Terrell, Brian D. Mouzon, and David G. Bogard, "Convective Heat Transfer through Film Cooling Holes of a Gas Turbine Leading Edge," in *ASME Turbo Expo 2005: Power for Land, Sea and Air*, Reno, 2005.

[18] Jonathan Maikell, David Bogard, Justin Piggush, and Atul Kohli, "Experimental Simulation of a Film Cooled Turbine Blade Leading Edge Including Thermal Barrier Coating Effects," in *Proceedings of ASME Turbo Expo 2009: Pawer for Land, Sea and Air*, Orlando, 2009.

[19] D. L. Schmidt, B. Sen, and D. G. Bogard, "Film Cooling with Compound Angle Holes: Adiabatic Effectiveness," *Journal of Turbomachinery*, vol. 118, pp. 807-813, October 1996.

[20] K. Jambunathan, E. Lai, M. A. Moss, and B. L. Button, "A Review of Heat Transfer Data for Single Circular Jet Impingement," *International Journal of Heat and Fluid Flow*, vol. 13, no. 2, pp. 106-115, June 1992.

[21] Silvia Ravelli, Laurene Dobrowolski, and David G. Bogard, "Evaluating the Effects of Internal Impingement Cooling on a Film Cooled Turbine Blade Leading Edge," in *Proceedings from the ASME Turbo Expo 2010: Power for Land, Sea and Air*, Glasgow, UK, 2010.

[22] Jonathan S. Maikell, "Experimental Study of the Effect of TBC and Angle of Attack on Overall Cooling Performance on a Leading Edge with One and Three Rows of Cooling Holes," The University of Texas at Austin, Austin, M. S. Thesis 2008.

[23] Laurène Dobrowolski, "Numerical Simulation of a Film Cooled Turbine Blade Leading Edge Including Heat Transfer Effects," The University of Texas at Austin, Austin, M. S. Thesis 2009.

[24] Brian D. Mouzon, "Net Heat Flux Reduction and Overall Effectiveness for a Turbine Blade Leading Edge," The University of Texas at Austin, Austin, M. S. Thesis 2005.

[25] Scot K. Waye, "Film Cooling Effectiveness of Suction Side Axial Holes, Compound Angle Holes, and Axial Holes Embedded within an Overlying Transverse Trench," The University of Texas at Austin, Austin, M. S. Thesis 2005.

[26] R. J. Moffat, "Using Uncertainty Analysis in the Planning of an Experiment," *Journal of Fluids Engineering*, no. 107, pp. 173-178, June 1985.

[27] Atul Kohli, Personal Communication, March 2010.

[28] Je-Chin Han, Sandip Dutta, and Srinath V. Ekkad, "Impginement Heat Transfer in the Laeding Edge," in *Gas Turbine Heat Transfer and Cooling Technology*. New York, USA: Taylor & Francis, 2000, ch. 4.1.4.2, pp. 279-285.

[28] Christopher A. Johnston, "High Mainstream Turbulence Effects on Film Cooling of a Turbine Blade Leading Edge," The University of Texas at Austin, Austin, M. S. Thesis 1999.

[29] U. M. Yuki, "Heat Transfer and Adiabatic Effectiveness Measurements on a Simulated Film-Cooled Turbine Blade Leading Edge," The University of Texas at Austin, Austin, M. S. Thesis 1998.

[30] Ross Johnson, Jonathan Maikell, and David Bogard, "Experimental Study of the Effects of an Oscillating Approach flow on Overall Cooling Performance of a Simulated turbine Blade Leading Edge," in *ASME Turbo Expo: Power for Land, Sea and Air*, Orlando, 2009.

[31] R. S. Bunker and D. E. Metzger, ""Local Heat Transfer in Internally Cooled Turbine Airfoil Leading Edge Regions: Part I - Impingement Cooling Without Film Coolant Extraction," *Journal of Turbomachinery*, vol. 112, pp. 451-458, July 1990.

[32] M. E. Taslim, L. Setayeshgar, and S. D. Spring, "An Experimental Evaluation of Advanced Leading Edge Impingement Cooling Concepts," *Journal of Turbomachinery*, vol. 123, no. 1, pp. 147-153, January 2001.

Vita

Thomas Dyson was born in Webster, Texas. He lived there until he graduated from Clear Lake High School in 2001. Thomas then attended Texas A&M University's College Station campus. In December 2005, he received a B.S.M.E. from that institution.

While attending college, Thomas worked summers for Tietronix Software, Inc., a NASA contractor in Houston, Texas. Upon graduation, he accepted a position as a programmer/designer with Tietronix. He worked there until late 2007, when he moved to Austin to attend graduate school at the University of Texas at Austin starting in January of 2008.

Thomas worked in the Turbulence and Turbine Cooling Research Laboratory facility, and completed the requirements for a Master's of Science in Mechanical Engineering in May of 2010. He plans to continue under Dr. Bogard in the pursuit of a Ph. D.

He was a UTSR Fellow in 2009, working with Pratt & Whitney as part of the program.

Permanent Address: 7601 Helecho CT, Austin, TX 78745.

This thesis was typed by the author.